Controllable assembly of graphene hybrid materials and their application in energy storage and conversion

Dissertation

zur Erlangung des Grades
„Doktor der Naturwissenschaften“

im Fachbereich Chemie, Pharmazie, und
Geowissenschaften der Johannes Gutenberg-Universität
Mainz und in Kooperation mit dem Max-Planck-Institut
für Polymerforschung Mainz

vorgelegt von

Wei Wei

geboren in Shanxi / China

Mainz, 2015

Dekan:

1. Berichterstatter:

2. Berichterstatter:

Tag der mündlichen Prüfung:

Table of Contents

Chapter 1 Introduction

The development of high-performance, environmentally friendly, and low-cost energy storage and conversion systems (ESCSs) has been under an ever increasing demand in response to the challenges of electronic market enlargement and ecological concerns. Lithium-ion batteries (LiBs), supercapacitors (SCs) and fuel cells (FCs) are termed representative ESCSs as they rely on common electrochemistry principle.[1, 2] LiBs and SCs are electrochemical energy storage devices, while FCs are electrochemical energy conversion devices. Despite the remarkable progress achieved for ESCSs, several key points remain to be addressed, such as the low efficiency, poor durability, high cost and operation problems.[3-5] The performance of ESCSs depends intimately on the properties of electrode materials. For example, nanostructured materials have so far exhibited multiple advantages such as increased electrode/electrolyte interface contact and high electrochemical activity in comparison to conventional bulk materials.[6] In this respect, the development of low cost and highly efficient ESCSs can only be achieved by major advances in new material synthesis.

Design and construction of hybrid materials (HMs) offer opportunity to combine or create properties superior to those of individual components for ESCSs. Carbon materials, such as graphite, activated carbon and carbon black, are the most popular building blocks to construct HMs for ESCSs, because of their high electrical conductivity, excellent chemical stability and low cost.[7] The beneficial role of carbon is manifold, either to increase the utilization of electrochemically active constituents or improve the mechanical

strength/electrical conductivity of HMs. Recently, with the rapid development of nanoscience and technology, nanostructured carbon materials, such as template-synthesized carbons,[8] carbon nanofibers,[9] and nanotubes (CNTs),[10] have been explored to prepare HMs with diversified morphology and intriguing properties. The remarkable physical properties of these nanocarbons can be transferred to the frameworks of HMs, leading to significant performance enhancement. However, the high production cost and poor mass-producibility of these nanocarbons prevent their widespread use for practical applications.

Graphene, a free-standing atomic thick layer of sp^2 carbon atoms, has emerged as the new generation of carbon materials in the last decade not only due to its unprecedented physical and chemical properties such as high mechanical strength, good electrical/thermal conductivity and chemical stability but also due to its unique two-dimensional (2D) morphology and high specific surface area.[11, 12] Graphene can serve as appealing substrates for the binding of various functional components, which provide an opportunity for the construction of HMs with different complexity.[13-15] Although research is still at its early stages, graphene-based hybrid materials (GHMs) already exhibit several potential advantages over conventional carbon hybrids, and solve many vital issues in ESCSs.[16, 17] Very recently, large-scale synthesis of high-quality graphene was achieved by electrochemical exfoliation of graphite in aqueous solutions.[18] The mass producibility combined with superior properties renews graphene a promising candidate in the development of novel HMs.

1.1 Graphene

1.1.1 Structure and morphology

Graphene refers to a single honeycomb lattice of graphite, composed of equivalent sub-lattices of carbon atoms bonded with σ bonds in an angle of 120^{o} and partially filled π-orbitals above and below the graphitic plane.[19-21] Andre K. Geim and Konstantin S. Novoselov, both at the University of Manchester, made the decisive contribution to the development of graphene. They succeeded in isolating, identifying and characterizing graphene and won the Nobel Prize in Physics in 2010.[22, 23]

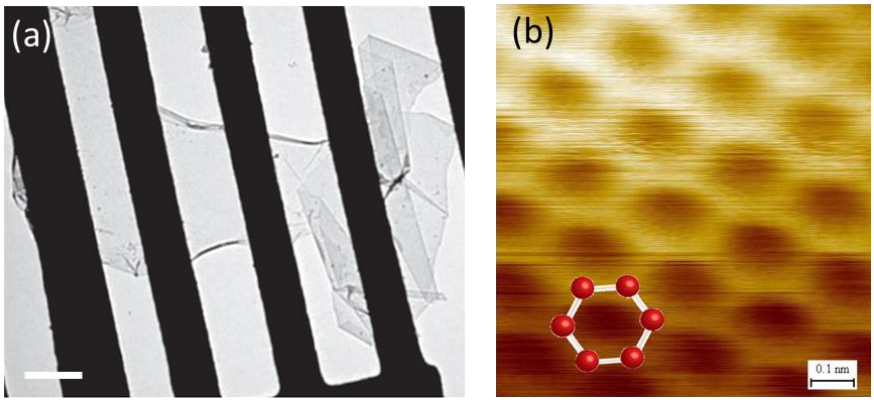

Figure 1.1 (a) Bright-field TEM image of a suspended graphene sheet.[24] The monolayer graphene displays homogeneous and featureless region in the central part and scrolled edges and strongly folded regions on the right. Scale bar: 500 nm; (b) STM topographic image of a monolayer graphene displays a symmetric honeycomb structure in which all of the surface atoms contribute equally to the tunneling image.[25]

The bright-field transmission electron microscopy (TEM) image discloses that the central parts of suspended graphene are homogeneous and featureless, whereas the sheet edges tend to scroll owing to the flexible and ultrathin features of graphene (Figure

1.1a).[24] The surface area of monolayer graphene sheet is calculated to be 2630 m^2 g^{-1},[26] substantially higher than the values of various activated carbon.[27] The thickness of monolayer graphene can be determined by atomic force microscopy (AFM) and cross-sectional TEM measurement. AFM images for monolayer graphene indicate that the average thickness ranges from ~0.3 to ~1.0 nm depending on the measurement parameters/conditions such as the atmospheric pressure and the substrates used.[28] Scanning tunneling microscopy (STM) measurements demonstrate that a monolayer graphene sheet displays asymmetric honeycomb structure in which all of the surface atoms contribute equally to the tunneling images. (Figure 1.1b).[25]

1.1.2 Electronic properties

Graphene displays intriguing electronic phenomena, such as the Dirac nature of the charge carriers.[29, 30] In particular, the electrons in graphene behave as massless relativistic particles (Dirac fermions) at a Fermi velocity (v_F) of ~1×10^6 m s^{-1}, and the travel distances are in the order of micrometers without scattering.[31, 32] Such a phenomenon is referred to as ballistic transport.[33, 34] Further, graphene has a remarkably high electron mobility which is nearly independent of temperature between 10 K and 100 K.[32] A mobility in excess of 200,000 cm^2 V^{-1} s^{-1} at a carrier density of ~2×10^{11} cm^{-2} has been measured for a mechanically exfoliated suspended layer of graphene on a Si/SiO_2 gate electrode.[35]

It should be mentioned that the presence of disorder (e.g. atomic vacancies and topological defects), absorbed impurities and the substrates used can affect the electronic properties of graphene.[36-38] These factors in general act as scattering sites and inhibit charge transport by limiting the electron mean free path.[39, 40] For example, the

conductivity and mobility of reduced graphene oxide (RGO, 0.05–2 S cm^{-1} and 2–200 cm^2 Vs^{-1} respectively) were reported to be 3 and 2 orders of magnitude smaller than these of pristine graphene.[41] The degradation on conductivity is due to the lattice vacancies of RGO which cannot be healed during reduction process.[42]

1.1.3 Mechanical and thermal stability

The mechanical properties of graphene including the Young's modulus and fracture strength have been widely investigated. The elastic properties and intrinsic breaking strength of free-standing monolayer graphene were measured by nanoindentation using an AFM (Figure 1.2a-b).[43] The breaking strength of a defect-free graphene sheet is calculated to be 42 N m^{-1}, which corresponds to a Young's modulus of E=1.0 TPa and third-order elastic stiffness of D=−2.0 TPa. These measurements establish graphene as the strongest material ever discovered.

The thermal stability of graphene produced by either mechanical cleavage or reduction of graphene oxide was studied by Raman spectroscopy and thermogravimetric analysis (TGA) respectively. It was found that mechanical cleaved graphene starts to show defects at ~500°C, indicated by the appearance of a disorder-induced Raman D peak (Figure 1.2c).[44] The defects are initially sp^3 type and convert to a vacancy at higher temperature. In a sharp contrast, GO is thermally unstable and starts to lose mass upon heating even below 100°C. The TGA analysis (Figure 1.2d) indicates a major mass loss occurring at 200°C, presumably due to elimination of the oxygen-containing functional groups, yielding CO, CO_2, and steam.[45] After chemical reduction of GO with hydrazine, the thermal stability of

reduced GO is increased significantly. Apart from a slight mass loss of adsorbed water below 100°C, no significant mass loss is detected when RGO is heated up to 800°C.

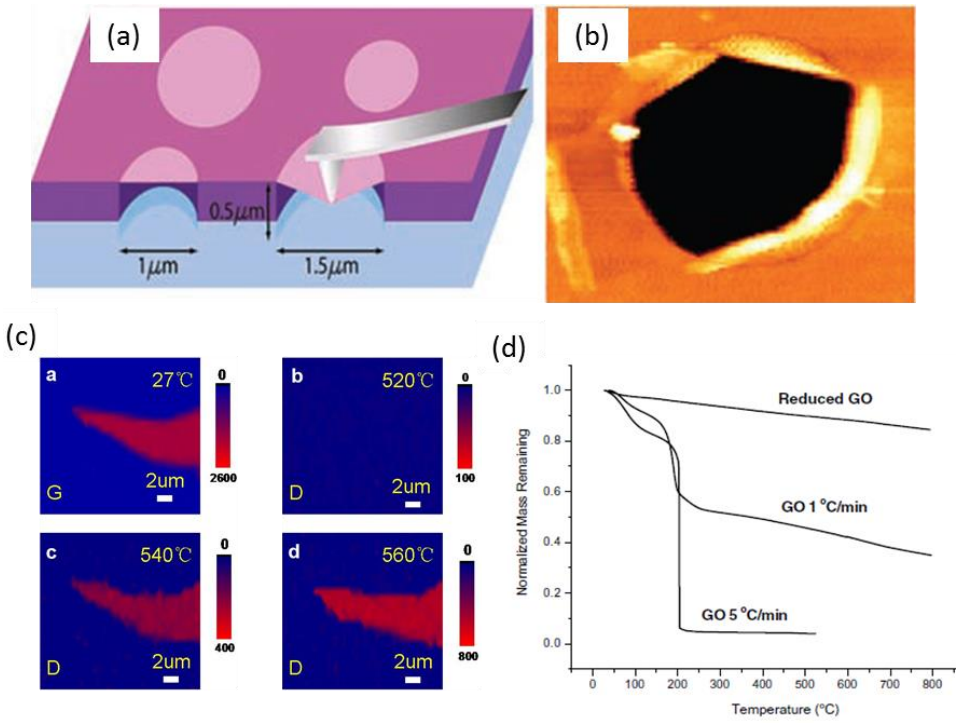

Figure 1.2 (a) Schematic of nanoindentation on suspended graphene membrane;[43] (b) AFM image of a fractured membrane;[43] (c) Raman images of the intensities of G and D peaks of single layer graphene (by mechanical cleavage) after thermal treatment in air at different temperatures;[44] (d) Normalized TGA plots for GO and the reduced GO.[45]

1.2 Synthesis of graphene

Approaches for the preparation of graphene mainly include micromechanical cleavage,[20-22] chemical vapor deposition (CVD),[46-48] liquid-phase exfoliation,[49, 50] electrochemical exfoliation,[51, 52] chemical oxidation/reduction of graphite,[53, 54] and bottom-up organic synthesis,[55, 56] etc. Some methods have been designed to obtain high-

quality, large-area and structurally defined graphene, though there are still some disadvantages for each method. For instance, micromechanical cleavage and liquid-phase exfoliation exhibit the capability to obtain high-quality graphene, but they are not suitable for industrial-scale utilization in terms of throughput and cost.

In the following sections, the chemical oxidation/reduction and electrochemical exfoliation approaches targeted for large-scale preparation of GHMs will be summarized.

1.2.1 Chemical oxidation/reduction of graphite

To date, the chemical oxidation and reduction is the most appealing method to prepare graphene owing to the potential scalability and solution processability. In a typical procedure, graphite oxide is initially synthesized through oxidation of graphite with concentrated sulphuric acid, nitric acid and potassium permanganate based on Hummers' method.[54] This aggressive chemical process impairs the sp^2-bonded networks of graphene flakes, leaving sp^3 carbons and vacancies which disrupt their electronic properties. Based on the Lerf-Klinowski model (Figure 1.3a),[57] the graphite oxide consists of oxidized graphene sheets (graphene oxide, GO) with hydroxyl and epoxy groups on the basal planes and carboxylic and carbonyl groups at the sheet edges. These oxygen containing groups make graphite oxide hydrophilic, and result in a larger interlayer spacing (6-12 Å) than graphite (3.4 Å).[58] Consequently, GO can be readily exfoliated by either sonication in water or thermal expansion of as-obtained graphite oxide.

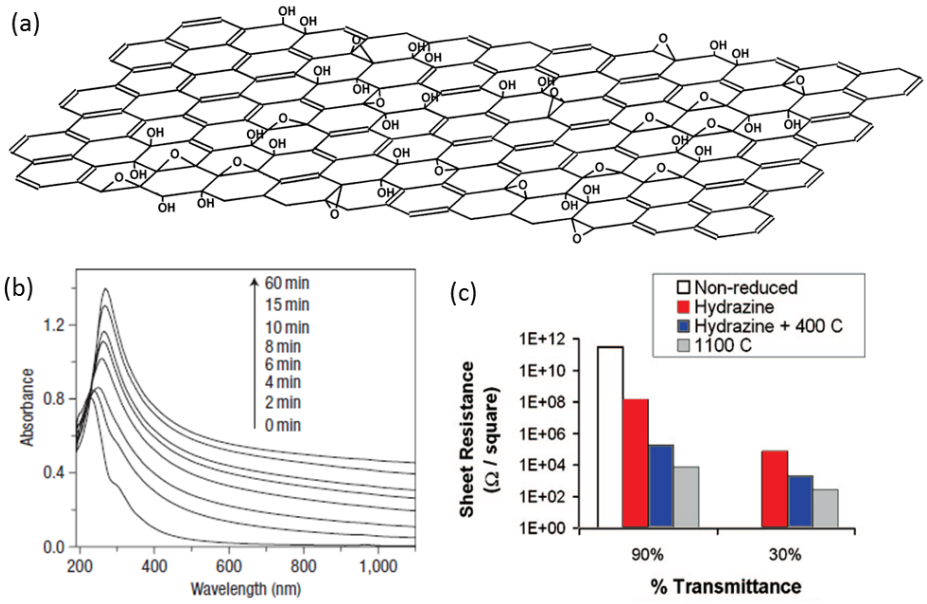

Figure 1.3 (a) A proposed schematic structure of GO based on Lerf-Klinowski model;[57] (b) UV-vis absorption spectra showing the change of GO dispersions as a function of reduction time by hydrazine.[59] The absorption peak of the GO dispersion at 231 nm gradually redshifts to 270 nm, suggesting that the electronic conjugation of GO is restored upon hydrazine reduction; (c) Comparison of sheet resistance of GO films of different optical transparency after undergoing different reduction treatments.[60]

By nature, GO is electrically insulating owing to the loss of electronic conjugation during the oxidation process. Further reduction via either chemical or thermal methods is necessary to decrease the network defects and re-establish an electrical/thermal conductivity of graphene (Figure 1.3 b-c).[59-61] Chemical reduction via hydrazine (N_2H_4) is currently the most popular approach to produce thin and conductive reduced GO sheets (RGO). The electrical conductivities of compressed-powder samples of GO, RGO and pristine graphite were investigated at room temperature with 30% relative humidity.[45] Notably, it was found that the conductivity of RGO (~2×10^2 S m^{-1}) is about 5 orders of magnitude better than that of GO, and approximately 10 times lower than that of pristine

graphite powder (at only about 10% of bulk graphite density). One of the key issues for chemical reduction is that GO sheets become less hydrophilic upon reduction and tend to aggregate and precipitate. GO could be converted to stable colloidal RGO in alkaline dispersions (e.g. ammonia, NaOH) through electrostatic repulsion,[59, 62, 63] which make it possible to obtain graphene using low-cost and facile processing techniques.

1.2.2 Electrochemical exfoliation

Recently, electrochemical exfoliation of graphite has attracted great attention due to its easy, fast, and environmentally friendly nature to produce high-quality graphene.[64-66] Electrochemical exfoliation of graphite has been performed mainly in two different types of electrolytes, including ionic liquids and aqueous solutions. Ionic liquids are proposed as ‘‘green’’ electrolyte for electrochemical exfoliation of graphene, owing to its negligible vapor pressure, low toxicity, relatively wide potential window and high stability.[67, 68] For example, Luo etc. reported a one-step, ionic-liquid-assisted electrochemical approach for the synthesis of graphene nanosheets (GNS).[69] Briefly, 1-octyl-3-methyl-imidazolium hexafluorophosphate ($[C_8mim]^+[PF_6]^-$) and water were used as the electrolyte, and a static potential of 15V was applied between two graphite rods to afford a black precipitate. The ionic-liquid-treated graphite sheets can be dispersed in polar aprotic solvents (such as *N*,*N*-dimethyl formamide (DMF), *N*-methyl-2-pyrrolidone (NMP) and dimethyl sulfoxide (DMSO)), which makes GNS an ideal candidate for synthesis of graphene/polymer hybrids (e.g. GNS/polystyrene).

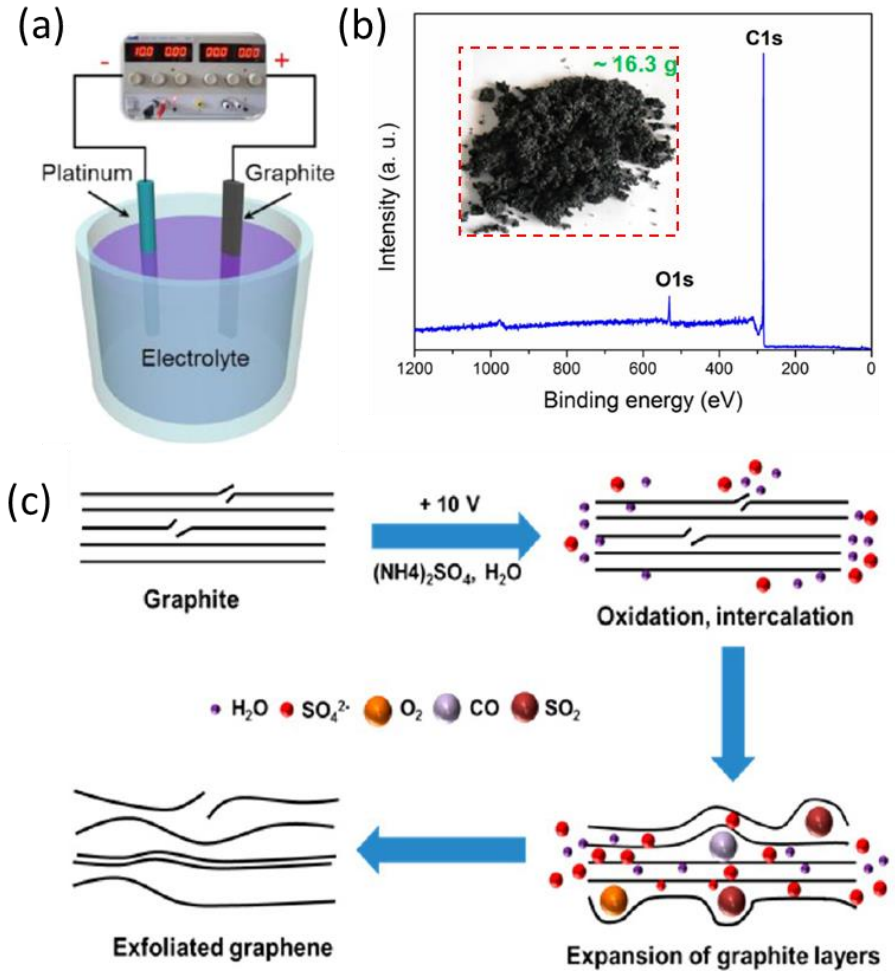

Figure 1.4 (a) Schematic illustration of the electrochemical exfoliation of graphite;[18] (b) XPS spectra of EG obtained from $(NH_4)_2SO_4$ electrolyte (Inset: photograph of EG powders on a bulk scale (~16.3 g));[18] (c) Schematic illustration of electrochemical exfoliation mechanism.[18]

Very recently, our group reported a prompt electrochemical exfoliation of graphene sheets in aqueous inorganic salts, such as $(NH_4)_2SO_4$, Na_2SO_4, and K_2SO_4 (Figure 1.4a).[18] The exfoliated graphene (EG) sheets exhibit an outstanding C/O ratio of 17.2 (oxygen content: 5.5 at.%) and low defect density (Figure 1.4b). Most importantly, the EG sheets can be readily produced on tens of grams scale, demonstrating a great potential for industrial scale-up production (inset of Figure 1.4b). The mechanism of electrochemical

exfoliation is proposed based on the morphology change of graphite foil (Figure 1.4c). Firstly, nucleophilic attack of graphite by OH^- ions occurs at the edge sites and grain boundaries, and leads to depolarization and expansion of the graphite layers. Subsequently, the SO_4^- anions intercalate within graphitic layers and react with H_2O to produce gaseous species such as SO_2, O_2 etc. These gaseous species exert large forces on the graphite layers and separate the bonded graphite layers from one another. The resultant EG sheets are highly solution-processable in organic solvents (e.g. DMF), which permits their direct use for the fabrication of GHMs (e.g. EG paper) and energy storage devices (e.g. all-solid-state flexible SCs).

1.3 Functionalization of graphene

The surface functionalization plays an important role in the assembly of graphene and thus holds the key to build up high-performance GHMs electrode materials. There are basically two types of surface functionalization of graphene: covalent functionalization and noncovalent functionalization. Owing to the existence of abundant oxygen functional groups, graphene derivatives including GO and RGO have been extensively utilized to covalently bond with various organic/polymeric functionalities.[70-72] For example, GO had been treated with organic isocyanates to produce covalently attached amides and carbamate esters from the carboxyl and hydroxyl groups of GO.[73] Remarkably, the resultant isocyanate-modified GO can be intimately mixed with host polymers in polar aprotic solvents, providing a facile synthesis route to graphene-polymer hybrids.[42]

The noncovalent functionalization of graphene typically involves π-π stacking,[74, 75] electrostatic interactions,[76, 77] and hydrogen bonding.[78, 79] Noncovalent functionalization minimizes the damage to the graphitic structure and thus maintains the physical and chemical properties of graphene. In one typical example, in-situ noncovalent functionalization of graphene was achieved by ultrasonic exfoliation of graphite in 1-pyrenecarboxylic acid (PCA) aqueous solution.[80] PCA served as a "molecular wedge" that cleaved individual graphene flakes from graphite and attached on graphene surface via π-π stacking. These intercalated molecules broke the π-bonding of the graphene interlayers and reduced their hydrophobic interactions with water. Moreover, the hydrophilic -COOH groups of PCA enabled the formation of stable aqueous dispersions of graphene, and facilitated filtration of graphene membranes for ultrathin electrochemical capacitor electrode.

1.4 Graphene-based hybrid materials

The intrinsic electrical and chemical properties of graphene, associated with methods available for processing and functionalization, provide an opportunity for the construction of graphene-based hybrid materials (GHMs) with diversified morphology and intriguing properties. In this section, we summarize typical protocols for assembly of GHMs with defined morphology, including core-shell hybrids, two-dimensional (2D) sandwich-like nanosheets and three-dimensional (3D) graphene aerogels/foams.

1.4.1 Core-shell hybrids

Graphene-encapsulated nanomaterials with a core-shell structure have been synthesized by a variety of techniques, including electrostatic forces,[81] hydrophobic interactions,[82] and covalent coupling.[83] Electrostatic forces offer a significant benefit over other methods because of their ease in processing and mild synthesis conditions. In contrast to pristine graphene, hydrophilic GO can form well-dispersed aqueous colloids via electrostatic repulsion. The surface charge (zeta potential) measurement indicates that the GO sheets are highly negatively charged when dispersed in water as a result of ionization of the carboxylic acid and phenolic hydroxyl groups.[59] This feature offers great technological promise for assembly of GO with other functional components to build up core-shell GHMs.

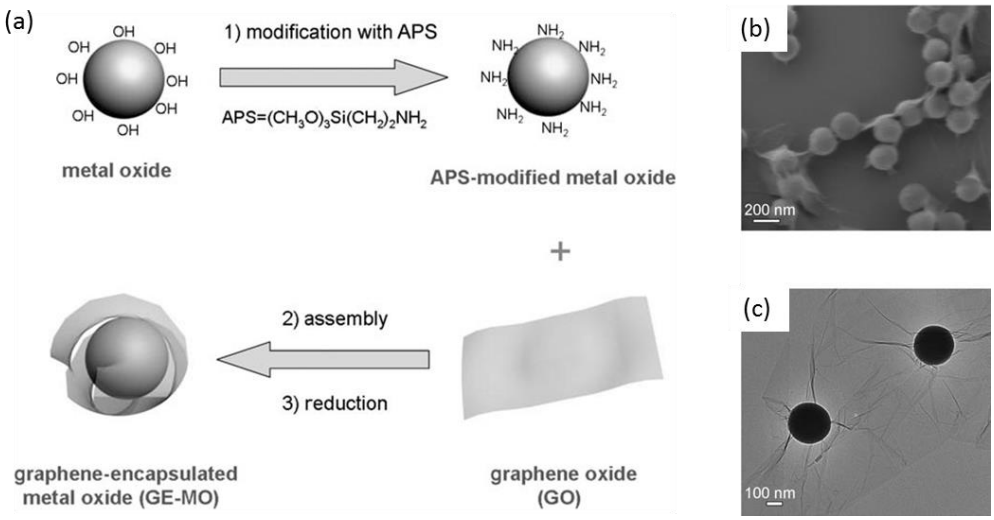

Figure 1.5 (a) Fabrication of graphene-encapsulated metal oxide by coassembly between negatively charged graphene oxide and positively charged oxide nanoparticles; Typical SEM (b) and (c) TEM image of graphene-encapsulated silica spheres.[81]

Our group has demonstrated the feasibility to construct GHMs consisting of oxide nanoparticles (metallic/non-metallic) as cores and graphene sheets as shells.[81] The overall synthetic procedure is illustrated in Figure 1.5a. The oxide nanoparticles (e.g. SiO_2 and Co_3O_4) were modified by aminopropyltrimethoxysilane (APS) to render the particle surface positively charged, and wrapped by negatively charged GO sheets in aqueous solutions. Subsequent chemical reduction of GO with hydrazine gave rise to graphene-encapsulated SiO_2/Co_3O_4 hybrids (Figure 1.5b-c). Core-shell structures provide a prospective solution to accommodate the volume expansion of active materials for lithium storage. In comparison to other carbon-coated hybrid materials, the ultrathin graphene shells not only act as a buffer matrix against volume change during cycling but also preserve a highly active material content (up to 91.5% of Co_3O_4) in the GHMs. Such a simple and low-cost assembly protocol has been extended to build up a series of core-shell hybrids for energy storage applications, such as Si/graphene,[84] Fe_2O_3/graphene,[85] and NiO/graphene.[86]

1.4.2 Two-dimensional sandwich-like nanosheets

The unique 2D morphology and high surface area render graphene a fascinating substrate for creating 2D sandwich-like hybrid materials. GO and RGO are the basic building blocks for the construction of such hybrid materials, since they possess abundant oxygen functional groups which provide preferred reactive sites for the binding of various inorganic/organic species.[87-89] The typical method for preparing 2D inorganic GHMs involves mixing respective salt precursors with GO/RGO suspensions, followed by in-situ reduction of metal salts and GO with reducing agents (e.g. $NaBH_4$, ascorbic acid) [90, 91] or reflux/hydrothermal treatment.[92, 93] As a result, inorganic nanoparticles (NPs) with

diversified morphology and crystallinity anchor on GO/RGO surface via ionic interactions or covalent bonding, and simultaneously prevent the stacking and agglomeration of graphene sheets.

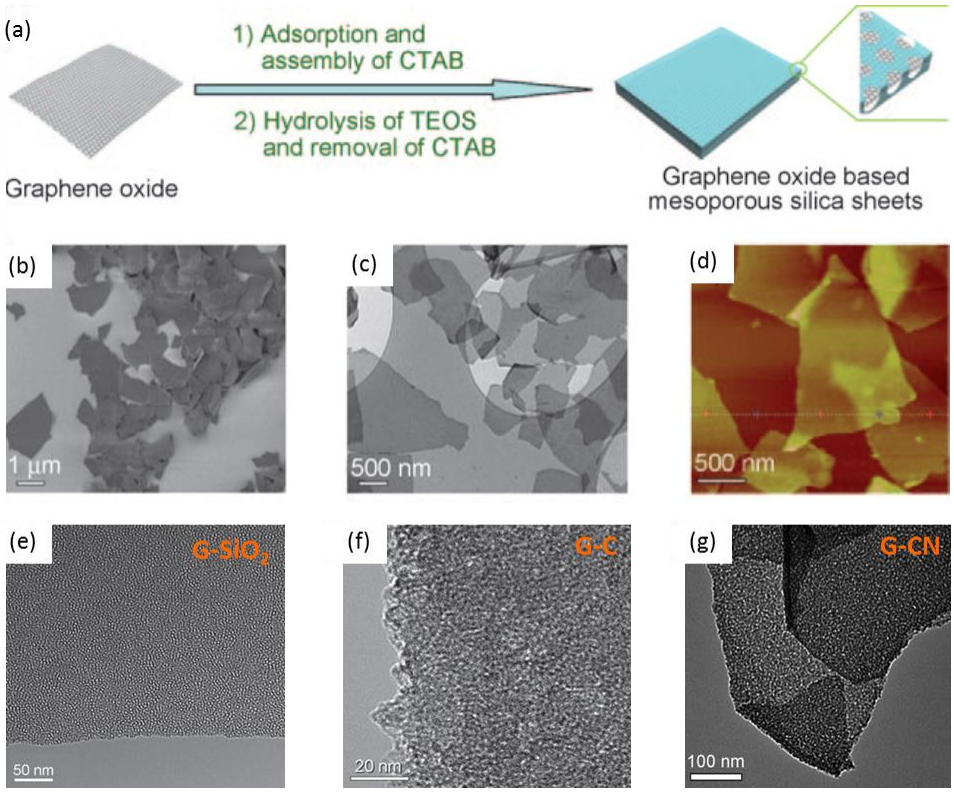

Figure 1.6 (a) Fabrication process for graphene oxide-based mesoporous silica (GOM-silica) nanosheets;[94] (b-d) Representative SEM, TEM and AFM images respectively of as-synthesized GOM-silica nanosheets;[94] Typical HR-TEM image of graphene-based silica (e), carbon (f),[94] and carbon nitride (g) nanosheets.[95]

Although the oxygen functional groups on GO/RGO afford numerous reactive sites for nucleation and anchoring of foreign species, the as-produced 2D hybrid materials generally exhibit a broad and nonuniform distribution of nanoparticles.[96, 97] Thus, the control over the morphology and distribution of functional components is fundamental to optimize the properties and electrochemical performance of GHMs. In our group, a bottom-up approach was developed for the large-scale production of 2D hybrids with graphene sheets

sandwiched by homogeneous mesoporous silica, carbon, or metal oxides layers. In a typical synthesis approach, graphene oxide-based mesoporous silica (GOM-silica) nanosheets were first fabricated via the hydrolysis of tetraethylorthosilicate (TEOS) on the surface of GO with the aid of a cationic surfactant cetyltrimethyl ammonium bromide (CTAB) (Figure 1.6a-d).[94] Herein CTAB served as unique molecular template that electrostatically adsorbed/self-assembled onto GO surface and further directed the nucleation and growth of mesoporous silica around GO sheets. Heat treatment under argon rendered the thermal reduction of GO and afforded graphene-based mesoporous silica nanosheets (GM-silica, Figure 1.6e). The as-obtained GM-silica exhibited a large specific surface area of 980 $m^2 g^{-1}$ and highly uniform mesopore size of 2 nm. Remarkably, the GM-silica could be used as universal template for the creation of various functional nanosheets, such as graphene-based mesoporous carbon, Co_3O_4,[94] TiO_2,[98] and carbon nitride (CN) [95] nanosheets (Figure 1.6 f and g). The resulting 2D GHMs exhibit many unique features such as a large aspect ratio and high surface area, which render them suitable for broad application in energy storage and conversion.

1.4.3 Three-dimensional graphene aerogels/foams

3D graphene assembly, such as aerogels and foams, can provide continuously interconnected macroporous structures with a large surface area, low mass density and multi-dimensional electric/ionic transport pathways. The deposition of graphene on stacking nanospheres (e.g. SiO_2, polystyrene) [99, 100] or porous frameworks (e.g. nickel foam) [101] followed by the elimination of the template can generate graphene materials with 3D macroporous structures. For example, methyl group grafted silica spheres with different

diameters (~28, 60, and 120 nm) were assembled with GO sheets via the hydrophobic interactions between silica surface and GO central planes.[82] Subsequent calcination of the lamellar-like precipitates combined with HF etching of silica template yielded nanoporous graphene foams with controllable pore size. Notably, the graphene frameworks obtained from the smallest silica template (~28 nm in diameter) show a high surface area of 851 m^2 g^{-1} and an ultra-large pore volume of ~4.28 cm^3 g^{-1}, and the majority of pore size are narrowly distributed and quite close to the diameter of silica spheres. Furthermore, the graphene foams can be employed for the generation of functional hybrid materials by simple deposition with metal oxide nanoparticles (e.g. Fe_3O_4).

It was found that the direct chemical reduction of GO in water under hydrothermal treatment or with assistance of reducing agents, such as L-ascorbic acid (Vitamin C),[102] sodium hydrogen sulfite and sodium sulfide,[103] could also produce 3D macroporous structures. In one typical case, controllable assembly of Fe_3O_4 nanoparticles (NPs) supported on 3D nitrogen-doped graphene aerogels (Fe_3O_4/N-GAs) was reported via a combined hydrothermal, freeze-drying, and thermal treatment (Figure 1.7a).[104] The hybrids comprise interconnected, porous 3D graphene frameworks with continuous macropores in the micrometer size range and uniform dispersion of Fe_3O_4 NPs (Figure 1.7b). It is noteworthy that besides the decoration on a graphene surface, a significant portion of the Fe_3O_4 NPs are encapsulated within the graphene layers (Figure 1.7c), suggesting efficient assembly between graphene sheets and Fe_3O_4 NPs. Benefiting from the 3D macroporous structure and high surface area (110 m^2 g^{-1}), the resulting Fe_3O_4/N-GAs displayed excellent electrocatalytic activity for ORR in alkaline electrolytes. Such synthetic strategy could be applied to prepare other 3D graphene-based monolithic materials for the development of novel energy storage devices. For instance, nitrogen- and boron-co-doped

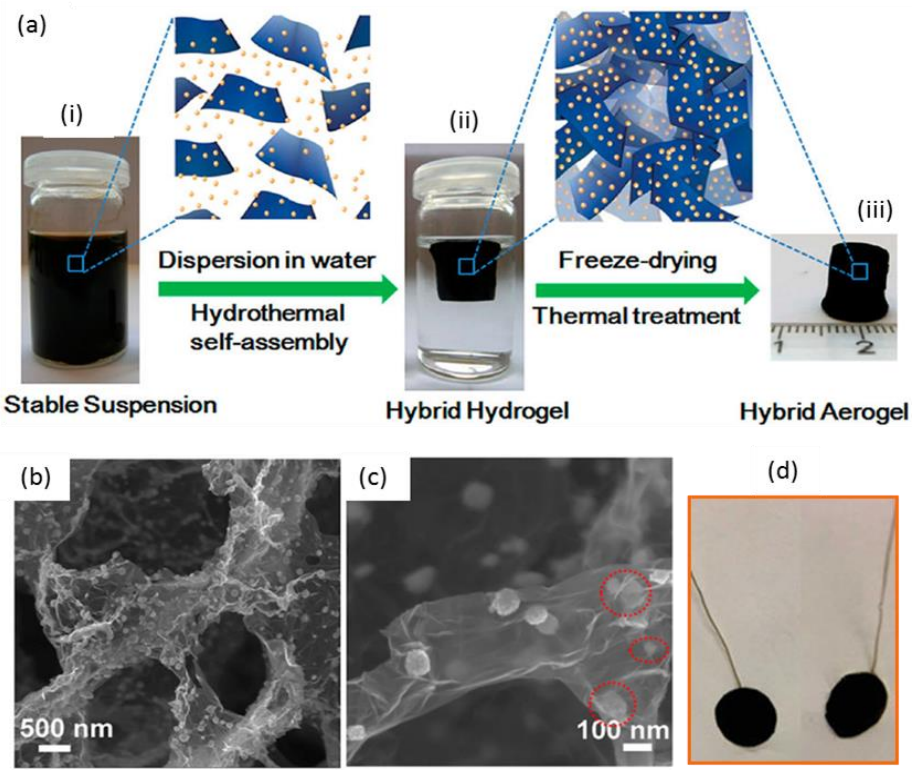

Figure 1.7 (a) Fabrication process for the 3D Fe_3O_4/N-GAs catalyst.[104] (i) stable aqueous suspension of GO, iron ions, and polypyrrole; (ii) graphene hybrid hydrogel synthesized by hydrothermal self-assembly; (iii) monolithic Fe_3O_4/N-GAs hybrid aerogel obtained after freeze-drying and thermal treatment. Inset images: ideal dispersion and assembly model; (b, c) Typical SEM images of as-synthesized Fe_3O_4/N-GAs. The red rings in (c) indicate Fe_3O_4 NPs encapsulated in thin graphene layers;[104] (d) thin electrode plates processed by physical pressing of BN-GAs.[105]

graphene aerogels (BN-GAs) with high surface areas of up to 249 m^2 g^{-1} were fabricated by adding ammonia boron trifluoride (NH_3BF_3) into GO dispersions followed by the same hydrothermal reaction and freeze-drying processes.[105] Importantly, such monolithic BN-GAs could be processed into thin plates (Figure 1.7d) and used as binder-free electrodes for all-solid-state supercapacitors (ASSSs).

1.5 Applications

Construction of hybrid materials via controlled assembly approaches is crucial for the development of high-performance energy storage and conversion devices. In these GHMs, the beneficial role of graphene is manifold, either maximizing the activity of supported nanomaterials or improving the stability/durability of electrode in energy devices. In this section, we focus on the latest advancements on utilizing these GHMs for energy storage and conversion devices, including lithium-ion batteries, supercapacitors and fuel cells.

1.5.1 Lithium-ion batteries

Rechargeable lithium-ion batteries (LiBs) are the representative system for energy storage devices. Compared to conventional nickel-cadmium/lead acid batteries, LiBs exhibit advantages including high energy density, low maintenance, and low self-discharge rate.[106] Each cell of LiBs consists of two electrodes (anode and cathode) and electrolyte, together with separator that allows ion transfer but prohibits electrical contact (Figure 1.8).[107] The commercial LiBs use mostly graphite as the anode host and the layered $LiCoO_2$ compound as the cathode host. A mixture of aprotic solvents (e.g. ethylene carbonate (EC) and diethyl carbonate (DEC)) containing lithium salt ($LiPF_6$) are used as the electrolyte. The operating principle of LiBs is based on Li^+ intercalation/conversion reactions. When the cell is discharged, Li^+ intercalates the graphite through the electrolyte, providing outer electron flow. During charging, Li^+ deintercalates in reverse from the graphite and intercalates the anode. The chemical reaction involved during the cycling is described in Equation (1).[108]

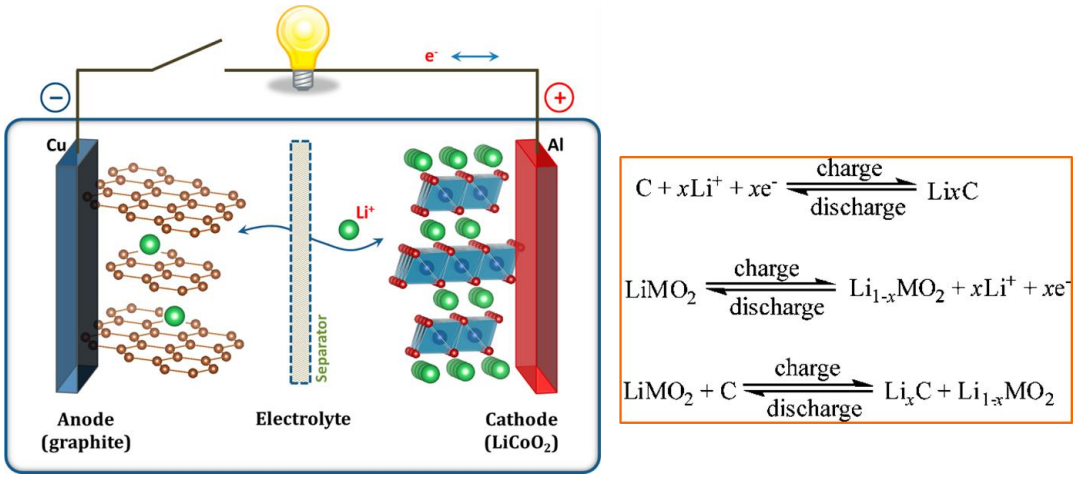

Figure 1.8 Schematic illustration of the traditional LiBs ($LiCoO_2$/Li^+ electrolyte/graphite);[107] Equation (1): chemical reactions involved in the cells.[108]

The poor electronic transport and large volume swing during lithiation/delithiation processes constitute two key problems in most proposed cathode (e.g. $LiMn_2O_4$, S) [109, 110] and anode (e.g. Si, SnO_2) [111, 112] materials. A core-shell structure with active materials encapsulated by graphene layers provides a prospective solution. As a typical example, Co_3O_4 encapsulated with flexible, ultrathin graphene shells (GE-Co_3O_4) exhibited a very high reversible capacity of 1100 mAh g^{-1} in initial 10 cycles and over 1000 mAh g^{-1} after 130 cycles at a current density of 74 mA g^{-1}, which were much higher than that of bare Co_3O_4 and other Co_3O_4/carbon core-shell electrodes (600–850 mAh g^{-1}).[81] The kinetic differences between the two electrodes played an important role in their electrochemical performance, which was validated by electrochemical impedance spectroscopy (EIS) measurement after 30 cycles. Nyquist plots showed that the diameter of the semicircle for GE-Co_3O_4 electrodes in the high-medium frequency region was much smaller than that of bare Co_3O_4 electrodes, thus suggesting that GE-Co_3O_4 electrodes had lower contact and charge-transfer impedances. These results confirmed that the graphene shells not only

served as buffer matrix and conducting pathways of the overall electrode, but also largely improved the electrochemical activity of Co_3O_4 during the cycling.

1.5.2 Supercapacitors

Supercapacitors (SCs) are promising candidates as alternative energy storage devices owing to their high rate capability, high power density and long cycle life.[113] SCs can be classified into two categories: the electrical-double-layer capacitors (EDLCs) and pseudocapacitors. The EDLCs store energy via the adsorption of electrolyte ions on the porous electrode materials (e.g. activated carbon), while the pseudocapacitors store energy via the fast and reversible redox reactions of the electro-active materials (e.g. transition metal oxides, conducting polymers).[114, 115] Figure 1.9a illustrates the typical EDLCs profiles, comprising two nonreactive porous electrodes immersed in an electrolyte and a separator located between the electrodes. During the charge process, anions transport to the surface of the positive electrode and cations transport to the negative electrode, forming electrical double layers at the interface. When the stored energy is released, the adsorbed electrolyte ions release to the solutions.[116]

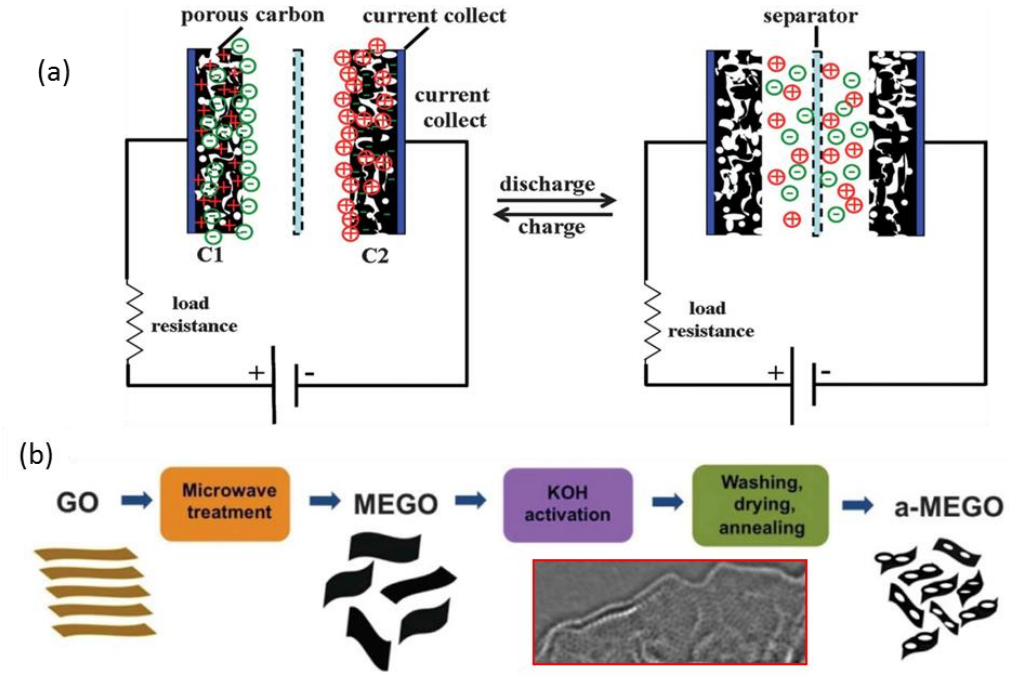

Figure 1.9 (a) Schematic diagram of the charged and discharged electric double layer capacitor;[116] (b) Schematic showing the microwave exfoliation/reduction of GO and the following chemical activation of MEGO with KOH that creates pores while retaining high electrical conductivity (inset: HR-TEM image from the edge of a-MEGO).[117]

The performance of electrode materials for EDLCs is intimately dependent on both the accessible specific surface area and the pore structure. In this regard, porous GHMs have been at the focus of research due to the beneficial combination of the excellent electrical properties and large surface area. A significant progress was achieved for KOH-activated microwave exfoliated GO (a-MEGO, Figure 1.10b) with an ultra-high surface area up to 3100 m^2 g^{-1}, high electrical conductivity of 500 S m^{-1}, and low oxygen and hydrogen content as the symmetrical SCs electrode.[117] The HR-TEM image indicated that the activation process introduced numerous micro- and mesopores with a pore size distribution between ~1 and ~10 nm in a-MEGO (inset of Figure 1.9b). The specific capacitance calculated from the discharge curves at current densities of 5.7 A g^{-1} was 166 F g^{-1}, giving

rise to a high energy and power density of ~70Wh kg^{-1} and ~250 kW kg^{-1} respectively. Moreover, the practical energy and power density based on 30wt% active electrode material in a packaged supercapacitor device was calculated to be ~21 Wh kg^{-1} and ~75 kW kg^{-1} respectively, which was much higher than the values from existing activated carbon-based supercapacitors or commercial carbon supercapacitors (4~5Wh kg^{-1}).[118]

1.5.3 Fuel cells

Proton exchange membrane fuel cells (PEMFC) have been recognized as high efficiency, low pollution power generators for stationary and electric vehicle applications.[119, 120] A PEMFC is made of a solid electrolyte membrane sandwiched between anode and cathode electrodes (Figure 1.10a).[121] The power is electrochemically generated when the fuel (e.g. hydrogen) is passed over the anode and oxygen (e.g. air) over the cathode. Precious-metal catalysts, like platinum (Pt) supported on carbon, have been predominantly used for the oxidation of the fuel (anode) and reduction of the oxygen (cathode) in fuel cells.[122-124] For commercial viability, however, PEMFCs must overcome the barrier of high cost caused by the exclusive use of Pt-based catalysts at the cathode, due to the slow kinetics of the cathodic oxygen reduction reaction (ORR).[125, 126]

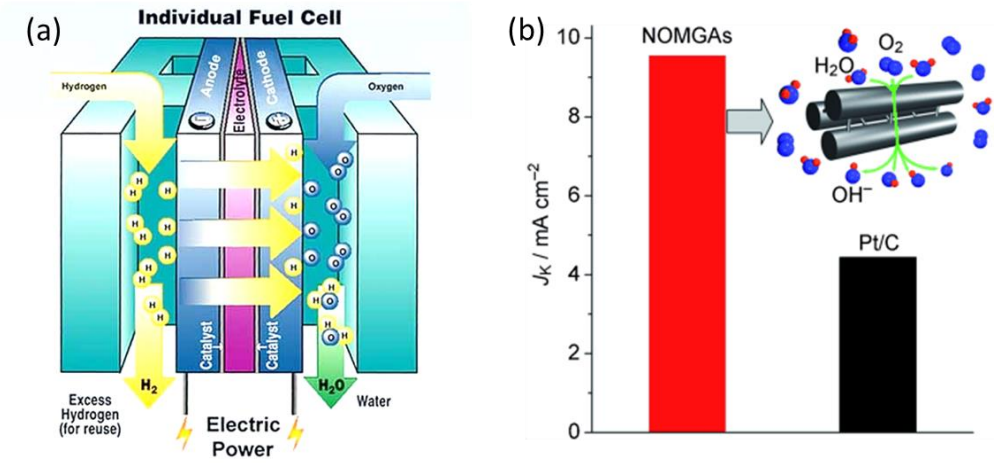

Figure 1.10 (a) Schematic diagram of the PEMFC;[121] (b) Electrochemical activity given as the kinetic-limiting current density (J_k) for the nitrogen-doped carbon in comparison with that of a commercial Pt-C electrode.[127]

Tremendous efforts have been devoted to fabricating highly active and stable, yet low-cost ORR electrocatalysts, including no-precious metal (e.g. Fe, Co, Ni) [128] and metal-free catalysts (e.g. heteroatom doped CNTs/graphene, carbon nitride).[129] Although non-precious metal catalysts play a major role in various industrial processes, they still suffer from some disadvantages including poor durability and environmental poisoning.[130] Recently, nitrogen-doped metal-free carbon materials (NMCs) have become prominent catalyst candidates for high-efficient ORR processes.[131-133] For example, our group developed a novel NMCs catalyst comprising ordered mesoporous graphitic arrays (NOMGAs) using SBA-15 as template and nitrogen-containing aromatic dyestuff as carbon precursor.[127] The resultant NOMGAs possess remarkable electrocatalytic properties, including higher electrocatalytic activity, longer term stability, and improved resistance to crossover effects for ORR compared to commercialized Pt catalyst (Figure 1.10b). Although the nature of active ORR catalytic sites in NMCs remains controversial, both

theoretical studies and experimental observations indicate that the nitrogen heteroatom create net positive charge on adjacent carbon atoms and modulate the electronic property and catalytic activity of carbon catalysts.[134, 135] Nevertheless, the electrochemical activities of NMCs towards ORR need to be much improved. The production of NMCs with well-defined nanostructures and enhanced ORR activity is still a highly attractive synthetic target.

1.6 Motivation and objectives

As discussed above, graphene has emerged as the most significant carbon material in the last decade. The unprecedented physical and chemical properties including high electrical conductivity, excellent mechanical and chemical stability, make graphene a promising electrode material for different energy storage and conversion devices. The development of hybrid materials using graphene as the building blocks is the key given that the remarkable properties of graphene can be translated to the frameworks of hybrids and simultaneously promote the electrochemical performance of the major components. The maximum improvements in ultimate device properties can only be achieved when the electrochemically active materials are homogeneously dispersed in hybrid matrix and the graphene is efficiently integrated through strong interfacial bonding. However, the conventional method for preparing GHMs involves mechanically mixing/stacking or direct pyrolysis of the compounds and frequently fails in controlling the morphology and uniformity, thus leading to limited interfacial interactions and poor device performance. Therefore, rational design and controlled assembly of GHMs which aim at construction of well-defined nanostructures is of great concern.

The assembly of GHMs should also be guided by the end-application of the materials. LiBs require a stable electrode structure in order to accommodate the volume change of active materials and improve their lifetime. Thus, construction of a robust carbon matrix based on ultrathin and chemically inert graphene sheets is highly desirable. In regard to SCs and FCs, the device performance is determined by the intrinsic nature of charge adsorption and catalytic active sites of electrode materials. Therefore, the decoration of graphene with uniform porous components to facilitate fast mass-transport kinetics coupled with tailored

mesopore size for optimized charge storage/active site density is highly appealing. On the other hand, high-quality graphene produced by electrochemical exfoliation of graphite (EEG) already holds a great promise for replacing GO/RGO to produce novel GHMs on a large scale and low cost. Therefore, both the functionalization of EEG and controlled assembly of EEG hybrids are also urgently required.

In this thesis, we will focus on the following directions to demonstrate the controllable assembly of GHMs and address the specific applications of well-defined GHMs as high-performance electrode materials for lithium storage, supercapacitors and oxygen reduction reaction.

(1) The poor electronic transport and large volume expansion during lithiation/delithiation processes constitute two major obstacles for developing high-performance lithium storage materials. Graphene-based core-shell structure could partially alleviate the pulverization induced by the volume changes of active materials. However, owing to poor interfacial interactions between graphene shells and active materials, such architecture failed to afford constant protection against the severe volume change and high stresses within electrode, especially operated at high current rate and over a large number of cycles. In Chapter 2, we propose a novel strategy to construct 3D graphene foams that integrate graphene/Fe_3O_4 core-shell structure with interconnected graphene frameworks. Remarkably, such hierarchical framework structure provides double protection against the volume changes of embedded Fe_3O_4 nanoparticles, that is, the interior graphene shells buffer the volume expansion of Fe_3O_4 while the interconnected 3D graphene networks act to reinforce the core-shell structure. As a result, the 3D graphene/Fe_3O_4 hybrids deliver a high reversible capacity of 1059 mAh g^{-1} over 150 cycles (at 93 mA g^{-1}), and excellent rate

capability (363 mAh g^{-1} at 4.8 A g^{-1}). Such a protocol to construct 3D hierarchical graphene frameworks can be extended to other battery electrode materials that experience large volumetric swing during cycling.

(2) The porosity features serve as key component in high-performance SCs devices. Despite the significant progress in synthesizing porous GHMs, the following two key points remain to be addressed. First, the accessible surface areas of these porous GHMs is very low, mainly attributable to the strong aggregation of graphene and the random distribution of porous components; second, the control over pore morphology and size distribution is limited, which substantially impedes the efficiency of mass transport and charge storage. In Chapter 3, we will describe a novel synthetic approach to engineer the surface porosity of graphene and construct highly porous carbon nanosheets (HPCN) via a combined template and nanocasting technology. Successful control over pore size distribution of HPCN is realized by self-assembly of colloidal silica nanoparticles on graphene surface. We find that porosity regulation over HPCN exerts essential influence on the physicochemical properties and their capacitive behavior for SCs. The as-synthesized HPCN exhibits a specific surface area of 1270 m^2 g^{-1} and pore volume of 2.64 cm^3 g^{-1}, both of which are higher than that of physically mixed porous carbon nanosheets (PCNs, 910 m^2 g^{-1} and 1.15 cm^3 g^{-1} respectively). The open and ultrathin mesoporous shells of HPCN enable full accessibility of electrolyte and provide sufficient charge accommodations within electrode. Electrical-double-layer capacitor employing HPCN as electrode exhibits a specific capacitance of 222 F g^{-1} at a scan rate of 1 mV s^{-1}, which is much higher than that of PCNs (157 F g^{-1}) and non-porous carbon nanosheets (CNs, 103 F g^{-1}). Further, we demonstrate that HPCN can serve as novel 2D carbon matrix for incorporation of metal oxide (e.g. RuO_2) for pseudocapacitors.

(3) Nitrogen-doped carbon materials hold great promise to replace high-cost platinum catalysts for efficient oxygen reduction reaction in fuel cells. The unique planar structure with atomic thickness renders graphene a suitable substrate for creating N-doped GHMs containing numerous catalytic sites with the promise of efficient transport pathways. However, metal-free N-doped graphene catalysts still suffer from low activity in either alkaline or acidic media, mostly because of the few amount or limited exposure of ORR catalytic sites. To address this issue, we develop a series of metal-free nitrogen-doped carbon nanosheets (NDCN) with uniform and tuneable mesopores in Chapter 4. Porosity control over NDCN is achieved by developing appropriate graphene/silica nanosheet template followed by surface coating with polydopamine (PDA). Pyrolysis of nitrogen-rich PDA layer and removal of silica template yield NDCN with size-defined mesopores which have exposed highly electroactive and stable catalytic sites. The prepared NDCN catalysts possess high specific surface area in a range of 578-652 m^2 g^{-1}. This synthetic strategy appears to boost the electrocatalytic activity of metal-free N-doped catalysts via controlled mesoporosity. Remarkably, NDCN with defined mesopore size of 22 nm exhibits the highest ORR performance, with a well-defined plateaux for the diffusion-limiting current and a more positive onset potential than that of a Pt/C catalyst in an alkaline medium (-0.01 V vs. -0.02 V). Moreover, it manifests pronounced catalytic activity in acidic medium, with mainly a 4-electron transfer process and positive ORR onset potential of 0.72 V. This study suggests that the electrocatalytic activity of NDCN catalysts is highly dependent on their pore size. Upon increasing the mesopore size, ORR performance in both alkaline and acidic medium increases, as verified by the onset potential and the diffusion-limiting current.

(4) Previous studies on controllable assembly of GHMs are mainly based on GO sheets. Although GO can be produced in bulk scale with good solution processability, a

large amount of defect density and low electrical conductivity constitutes the major drawbacks towards advanced energy storage and conversion applications. Recently, electrochemically exfoliated graphene (EEG) has attracted attention due to the high quality and ease in synthesis. However, owing to the hydrophobic nature and inert surface properties, solution processing of EEG and assembly of EEG-based hybrid materials remain challenging issues. In Chapter 5, for the first time, we describe a novel strategy to modulate surface property of EEG and direct assembly of EEG with a series of inorganic functional nanoparticles (e.g. Si, Fe_3O_4 and Pt NPs). Polyaniline (PANI), in the emeraldine base form, serves as bi-functional linker to bridge the counterparts of EEG and functional NPs. The backbone rings of PANB spontaneously adsorb on EEG surface via π-π interactions, whereas the exposed amine/imine groups act as numerous active sites for binding with functional NPs via electrostatic force and hydrogen bonding. Such a protocol is versatile and cost-effective for production of various 2D EEG hybrids, such as EEG-Si, EEG-Fe_3O_4 and EEG-Pt, interesting for a variety of possible applications. As exemplified by EEG-Si hybrids serving as anode material for lithium storage, a high initial reversible capacity (2357 mAh g^{-1} at 105 mA g^{-1}) and excellent cycling stability (86% capacity retention after 100 cycles at 1 A g^{-1}) are achieved. Even at a high current density of 8.4 A g^{-1}, a reversible capacity of 460 mAh g^{-1} is maintained with excellent cycling stability.

1.7 References

[1] A. Manthiram, A. Vadivel Murugan, A. Sarkar, T. Muraliganth, *Energy Environ. Sci.* **2008**, *1*, 621.

[2] M. Winter, R. J. Brodd, *Chem. Rev.* **2004**, *104*, 4245.

[3] N.-S. Choi, Z. Chen, S. A. Freunberger, X. Ji, Y.-K. Sun, K. Amine, G. Yushin, L. F. Nazar, J. Cho, P. G. Bruce, *Angew. Chem. Int. Ed.* **2012**, *51*, 9994.

[4] M. S. Whittingham, *MRS Bull.* **2008**, *33*, 411.

[5] S. Chu, A. Majumdar, *Nature* **2012**, *488*, 294.

[6] D. Eder, *Chem. Rev.* **2010**, *110*, 1348.

[7] M. M. Ottakam Thotiyl, S. A. Freunberger, Z. Peng, P. G. Bruce, *J. Am. Chem. Soc.* **2012**, *135*, 494.

[8] H. Nishihara, T. Kyotani, *Adv. Mater.* **2012**, *24*, 4473.

[9] E. Hammel, X. Tang, M. Trampert, T. Schmitt, K. Mauthner, A. Eder, P. Pötschke, *Carbon* **2004**, *42*, 1153.

[10] W. Wei, J. Wang, L. Zhou, J. Yang, B. Schumann, Y. NuLi, *Electrochem. Commun.* **2011**, *13*, 399.

[11] C. N. R. Rao, A. K. Sood, K. S. Subrahmanyam, A. Govindaraj, *Angew. Chem. Int. Ed.* **2009**, *48*, 7752.

[12] M. J. Allen, V. C. Tung, R. B. Kaner, *Chem. Rev.* **2009**, *110*, 132.

[13] L. Rodriguez-Perez, M. a. A. Herranz, N. Martin, *Chem. Commun.* **2013**, *49*, 3721.

[14] N. G. Sahoo, Y. Pan, L. Li, S. H. Chan, *Adv. Mater.* **2012**, *24*, 4203.

[15] X. Huang, Z. Yin, S. Wu, X. Qi, Q. He, Q. Zhang, Q. Yan, F. Boey, H. Zhang, *Small* **2011**, *7*, 1876.

[16] D. R. Dreyer, R. S. Ruoff, C. W. Bielawski, *Angew. Chem. Int. Ed.* **2010**, *49*, 9336.

[17] J. Liu, X.-W. Liu, *Adv. Mater.* **2012**, *24*, 4097.

[18] K. Parvez, Z.-S. Wu, R. Li, X. Liu, R. Graf, X. Feng, K. Müllen, *J. Am. Chem. Soc.* **2014**, *136*, 6083.

[19] C. Berger, Z. Song, X. Li, X. Wu, N. Brown, C. Naud, D. Mayou, T. Li, J. Hass, A. N. Marchenkov, E. H. Conrad, P. N. First, W. A. de Heer, *Science* **2006**, *312*, 1191.

[20] A. K. Geim, K. S. Novoselov, *Nat. Mater.* **2007**, *6*, 183.

[21] K. S. Novoselov, D. Jiang, F. Schedin, T. J. Booth, V. V. Khotkevich, S. V. Morozov, A.

K. Geim, *Proc. Natl. Acad. Sci. USA* **2005**, *102*, 10451.

[22] K. S. Novoselov, A. K. Geim, S. V. Morozov, D. Jiang, Y. Zhang, S. V. Dubonos, I. V. Grigorieva, A. A. Firsov, *Science* **2004**, *306*, 666.

[23] A. K. Geim, *Science* **2009**, *324*, 1530.

[24] J. C. Meyer, A. K. Geim, M. I. Katsnelson, K. S. Novoselov, T. J. Booth, S. Roth, *Nature* **2007**, *446*, 60.

[25] E. Stolyarova, K. T. Rim, S. Ryu, J. Maultzsch, P. Kim, L. E. Brus, T. F. Heinz, M. S. Hybertsen, G. W. Flynn, *Proc. Natl. Acad. Sci. USA* **2007**, *104*, 9209.

[26] M. D. Stoller, S. Park, Y. Zhu, J. An, R. S. Ruoff, *Nano Lett.* **2008**, *8*, 3498.

[27] Z. Hu, M. P. Srinivasan, *Microporous Mesoporous Mater.* **2001**, *43*, 267.

[28] M. Ishigami, J. H. Chen, W. G. Cullen, M. S. Fuhrer, E. D. Williams, *Nano Lett.* **2007**, *7*, 1643.

[29] E. Hwang, S. Adam, S. Das Sarma, *Phys. Rev. Lett.* **2007**, *98*, 186806.

[30] A. Castro Neto, F. Guinea, N. Peres, K. Novoselov, A. Geim, *Rev. Mod. Phys.* **2009**, *81*, 109.

[31] A. Shytov, M. Rudner, N. Gu, M. Katsnelson, L. Levitov, *Solid State Commun.* **2009**, *149*, 1087.

[32] K. S. Novoselov, A. K. Geim, S. V. Morozov, D. Jiang, M. I. Katsnelson, I. V. Grigorieva, S. V. Dubonos, A. A. Firsov, *Nature* **2005**, *438*, 197.

[33] A. S. Mayorov, R. V. Gorbachev, S. V. Morozov, L. Britnell, R. Jalil, L. A. Ponomarenko, P. Blake, K. S. Novoselov, K. Watanabe, T. Taniguchi, *Nano Lett.* **2011**, *11*, 2396.

[34] F. Miao, S. Wijeratne, Y. Zhang, U. C. Coskun, W. Bao, C. N. Lau, *Science* **2007**, *317*, 1530.

[35] K. I. Bolotin, K. Sikes, Z. Jiang, M. Klima, G. Fudenberg, J. Hone, P. Kim, H. Stormer, *Solid State Commun.* **2008**, *146*, 351.

[36] A. M. Ilyin, E. A. Daineko, G. W. Beall, *Physica E: Low-dimensional Systems and Nanostructures* **2009**, *42*, 67.

[37] G. Compagnini, F. Giannazzo, S. Sonde, V. Raineri, E. Rimini, *Carbon* **2009**, *47*, 3201.

[38] S. Adam, E. H. Hwang, E. Rossi, S. Das Sarma, *Solid State Commun.* **2009**, *149*, 1072.

[39] J.-H. Chen, W. Cullen, C. Jang, M. Fuhrer, E. Williams, *Phys. Rev. Lett.* **2009**, *102*, 236805.

[40] M. Acik, G. Lee, C. Mattevi, M. Chhowalla, K. Cho, Y. J. Chabal, *Nat. Mater.* **2010**, *9*, 840.

[41] C. Gómez-Navarro, R. T. Weitz, A. M. Bittner, M. Scolari, A. Mews, M. Burghard, K. Kern, *Nano Lett.* **2007**, *7*, 3499.

[42] V. Singh, D. Joung, L. Zhai, S. Das, S. I. Khondaker, S. Seal, *Prog. Mater Sci.* **2011**, *56*, 1178.

[43] C. Lee, X. Wei, J. W. Kysar, J. Hone, *Science* **2008**, *321*, 385.

[44] H. Y. Nan, Z. H. Ni, J. Wang, Z. Zafar, Z. X. Shi, Y. Y. Wang, *J. Raman Spectrosc.* **2013**, *44*, 1018.

[45] S. Stankovich, D. A. Dikin, R. D. Piner, K. A. Kohlhaas, A. Kleinhammes, Y. Jia, Y. Wu, S. T. Nguyen, R. S. Ruoff, *Carbon* **2007**, *45*, 1558.

[46] A. Reina, X. Jia, J. Ho, D. Nezich, H. Son, V. Bulovic, M. S. Dresselhaus, J. Kong, *Nano Lett.* **2008**, *9*, 30.

[47] X. Li, W. Cai, J. An, S. Kim, J. Nah, D. Yang, R. Piner, A. Velamakanni, I. Jung, E. Tutuc, *Science* **2009**, *324*, 1312.

[48] S. Bae, H. Kim, Y. Lee, X. Xu, J.-S. Park, Y. Zheng, J. Balakrishnan, T. Lei, H. R. Kim, Y. I. Song, *Nat. Nanotechnol.* **2010**, *5*, 574.

[49] Y. Hernandez, V. Nicolosi, M. Lotya, F. M. Blighe, Z. Sun, S. De, I. T. McGovern, B. Holland, M. Byrne, Y. K. Gun'Ko, J. J. Boland, P. Niraj, G. Duesberg, S. Krishnamurthy, R. Goodhue, J. Hutchison, V. Scardaci, A. C. Ferrari, J. N. Coleman, *Nat. Nanotechnol.* **2008**, *3*, 563.

[50] F. Torrisi, T. Hasan, W. Wu, Z. Sun, A. Lombardo, T. S. Kulmala, G.-W. Hsieh, S. Jung, F. Bonaccorso, P. J. Paul, D. Chu, A. C. Ferrari, *ACS Nano* **2012**, *6*, 2992.

[51] A. M. Abdelkader, I. A. Kinloch, R. A. Dryfe, *ACS Appl. Mater. Interfaces* **2014**, *6*, 1632.

[52] L. Wu, W. Li, P. Li, S. Liao, S. Qiu, M. Chen, Y. Guo, Q. Li, C. Zhu, L. Liu, *Small* **2014**, *10*, 1421.

[53] Y. Liang, D. Wu, X. Feng, K. Müllen, *Adv. Mater.* **2009**, *21*, 1679.

[54] W. S. Hummers, R. E. Offeman, *J. Am. Chem. Soc.* **1958**, *80*, 1339.

[55] L. Chen, Y. Hernandez, X. Feng, K. Müllen, *Angew. Chem. Int. Ed.* **2012**, *51*, 7640.

[56] A. Narita, X. Feng, Y. Hernandez, S. A. Jensen, M. Bonn, H. Yang, I. A. Verzhbitskiy, C. Casiraghi, M. R. Hansen, A. H. R. Koch, G. Fytas, O. Ivasenko, B. Li, K. S. Mali, T.

Balandina, S. Mahesh, S. De Feyter, K. Müllen, *Nat. Chem.* **2014**, *6*, 126.

[57] H. He, J. Klinowski, M. Forster, A. Lerf, *Chem. Phys. Lett.* **1998**, *287*, 53.

[58] S. Park, J. An, J. R. Potts, A. Velamakanni, S. Murali, R. S. Ruoff, *Carbon* **2011**, *49*, 3019.

[59] D. Li, M. B. Müller, S. Gilje, R. B. Kaner, G. G. Wallace, *Nat. Nanotechnol.* **2008**, *3*, 101.

[60] H. A. Becerril, J. Mao, Z. Liu, R. M. Stoltenberg, Z. Bao, Y. Chen, *ACS Nano* **2008**, *2*, 463.

[61] X. Gao, J. Jang, S. Nagase, *J. Phys. Chem. C* **2009**, *114*, 832.

[62] S. D. Perera, R. G. Mariano, N. Nijem, Y. Chabal, J. P. Ferraris, K. J. Balkus Jr, *J. Power Sources* **2012**, *215*, 1.

[63] T. Kar, R. Devivaraprasad, R. K. Singh, B. Bera, M. Neergat, *RSC Adv.* **2014**, *4*, 57781.

[64] K. Parvez, R. Li, S. R. Puniredd, Y. Hernandez, F. Hinkel, S. Wang, X. Feng, K. Müllen, *ACS Nano* **2013**, *7*, 3598.

[65] C.-Y. Su, A.-Y. Lu, Y. Xu, F.-R. Chen, A. N. Khlobystov, L.-J. Li, *ACS Nano* **2011**, *5*, 2332.

[66] J. H. Lee, D. W. Shin, V. G. Makotchenko, A. S. Nazarov, V. E. Fedorov, Y. H. Kim, J. Y. Choi, J. M. Kim, J. B. Yoo, *Adv. Mater.* **2009**, *21*, 4383.

[67] X. Wang, P. F. Fulvio, G. A. Baker, G. M. Veith, R. R. Unocic, S. M. Mahurin, M. Chi, S. Dai, *Chem. Commun.* **2010**, *46*, 4487.

[68] J. Lu, J.-x. Yang, J. Wang, A. Lim, S. Wang, K. P. Loh, *ACS Nano* **2009**, *3*, 2367.

[69] N. Liu, F. Luo, H. Wu, Y. Liu, C. Zhang, J. Chen, *Adv. Funct. Mater.* **2008**, *18*, 1518.

[70] J. Park, M. Yan, *Acc. Chem. Res.* **2012**, *46*, 181.

[71] V. Georgakilas, M. Otyepka, A. B. Bourlinos, V. Chandra, N. Kim, K. C. Kemp, P. Hobza, R. Zboril, K. S. Kim, *Chem. Rev.* **2012**, *112*, 6156.

[72] X. Zhuang, F. Zhang, D. Wu, N. Forler, H. Liang, M. Wagner, D. Gehrig, M. R. Hansen, F. Laquai, X. Feng, *Angew. Chem.* **2013**, *125*, 9850.

[73] S. Stankovich, R. D. Piner, S. T. Nguyen, R. S. Ruoff, *Carbon* **2006**, *44*, 3342.

[74] Q. Su, S. Pang, V. Alijani, C. Li, X. Feng, K. Müllen, *Adv. Mater.* **2009**, *21*, 3191.

[75] L. Q. Xu, L. Wang, B. Zhang, C. H. Lim, Y. Chen, K.-G. Neoh, E.-T. Kang, G. D. Fu, *Polymer* **2011**, *52*, 2376.

[76] H. Li, S. Pang, S. Wu, X. Feng, K. Müllen, C. Bubeck, *J. Am. Chem. Soc.* **2011**, *133*, 9423.

[77] Y. Liu, Y. Liu, H. Feng, Y. Wu, L. Joshi, X. Zeng, J. Li, *Biosens. Bioelectron.* **2012**, *35*, 63.

[78] N. V. Medhekar, A. Ramasubramaniam, R. S. Ruoff, V. B. Shenoy, *ACS Nano* **2010**, *4*, 2300.

[79] Y. Xu, Q. Wu, Y. Sun, H. Bai, G. Shi, *ACS Nano* **2010**, *4*, 7358.

[80] X. An, T. Simmons, R. Shah, C. Wolfe, K. M. Lewis, M. Washington, S. K. Nayak, S. Talapatra, S. Kar, *Nano Lett.* **2010**, *10*, 4295.

[81] S. Yang, X. Feng, S. Ivanovici, K. Müllen, *Angew. Chem. Int. Ed.* **2010**, *49*, 8408.

[82] X. Huang, K. Qian, J. Yang, J. Zhang, L. Li, C. Yu, D. Zhao, *Adv. Mater.* **2012**, *24*, 4419.

[83] Q. Liu, J. Shi, J. Sun, T. Wang, L. Zeng, G. Jiang, *Angew. Chem. Int. Ed.* **2011**, *50*, 5913.

[84] X. Zhou, Y.-X. Yin, L.-J. Wan, Y.-G. Guo, *Adv. Energy Mater.* **2012**, *2*, 1086.

[85] W. Zhou, J. Zhu, C. Cheng, J. Liu, H. Yang, C. Cong, C. Guan, X. Jia, H. J. Fan, Q. Yan, C. M. Li, T. Yu, *Energy Environ. Sci.* **2011**, *4*, 4954.

[86] W. Yue, Z. Lin, S. Jiang, X. Yang, *J. Mater. Chem.* **2012**, *22*, 16318.

[87] Z. S. Wu, D. W. Wang, W. Ren, J. Zhao, G. Zhou, F. Li, H. M. Cheng, *Adv. Funct. Mater.* **2010**, *20*, 3595.

[88] Z.-S. Wu, W. Ren, L. Wen, L. Gao, J. Zhao, Z. Chen, G. Zhou, F. Li, H.-M. Cheng, *ACS Nano* **2010**, *4*, 3187.

[89] X. Zhuang, F. Zhang, D. Wu, X. Feng, *Adv. Mater.* **2014**, *26*, 3081.

[90] Y.-K. Kim, H.-K. Na, Y. W. Lee, H. Jang, S. W. Han, D.-H. Min, *Chem. Commun.* **2010**, *46*, 3185.

[91] Y. Xin, J.-g. Liu, Y. Zhou, W. Liu, J. Gao, Y. Xie, Y. Yin, Z. Zou, *J. Power Sources* **2011**, *196*, 1012.

[92] H. Wang, H. S. Casalongue, Y. Liang, H. Dai, *J. Am. Chem. Soc.* **2010**, *132*, 7472.

[93] S. Yang, Y. Sun, L. Chen, Y. Hernandez, X. Feng, K. Müllen, *Sci. Rep.* **2012**, *2*, 427.

[94] G. Xie, P. Xi, H. Liu, F. Chen, L. Huang, Y. Shi, F. Hou, Z. Zeng, C. Shao, J. Wang, *J. Mater. Chem.* **2012**, *22*, 1033.

[95] Q. Min, X. Zhang, H. Zhang, F. Zhou, J.-J. Zhu, *Chem. Commun.* **2011**, *47*, 11709.

[96] S. Yang, X. Feng, L. Wang, K. Tang, J. Maier, K. Müllen, *Angew. Chem. Int. Ed.* **2010**, *49*, 4795.

[97] S. Yang, X. Feng, X. Wang, K. Müllen, *Angew. Chem. Int. Ed.* **2011**, *50*, 5339.

[98] S. Yang, X. Feng, K. Müllen, *Adv. Mater.* **2011**, *23*, 3575.

[99] B. G. Choi, M. Yang, W. H. Hong, J. W. Choi, Y. S. Huh, *ACS Nano* **2012**, *6*, 4020.

[100] T. Li, N. Li, J. Liu, K. Cai, M. F. Foda, X. Lei, H. Han, *Nanoscale* **2015**.

[101] Z. Chen, W. Ren, L. Gao, B. Liu, S. Pei, H.-M. Cheng, *Nat. Mater.* **2011**, *10*, 424.

[102] X. Zhang, Z. Sui, B. Xu, S. Yue, Y. Luo, W. Zhan, B. Liu, *J. Mater. Chem.* **2011**, *21*, 6494.

[103] W. Chen, L. Yan, *Nanoscale* **2011**, *3*, 3132.

[104] Z.-S. Wu, S. Yang, Y. Sun, K. Parvez, X. Feng, K. Müllen, *J. Am. Chem. Soc.* **2012**, *134*, 9082.

[105] Z. S. Wu, A. Winter, L. Chen, Y. Sun, A. Turchanin, X. Feng, K. Müllen, *Adv. Mater.* **2012**, *24*, 5130.

[106] I. Hadjipaschalis, A. Poullikkas, V. Efthimiou, *Renewable and Sustainable Energy Reviews* **2009**, *13*, 1513.

[107] J. B. Goodenough, K.-S. Park, *J. Am. Chem. Soc.* **2013**, *135*, 1167.

[108] F. Cheng, Z. Tao, J. Liang, J. Chen, *Chem. Mater.* **2008,** *20*, 667.

[109] M. Hirayama, H. Ido, K. Kim, W. Cho, K. Tamura, J. i. Mizuki, R. Kanno, *J. Am. Chem. Soc.* **2010**, *132*, 15268.

[110] W. Zhou, Y. Yu, H. Chen, F. J. DiSalvo, H. c. D. Abruña, *J. Am. Chem. Soc.* **2013**, *135*, 16736.

[111] N. Liu, Z. Lu, J. Zhao, M. T. McDowell, H.-W. Lee, W. Zhao, Y. Cui, *Nat. Nanotechnol.* **2014**, *9*, 187.

[112] Y. Su, S. Li, D. Wu, F. Zhang, H. Liang, P. Gao, C. Cheng, X. Feng, *ACS Nano* **2012**, *6*, 8349.

[113] Y. Huang, J. Liang, Y. Chen, *Small* **2012**, *8*, 1805.

[114] Y. Zhai, Y. Dou, D. Zhao, P. F. Fulvio, R. T. Mayes, S. Dai, *Adv. Mater.* **2011**, *23*, 4828.

[115] Q. Lu, J. G. Chen, J. Q. Xiao, *Angew. Chem. Int. Ed.* **2013**, *52*, 1882.

[116] X.-L. Wu, A.-W. Xu, *J. Mater. Chem. A* **2014**, *2*, 4852.

[117] Y. Zhu, S. Murali, M. D. Stoller, K. J. Ganesh, W. Cai, P. J. Ferreira, A. Pirkle, R. M.

Wallace, K. A. Cychosz, M. Thommes, D. Su, E. A. Stach, R. S. Ruoff, *Science* **2011**, *332*, 1537.

[118] A. Burke, *Electrochim. Acta* **2007**, *53*, 1083.

[119] A. Kraytsberg, Y. Ein-Eli, *Energy Fuels* **2014**, *28*, 7303.

[120] S. J. Peighambardoust, S. Rowshanzamir, M. Amjadi, *Int. J. Hydrogen Energy* **2010**, *35*, 9349.

[121] L. Petricca, P. Ohlckers, C. Grinde, *International Journal of Aerospace Engineering* **2011**, *2011*.

[122] S. Mukerjee, S. Srinivasan, *J. Electroanal. Chem.* **1993**, *357*, 201.

[123] S. Sun, G. Zhang, D. Geng, Y. Chen, R. Li, M. Cai, X. Sun, *Angew. Chem. Int. Ed.* **2011**, *50*, 422.

[124] P. Divya, S. Ramaprabhu, *J. Mater. Chem. A* **2014**, *2*, 4912.

[125] R. Bashyam, P. Zelenay, *Nature* **2006**, *443*, 63.

[126] S. Zhang, X.-Z. Yuan, J. N. C. Hin, H. Wang, K. A. Friedrich, M. Schulze, *J. Power Sources* **2009**, *194*, 588.

[127] R. Liu, D. Wu, X. Feng, K. Müllen, *Angew. Chem. Int. Ed.* **2010**, *49*, 2565.

[128] F. Jaouen, E. Proietti, M. Lefevre, R. Chenitz, J.-P. Dodelet, G. Wu, H. T. Chung, C. M. Johnston, P. Zelenay, *Energy Environ. Sci.* **2011**, *4*, 114.

[129] E. Biddinger, D. von Deak, U. Ozkan, *Top. Catal.* **2009**, *52*, 1566.

[130] D. Yu, E. Nagelli, F. Du, L. Dai, *J. Phys.Chem. Lett.* **2010**, *1*, 2165.

[131] C. Xiong, Z. Wei, B. Hu, S. Chen, L. Li, L. Guo, W. Ding, X. Liu, W. Ji, X. Wang, *J. Power Sources* **2012**, *215*, 216.

[132] L. Qu, Y. Liu, J.-B. Baek, L. Dai, *ACS Nano* **2010**, *4*, 1321.

[133] P. Chen, L.-K. Wang, G. Wang, M.-R. Gao, J. Ge, W.-J. Yuan, Y.-H. Shen, A.-J. Xie, S.-H. Yu, *Energy Environ. Sci.***2014**, *7*, 4095.

[134] K. Gong, F. Du, Z. Xia, M. Durstock, L. Dai, *Science* **2009**, *323*, 760.

[135] K. Parvez, S. Yang, Y. Hernandez, A. Winter, A. Turchanin, X. Feng, K. Müllen, *ACS Nano* **2012**, *6*, 9541.

Chapter 2

Three-Dimensional Graphene Foam Cross-Linked with Pre-Encapsulated Fe_3O_4 Nanospheres for Enhanced Lithium Storage

Lithium-ion batteries (LiBs) are the dominant energy storage source for rechargeable electronic devices. Much effort has been dedicated to searching for new LiBs electrode materials that exhibit advantages of high capacity and potential scalability, like silicon and transition metal oxides. However, the huge volume change during the lithiation/delithiation processes has severely limited their cycle life and practical application. In this Chapter, we demonstrate a novel self-assembly strategy to construct three-dimensional graphene/Fe_3O_4 foam hybrids (Fe_3O_4@GS/GF) with Fe_3O_4 nanospheres encapsulated by graphene sheets and confined by graphene networks. Such a hierarchical nanostructure provides double protection against the volume change of Fe_3O_4 during electrochemical cycling. The graphene shells buffer the volume expansion of Fe_3O_4, while the interconnected graphene networks act to reinforce the core-shell Fe_3O_4/graphene subunits. As a result, Fe_3O_4@GS/GF delivers a high reversible capacity of 1059 mAh g^{-1} over 150 cycles, and excellent rate capability, thus exhibiting great potential as an anode material for lithium storage.

2.1 Introduction

Rechargeable lithium-ion batteries (LiBs) are key devices for electricity storage and supply. The main challenges in this field are to achieve high capacity, excellent cycling performance and rate capability for both anode and cathode materials to meet the growing power supply requirements for a variety of applications, including portable electronics, electric vehicles, and renewable energy storage.[1,2] Graphite can react with lithium to form the intercalation compound LiC_6, which has been used in commercial LiBs since 1991.[3] However, the graphite anode has a very low gravimetric capacity (372 mAh g^{-1}), which hinders their widespread use for high power/capacity devices. Thus, much efforts have been paid to developing new anode materials, particularly transition metal oxides compounds (e.g. Fe_2O_3, Fe_3O_4 and SnO_2 etc.). Fe_3O_4 is considered as a promising candidate anode material because of its high theoretical capacity (922 mAh g^{-1}), nontoxic nature, and low cost.[4-6] Fe_3O_4-based anode materials, however, suffer from poor cycling performance and low rate capability due to large specific volume changes upon cycling and the intrinsic kinetic limitations of Fe_3O_4.[7-9] To address these issues, various strategies have been developed to improve the structural integrity and electrical conductivity of Fe_3O_4-based materials, such as optimizing particle size [10-12] or morphology,[5,13-15] and fabricating Fe_3O_4/carbon hybrids.[16-19]

The planar and conductive graphene sheets facilitate electron transport and Li^+ diffusion of anchored active materials, and thus enhance their electrochemical performance for lithium storage.[22-27] Graphene-based hybrid materials with an exposed surface of metal oxides, however, generally exhibit capacity degradation due to the severe volume change and pulverization effect of metal oxides during the cycling processes.[28-31] Very recently,

our group demonstrated that wrapping nanoparticles in graphene sheets to form core-shell structures partially alleviated the pulverization induced by the volume changes of metal oxides,[32-34] although the capacity decay remained unavoidable when the electrochemical devices were operated at a high rate and over a large number of cycles. In this Chapter, integration of Fe_3O_4/graphene core-shell subunits within robust graphene foam is investigated to improve the structural integrity and electrochemical performance of Fe_3O_4 anode material. The hierarchical graphene frameworks are constructed via successive electrostatic and hydrothermal self-assembly procedures. The interconnected graphene frameworks not only afford double protection against the volume changes of Fe_3O_4, but also provide multidimensional pathways to facilitate the electron transport within bulk electrode. As the result, as-obtained graphene/Fe_3O_4 foam hybrids (Fe_3O_4@GS/GF) exhibit higher reversible capacity of 1059 mAh g^{-1} over 150 cycles, and enhanced rate capability (363 mAh g^{-1} at 15 C) compared to the core-shell graphene/Fe_3O_4 hybrids (Fe_3O_4@GS).

2.2 Fabrication of Fe_3O_4/graphene foam

The overall synthetic procedure for Fe_3O_4@GS/GF is illustrated in Figure 2.1. Graphene oxide (GO) is synthesized from natural graphite flakes by a modified Hummer's method.[35] Fe_3O_4 nanospheres (NSs) are prepared by alcohol reduction of ferric chloride via a solvothermal process.[36,37] The detailed procedure is described in the Experimental part (7.1). GO-encapsulated Fe_3O_4 NSs (Fe_3O_4@GO) are fabricated by coassembly of positively-charged aminopropyltrimethoxysilane (APS)-modified Fe_3O_4 NSs and negatively-charged GO sheets.[32] The constructed Fe_3O_4@GO with a core-shell structure is dispersed in an aqueous GO suspension (1 mg mL^{-1}) and placed in an autoclave for

hydrothermal treatment. Within this step, GO is hydrothermally reduced to graphene, and the exposed graphene surface of Fe_3O_4@GO coalesce the graphene sheets due to the abundant oxygen-containing groups of GO serving as cross-linking sites.[38] Thereby, 3D hierarchical graphene/Fe_3O_4 hydrogel-embedding Fe_3O_4@GS are constructed. After freeze-drying dehydration and heat treatment at 500°C under argon, 3D Fe_3O_4@GS/GF is obtained (a photograph of the monolith is shown in Figure 2.1).

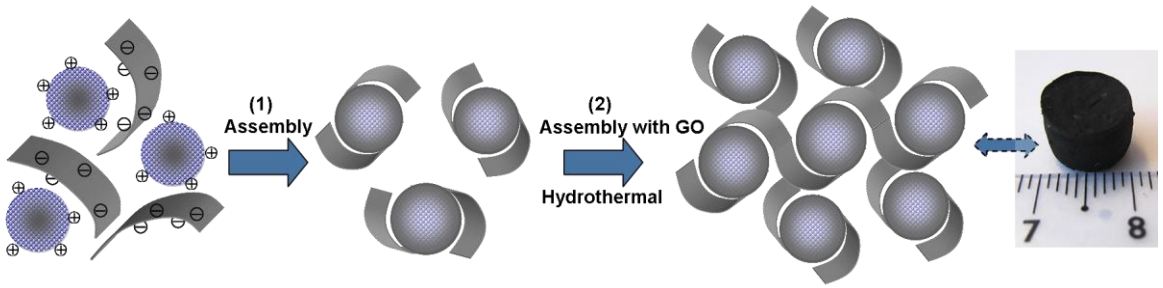

Figure 2.1 Fabrication process and photograph of Fe_3O_4@GS/GF. 1) assembly of positively charged Fe_3O_4 NSs and negatively-charged GO via electrostatic interactions; 2) hydrothermal self-assembly of Fe_3O_4@GO and GO.

2.3 Characterizations of GO and RGO

The morphology of as-synthesized GO was investigated by scanning electron microscopy (SEM) and transmission electron microscopy (TEM) observations. As shown in Figure 2.2a and b, the GO nanosheets are layer structured and irregular, with lateral size larger than 3 μm. Both the SEM and TEM images show a crumpled surface structure of GO sheets, which are formed due to the hydrophobic feature of the underlying silicon or carbon film of copper grids. The wrinkled structure disappeared when GO sheets were deposited

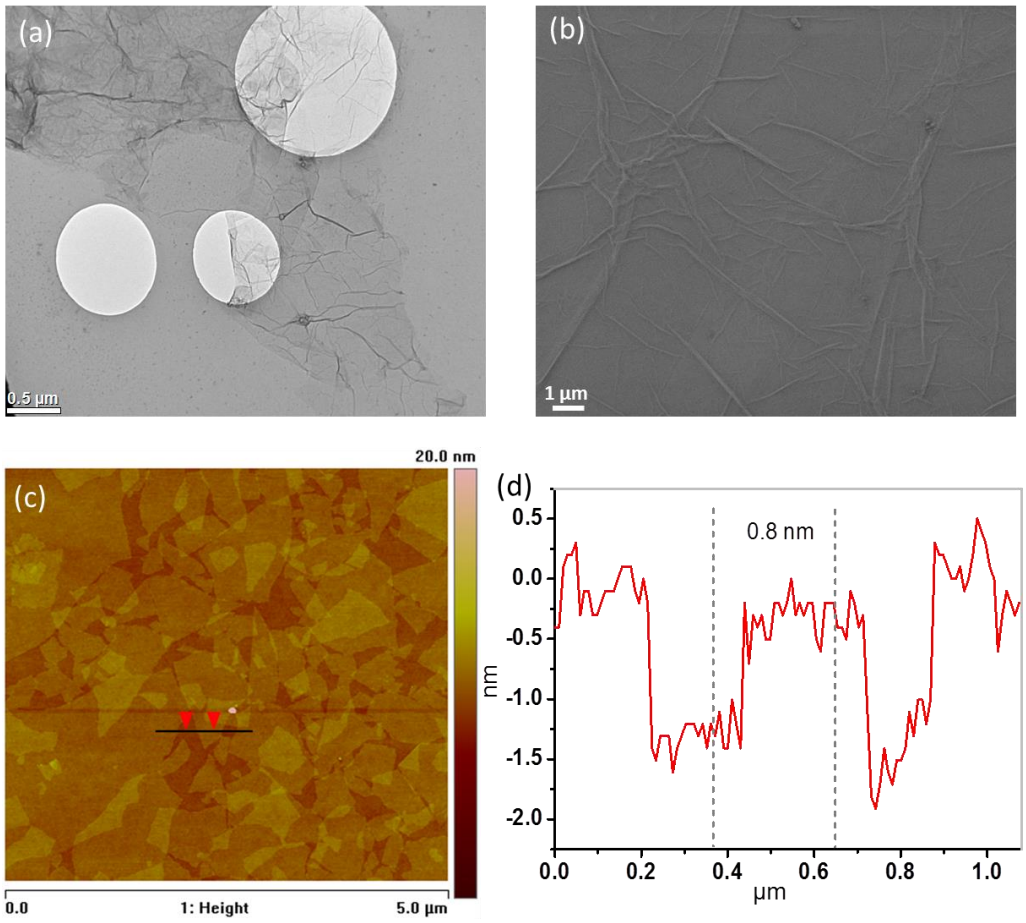

Figure 2.2 TEM (a) and SEM (b) images of GO nanosheets. (c) AFM image of GO on SiO_2/Si substrate. The height profile taken around the black line in image (c) indicates the thickness of ~ 0.8 nm.

on the hydrophilic SiO_2 substrate for atomic force microscopy (AFM) measurement (Figure 2.2c). The height profile (Figure 2.2d) taken around the black line in Figure 2.2c shows that the thickness of GO sheets is about 0.8 nm, which is in good agreement with the value of monolayer GO sheets reported previously.[39]

The chemical structure of GO nanosheets was monitored by FT-IR and UV-via spectrum (Figure 2.3). For comparison, the spectra of chemically reduced GO (RGO) were also presented. The FT-IR spectrum of GO exhibits several characteristic features (Figure

2.3a), including intense bands at 3430 cm^{-1} (OH-stretching vibrations), 1722 cm^{-1} (CO stretching vibrations from carbonyl and carboxylic groups), 1597 cm^{-1} (skeletal vibration from sp^2 graphitic carbon domains), 1383 cm^{-1} (C-OH stretching vibrations), and 1076 cm^{-1} (C-O stretching vibrations).[40] It is noteworthy that the absorptions of RGO sheets at this range almost disappeared, suggesting that the dominant oxygen functionalities within GO sheets were efficiently removed upon hydrazine reduction. This result was confirmed by UV-vis spectra. As shown in Figure 2.3b, the optical absorptions of GO are characterized by the π-π* plasmon peak near 230 nm and the π-π* transitions of C=O at a shoulder peak around 300 nm (marked with dash square). After reduction with hydrazine, the absorption peak of GO dispersion at 230 nm gradually redshifted to 270 nm, indicative of the restoration of π-conjugation within RGO sheets.[41]

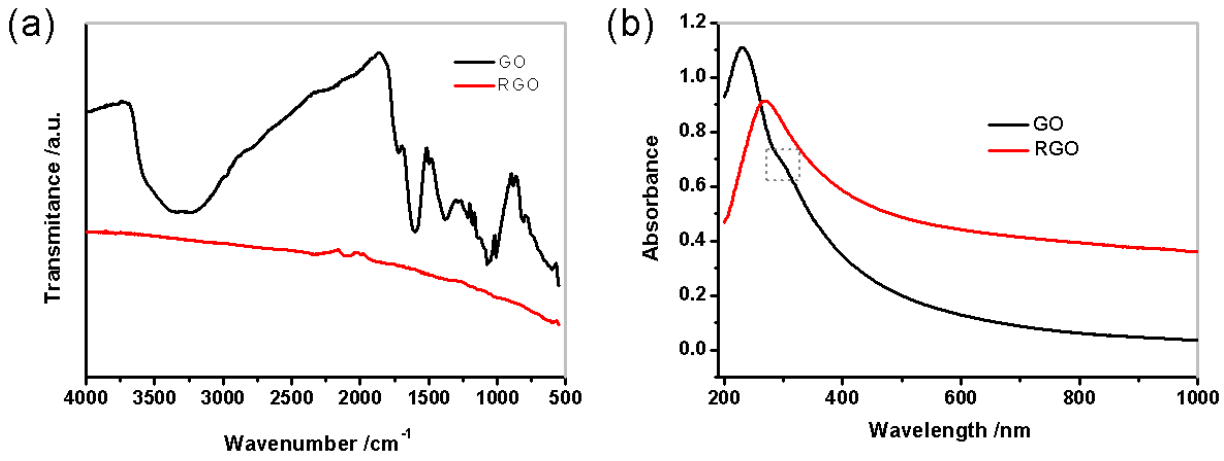

Figure 2.3 Comparison of FT-IR (a) and UV-vis (b) spectra of as-synthesized GO and RGO nanosheets.

2.4 Characterizations of Fe_3O_4@graphene hybrids

The morphology and microstructure of Fe_3O_4 NSs and Fe_3O_4@GO were initially examined based on the SEM measurement. Figure 2.4 demonstrates that the Fe_3O_4 NSs are highly monodispersed, with an average diameter of 200 nm.

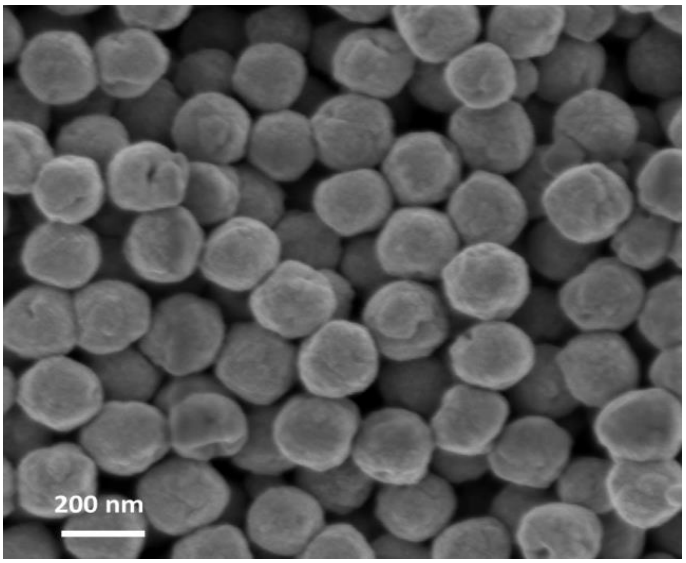

Figure 2.4 Typical SEM image of as-synthesized Fe_3O_4 NSs.

After assembly with GO, Fe_3O_4 NSs are homogeneously and tightly encapsulated by GO shells (Figure 2.5a). With respect to Fe_3O_4 NSs, the presence of crumpled and rough textures on the surfaces of Fe_3O_4@GO is associated with the flexible and corrugated nature of GO sheets. Interestingly, the edges of individual as well as overlapping graphene layers can be observed between aggregated Fe_3O_4 NSs, where the GO layers appear to link neighboring spheres together. The X-ray diffraction (XRD) patterns of Fe_3O_4@GS and pristine Fe_3O_4 NSs are then investigated (Figure 2.5b), and all the peaks of Fe_3O_4@GS are assigned to the standard profiles of Fe_3O_4.[18] Thermogravimetric analysis (TGA) of Fe_3O_4@GS (Figure 2.5c) reveals that the weight fraction of Fe_3O_4 in the hybrids is 91.0 %,

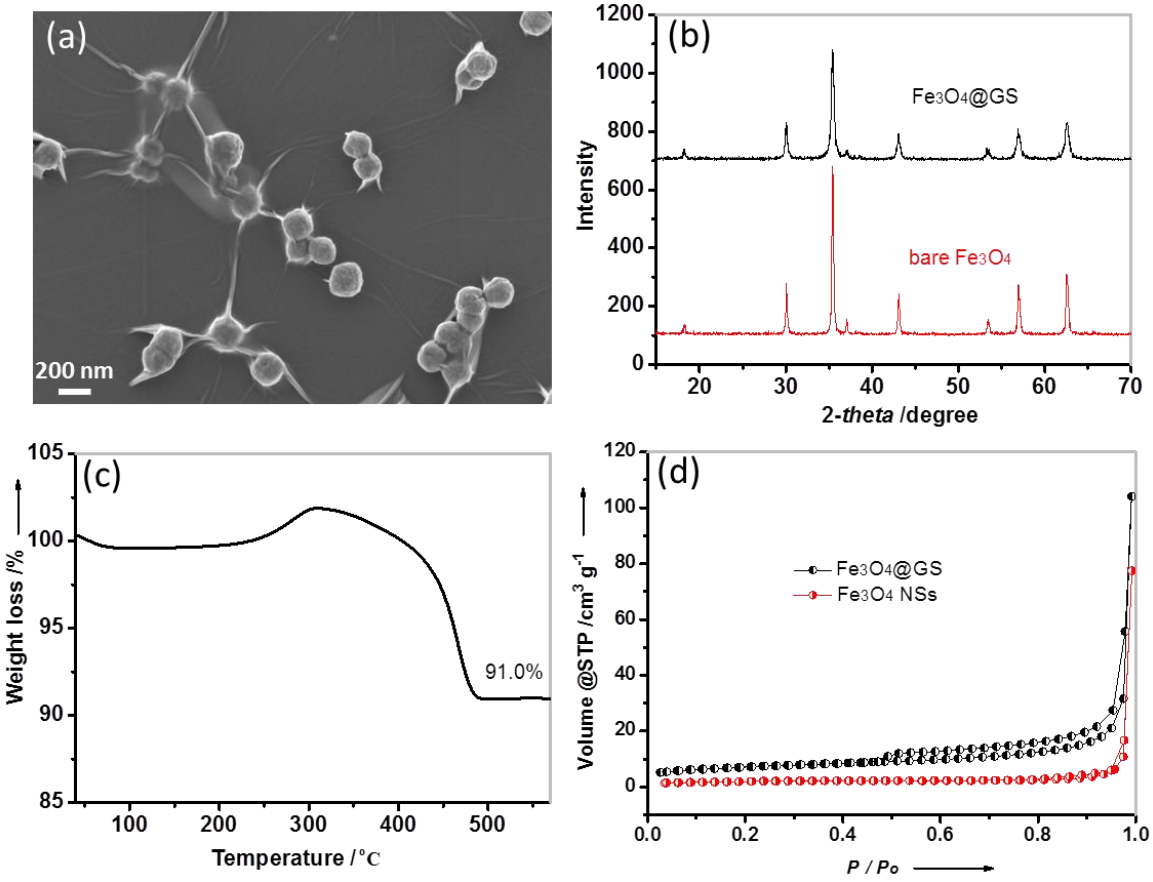

Figure 2.5 (a) Typical SEM image of Fe_3O_4@GO; (b) X-ray diffraction patterns of Fe_3O_4@GS and Fe_3O_4 NSs; (c) TGA curve of Fe_3O_4@GS carried out in air with a heating rate of 10 °C min^{-1}; (d) Nitrogen adsorption and desorption isotherms of Fe_3O_4@GS and Fe_3O_4 NSs.

which is much higher than those reported core-shell Fe_3O_4/carbon hybrids.[33] Such a high content of active material (Fe_3O_4 NSs) in hybrids is beneficial to practical applications. The Brunauer-Emmett-Teller (BET) surface area of Fe_3O_4@GS on the basis of nitrogen adsorption-desorption analysis is calculated to be 8.1 m^2 g^{-1} (Figure 2.5d), which is higher than that of pristine Fe_3O_4 NSs (2.0 m^2 g^{-1}).

2.5 Characterizations of Fe_3O_4/graphene foam

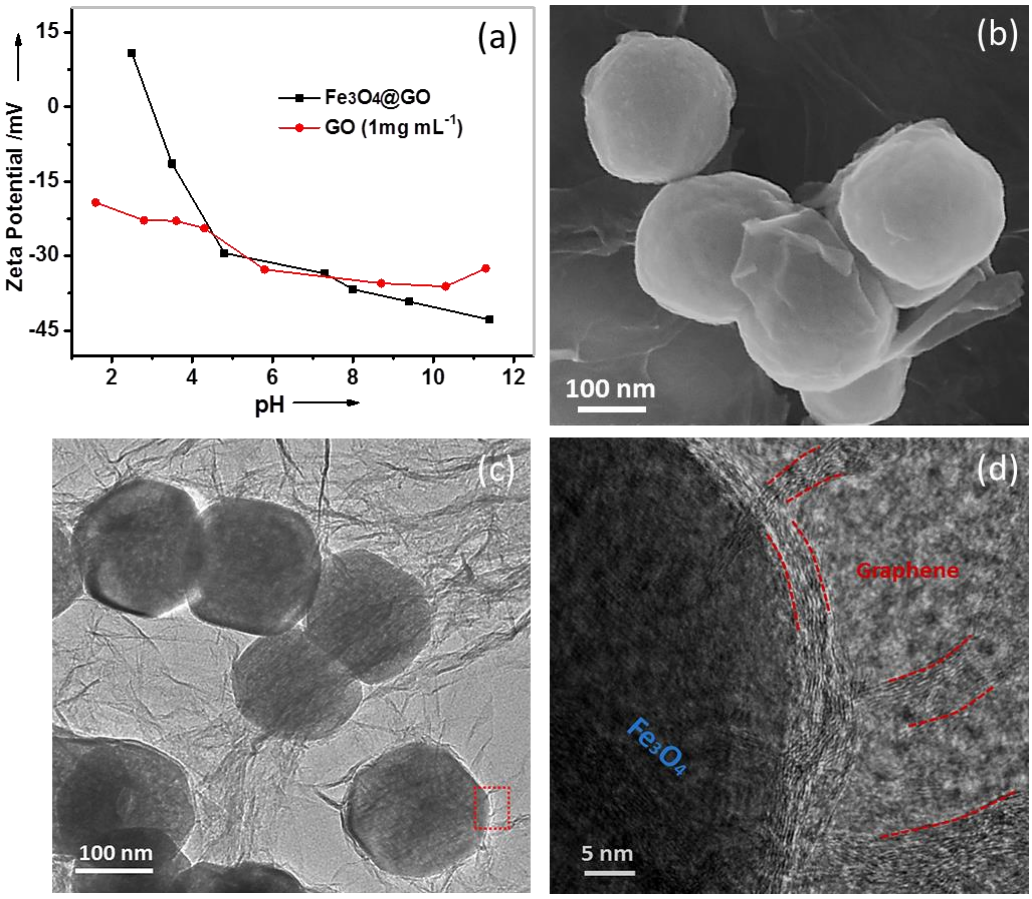

Figure 2.6 (a) Zeta potentials of Fe_3O_4@GO and GO in aqueous dispersion under different pH conditions; (b) Typical SEM images of Fe_3O_4@GS/GF; (c, d) Representative TEM and HR-TEM image of Fe_3O_4@GS/GF. The red rings in (d) indicate that Fe_3O_4 NS is encapsulated in graphene shells and interconnected by graphene networks.

The surface charge of Fe_3O_4@GO was negative over a broad pH range (3.0–11.4, Figure 2.6a), as depicted by the zeta potential measurement. The variation in the zeta potential of Fe_3O_4@GO was in agreement with that of GO over a broad pH range (4.3–10.3). Thus, it can be concluded that the electrostatic repulsion associated with the high hydrophilicity of GO shells ensures the stability of Fe_3O_4@GO dispersions, similar to the

colloidal behavior of GO.[41] The morphology and microstructure of Fe_3O_4@GS/GF were examined based on SEM, TEM, and high-resolution TEM (HR-TEM) measurements. Both SEM and TEM images of Fe_3O_4@GS/GF (Figure 2.6b and c) revealed that Fe_3O_4 NSs were confined in 3D graphene frameworks. The HR-TEM image in Figure 2.6d demonstrated a typical Fe_3O_4 NS with a well-crystalline texture that was tightly enwrapped by graphene sheets (≤5 layers) and interconnected by graphene networks. Such a unique geometric confinement of Fe_3O_4 within a graphene matrix can effectively improve the mechanical strength of an electrode towards lithium storage (see next section).[42-45]

The obtained Fe_3O_4@GS/GF was then characterized by X-ray diffraction (XRD). The diffraction peaks (Figure 2.7a) of the hybrids were perfectly indexed to Fe_3O_4 (JCPDS No.65-3107).[18] A diffraction hump appearing in the range of 24-28° was attributed to the stacking of graphene sheets. Thermogravimetric analysis of Fe_3O_4@GS/GF (Figure 2.7b) revealed that the weight fraction of Fe_3O_4 in the hybrids was 83.7%. To determine the chemical compositions of Fe_3O_4@GS/GF, X-ray photoelectron spectroscopy (XPS)

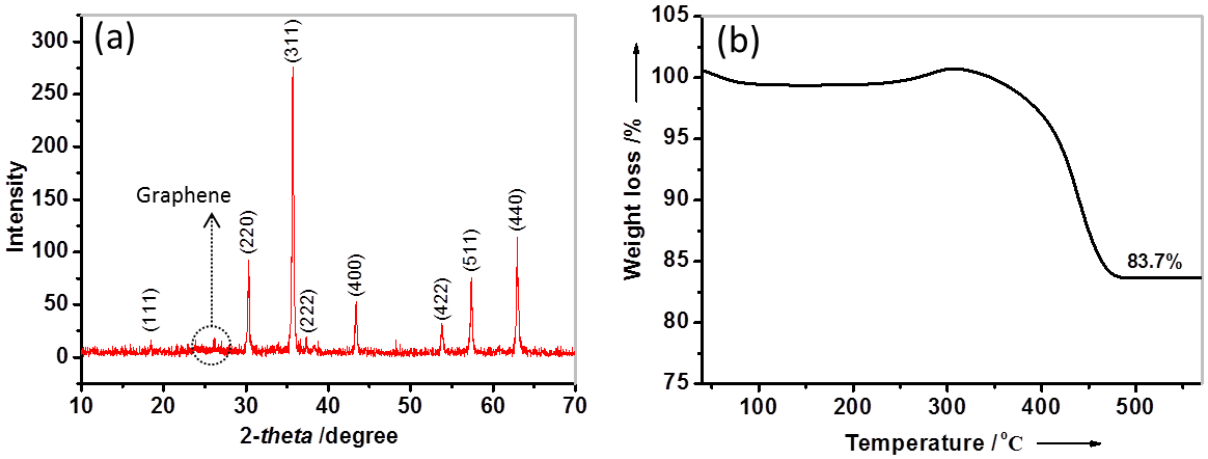

Figure 2.7 X-ray diffraction pattern (a) and TGA curve of Fe_3O_4@GS/GF (b). TGA was carried out in air with a heating rate of 10 °C min^{-1}.

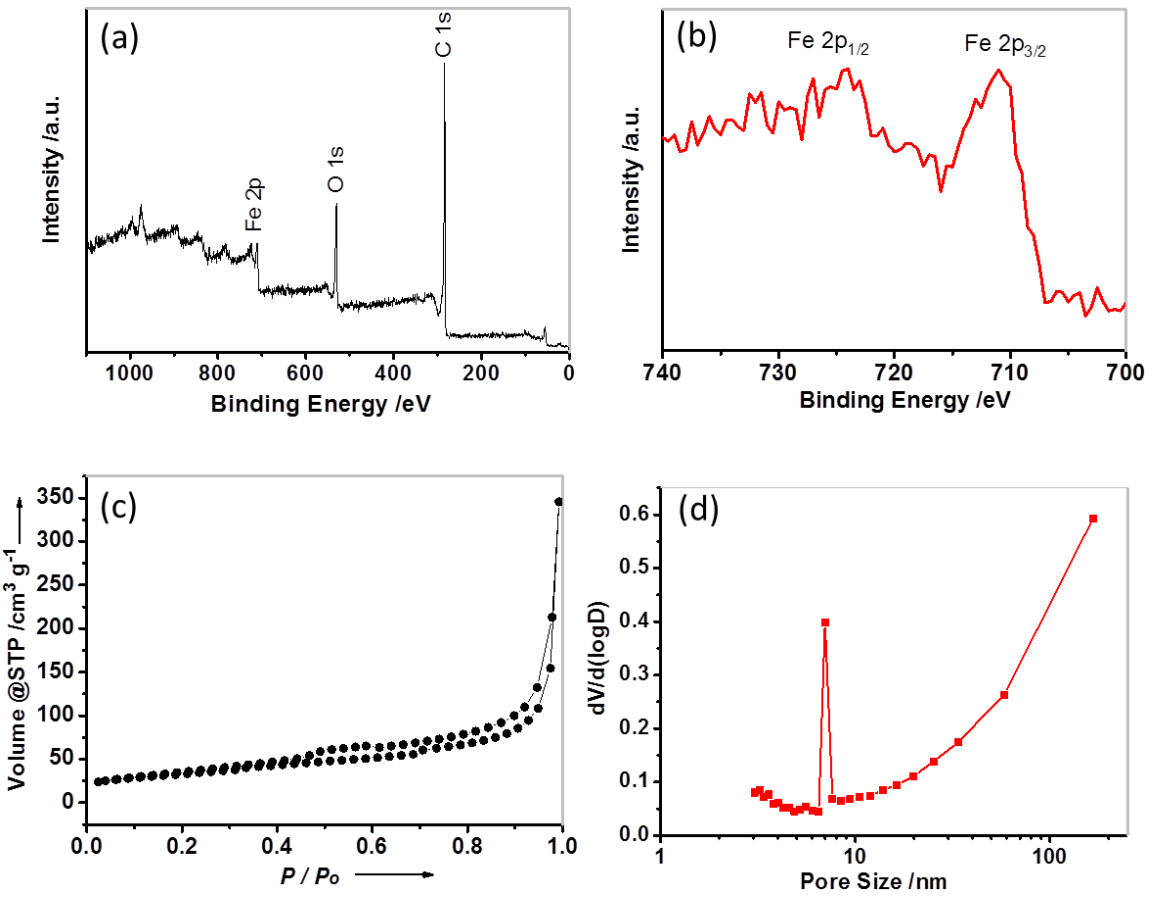

Figure 2.8 (a) X-ray photoelectron spectroscopy spectra and (b) high-resolution Fe2p spectrum of Fe_3O_4@GS/GF; (c) Nitrogen adsorption and desorption isotherm and (d) pore-size distributions of Fe_3O_4@GS/GF.

measurements were performed in a binding energy (BE) from 0 to 1100 eV (Figure 2.8a). The spectrum indicated the presence of carbon, oxygen, and iron, arising from Fe_3O_4 NSs and graphene frameworks. The high-resolution Fe2p spectrum was present in Figure 2.8b. Two peaks at 725 eV and 711 eV corresponded to Fe 2p1/2 and Fe 2p3/2 of Fe_3O_4 NSs, respectively.[46] The 3D porous structure of Fe_3O_4@GS/GF was probed by nitrogen isothermal adsorption/desorption measurement. Remarkably, the Brunauer–Emmett–Teller (BET) specific surface area of Fe_3O_4@GS/GF was calculated to be 115 m^2 g^{-1} (Figure 2.8c), which is much higher than that of Fe_3O_4@GS (8.1 m^2 g^{-1}) and Fe_3O_4 NSs (2.0 m^2 g^{-1}).

Based on the Barrett–Joyner–Halenda (BJH) model, the pores of Fe_3O_4@GS/GF ranged mostly between 6 and 100 nm. Interestingly, a well-defined 7.0 nm mesopore was obtained (Figure 2.8d). With respect to Fe_3O_4@GS and Fe_3O_4 NSs, the high surface area of Fe_3O_4@GS/GF in association with its meso- and macro-porous features, are favorable for electrolyte accessibility and rapid lithium ion diffusion.

2.6 Electrochemical performance for lithium storage

2.6.1 Cycle stability

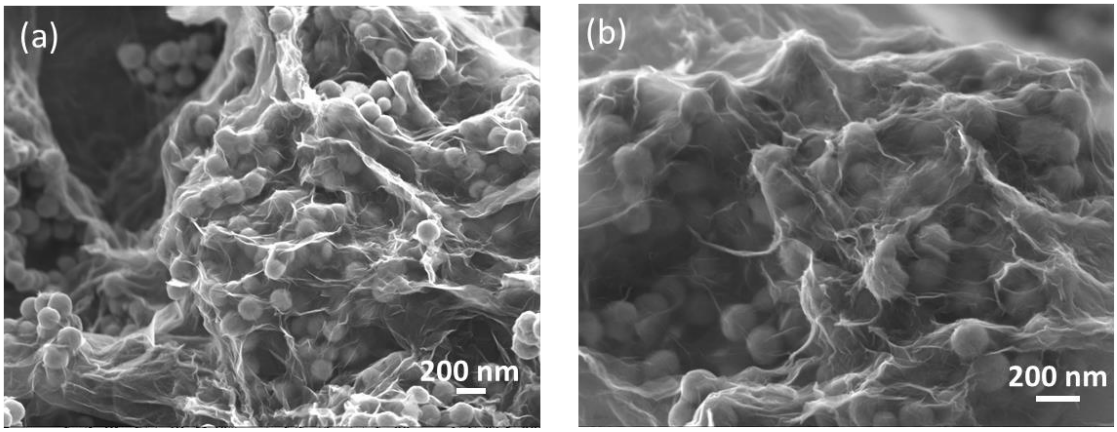

Figure 2.9 Microstructure investigation of Fe_3O_4@GS/GF hybrids before (a) and after grinding (b) for electrode preparation based on SEM measurement.

The details of the electrode preparation and cell assembly are described in the Experimental part. From a practical point of view, the volumetric lithium storage capacity of Fe_3O_4@GS/GF could be improved by a simple mechanical grinding method. As a result, the foam-like Fe_3O_4@GS/GF monolith was broken into pieces for electrode preparation as measured for traditional powder samples. The SEM image of Fe_3O_4@GS/GF after

mechanical grinding (Figure 2.9b) revealed that the Fe_3O_4 NSs remained well-confined within the graphene buffer matrix, consistent with the morphology of pristine Fe_3O_4@GS/GF (Figure 2.9a).

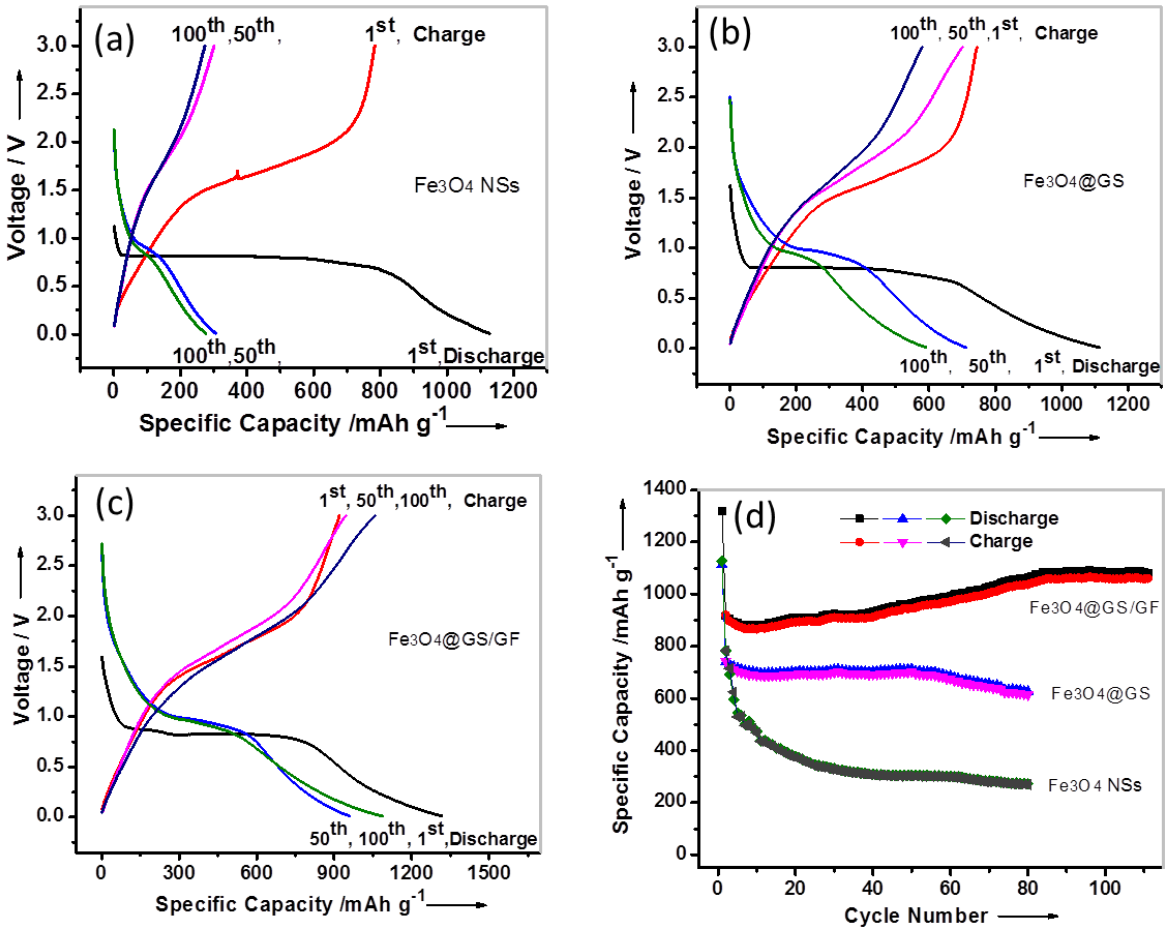

Figure 2.10 Galvanostatic discharge-charge profiles of Fe_3O_4 NSs (a), Fe_3O_4@GS (b), and Fe_3O_4@GS/GF (c) at a current density of 93 mA g^{-1}; (d) Cycling performance of the three samples at a current density of 93 mA g^{-1}.

The electrochemical performance of Fe_3O_4@GS/GF, Fe_3O_4@GS, and Fe_3O_4 NSs was evaluated by galvanostatic discharge-charge measurements at a current density of 93 mA g^{-1} (Figure 2.10a-c). The initial reversible capacity of Fe_3O_4@GS/GF was 920.3 mAh g^{-1}, significantly higher than that of Fe_3O_4@GS and Fe_3O_4 NSs (744.3 mAh g^{-1} and 783.1 mAh

g^{-1}, respectively). The irreversible capacity losses of the three electrodes were probably associated with the formation of a solid electrolyte interface (SEI) on the surfaces of the Fe_3O_4 NSs and the reaction of oxygen-containing functional groups on the graphene with lithium ions.[7] Notably, the cycling performance of Fe_3O_4@GS/GF was superior to that of Fe_3O_4@GS and Fe_3O_4 NSs (Figure 2.10d). Starting from the second cycle, the reversible capacity of Fe_3O_4@GS/GF gradually increased to 1060 mAh g^{-1} after 85 cycles. Moreover, a high reversible capacity of 1059 mAh g^{-1} for the Fe_3O_4@GS/GF electrode was retained after 150 cycles. In contrast, the capacity of Fe_3O_4@GS was stable during the initial 50 cycles and then gradually decreased to 613.8 mAh g^{-1} after the 80th cycle, while the capacity of Fe_3O_4 NSs rapidly decayed from 770.0 mAh g^{-1} to 269.3 mAh g^{-1}. The increasing trend of the capacity of Fe_3O_4@GS/GF in the initial 85 cycles was likely due to the reversible growth of the polymeric gel-like film by the kinetically activated electrolyte degradation, which had been also observed in other metal oxide composites.[18, 47, 48]

2.6.2 Rate capability

To further probe the electrochemical performance of Fe_3O_4@GS/GF and Fe_3O_4@GS, we investigated the rate capability of the samples (Figure 2.11a). As expected, Fe_3O_4@GS/GF manifested an exceptionally high rate capability compared to Fe_3O_4@GS. For example, at a current density of 4800 mA g^{-1} (equal to a current rate of 15 C, by which the discharge and charge process finished in ~4 min), Fe_3O_4@GS/GF still delivered a favorable capacity of 363 mAh g^{-1}, while Fe_3O_4@GS only exhibited a capacity of 115 mAh g^{-1}. When the current rate was returned to 150 mA g^{-1}, a stable high capacity of Fe_3O_4@GS/GF (802 mAh g^{-1}, 93.6% of the initial reversible capacity) was resumed. To

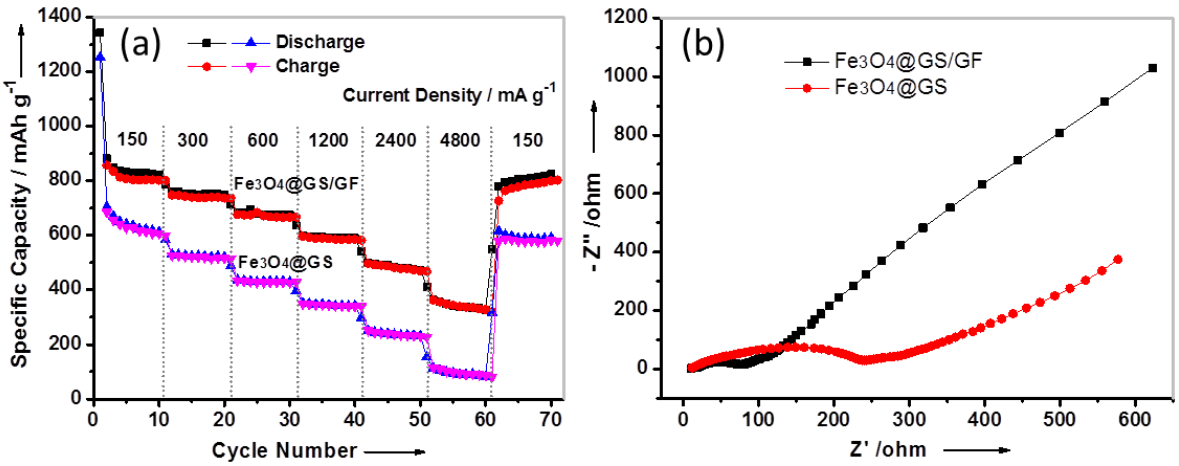

Figure 2.11 (a) Cycling performance of Fe_3O_4@GS/GF and Fe_3O_4@GS at various current densities; (b) Nyquist plots of Fe_3O_4@GS/GF and Fe_3O_4@GS electrodes.

verify the superior electrochemical performance of Fe_3O_4@GS/GF to Fe_3O_4@GS electrodes, AC impedance measurements were performed after the rate capability test. The Nyquist plots (Figure 2.11b) show that the diameter of the semicircle for Fe_3O_4@GS/GF electrodes in the high-medium frequency region is much smaller than that of Fe_3O_4@GS, indicating lower contact and charge-transfer impedances of Fe_3O_4@GS/GF compared with Fe_3O_4@GS.

2.6.3 Effect of Fe_3O_4 loading amount

Further, the relationship between loading amount of active material (Fe_3O_4 NSs) and the electrochemical performance of hybrids was investigated. The Fe_3O_4 loading of Fe_3O_4@GS/GF could be tuned by adjusting the concentration of starting Fe_3O_4 NSs dispersions (e.g. 0.19, 0.38, 0.57 mg mL^{-1}). The cycling performance (Figure 2.12) demonstrated that in each case, stable reversible capacity of Fe_3O_4@GS/GF hybrids over 50

cycles was readily obtained, indicating an effective role of graphene in accommodating volume change of Fe_3O_4. Upon increasing Fe_3O_4 content, the initial Coulombic efficiency of Fe_3O_4@GS/GF increased (from 70.5 to 78.7%), which could be attributed to the reduced lithium consumption of graphene for SEI formation. Generally, a high Fe_3O_4 loading amount resulted in the degradation of reversible capacity, indicating a low utilization of Fe_3O_4 NSs in Fe_3O_4@GS/GF. This result suggests that the graphene frameworks can improve the utilization of Fe_3O_4 in hybrids apart from retaining its structural integrity.

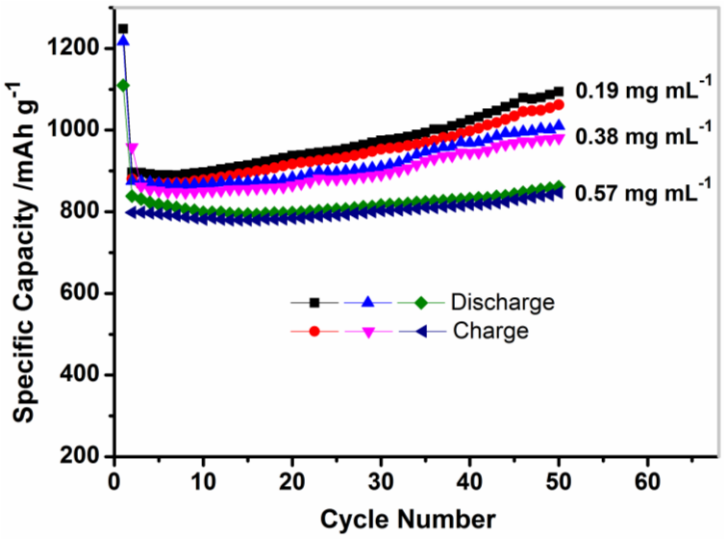

Figure 2.12 Cycling performance of Fe_3O_4@GS/GF hybrids with different Fe_3O_4 NSs loading amount at a current density of 90 mA g^{-1} (the concentration of starting Fe_3O_4 NSs is denoted in the curves).

2.7 Investigation on electrode stability

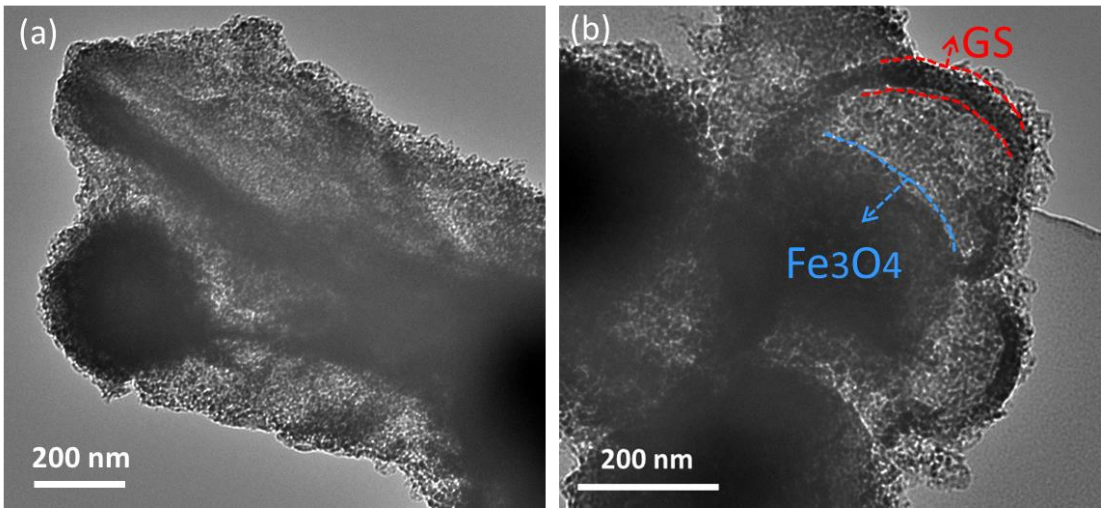

Figure 2.13 TEM images of Fe_3O_4@GS/GF (a) Fe_3O_4@GS (b) electrodes after 80 electrochemical cycles. The nanoparticles decorated on the samples are Super P carbon black; the rings in image (b) indicate the detachment between graphene shell (GS, red color) and Fe_3O_4 NSs (blue color) of Fe_3O_4@GS.

The different structural features among these Fe_3O_4 hybrids play an important role in cycling stability and rate capability, which was validated by TEM observation (Figure 2.13) of Fe_3O_4@GS/GF and Fe_3O_4@GS after the 80th cycle. The cells were discharged to 3V and opened in a glovebox. Both electrodes were washed in dimethyl carbonate (DMC) and 1-methyl-2-pyrrolidinone (NMP) to remove the electrolyte and polyvinyl difluoride (PVDF) binder. Remarkably, the original morphology of the Fe_3O_4@GS/GF electrode was preserved benefiting from the integration of graphene shells and 3D graphene networks, whereas the Fe_3O_4@GS electrode showed a disconnection between Fe_3O_4 NSs and the graphene shells (Figure 2.13). Thereby, it can be concluded that although graphene shells of Fe_3O_4@GS mitigated the structural changes of Fe_3O_4 NSs, such a buffering or

encapsulation function would be weakened or even abolished upon long time cycling as a result of severe volume change and stresses within the electrode. In contrast, these pulverization effects of Fe_3O_4 in Fe_3O_4@GS/GF were suppressed by the synergistic effect of the graphene shells and graphene frameworks, thus realizing a unique double protection of Fe_3O_4 NSs.

2.8 Conclusion

In this chapter, we demonstrate an effective approach for construction of three-dimensional (3D) graphene/Fe_3O_4 hybrids (Fe_3O_4@GS/GF) as anode material for lithium storage. The Fe_3O_4@GS/GF exhibits enhanced cycle and rate performance compared to the core-shell Fe_3O_4@GS hybrids and pristine Fe_3O_4, which can be attributed to our rationally designed 3D porous architecture, combined with an additional geometry confinement effect. First, the graphene shells afford good encapsulation of Fe_3O_4 NSs and accommodate the volume change of Fe_3O_4 NSs during electrochemical cycling. Second, the outer highly elastic and stable graphene networks act as buffer that improves the mechanical reinforcement of the electrode by supporting graphene shells, thereby realizing good cycling performance. Third, the interconnected graphene frameworks with meso-/macro-porous features and a high surface area provide efficient electrical and ionic transfer pathways, which contribute to the much improved reversible capacity and rate capability. The unique architecture provides double protection against the aggregation and volume changes of Fe_3O_4 active materials, and ensures favorable transport kinetics for both electrons and lithium ions. As a consequence, superior cycling performance (1059 mAh g^{-1} over 150 cycles) and excellent rate capability (363 $mAhg^{-1}$ at 4800 mA g^{-1}) were achieved when Fe_3O_4@GS/GF was used as anode material for lithium storage. Such a protocol to construct 3D hierarchical graphene frameworks can be further extended to other metals or metal oxides for electrochemical energy storage and conversion applications.

2.9 References

[1] M. Armand, J. M. Tarascon, *Nature* **2008**, *451*, 652.

[2] J. B. Goodenough, Y. Kim, *Chem. Mater.* **2010**, *22*, 587.

[3] K. Brandt, *Solid State Ionics* **1994**, *69*, 173.

[4] N. Kang, J. H. Park, J. Choi, J. Jin, J. Chun, I. G. Jung, J. Jeong, J. G. Park, S. M. Lee, H. J. Kim, S. U. Son, *Angew. Chem. Int. Ed.* **2012**, *51*, 6626.

[5] W. M. Zhang, X. L. Wu, J. S. Hu, Y. G. Guo, L. J. Wan, *Adv. Funct. Mater.* **2008**, *18*, 3941.

[6] Y. M. Sun, X. L. Hu, W. Luo, Y. H. Huang, *ACS Nano* **2011**, *5*, 7100.

[7] P. Poizot, S. Lauruelle, S. Grugeon, L. Dupont, J. M. Tarascon, *Nature* **2000**, *407*, 496.

[8] P. L. Taberna, S. Mitra, P. Poizot, P. Simon, J. M. Tarascon, *Nat. Mater.* **2006**, *5*, 567.

[9] L. W. Ji, Z. K. Tan, T. R. Kuykendall, S. Aloni, S. D. Xun, E. Lin, V. Battaglia, Y. G Zhang, *Phys. Chem. Chem. Phys.* **2011**, *13*, 7170.

[10] S. L. Zhu, A. C. Marschilok, E. S. Takeuchi, G. T. Yee, G. B. Wang, K. J. Takeuchia, *J. Electrochem. Soc.* **2010**, *157*, A1158.

[11] S. Komaba, T. Mikumo, N. Yabuuchi, A. Ogata, H. Yoshida, Y. Yamada, *J. Electrochem. Soc.* **2010**, *157*, A60.

[12] S. K. Behera, *Chem. Commun.* **2011**, *47*, 10371.

[13] Y. J. Chen, G. Xiao, T. S. Wang, Q. Y. Ouyang, L. H. Qi, Y. Ma, P. Gao, C. L. Zhu, M. S. Cao, H. B. Jin, *J. Phys. Chem. C* **2011**, *115*, 13603.

[14] B. Koo, H. Xiong, M. D. Slater, V. B. Prakapenka, M. Balasubramanian, P. Podsiadlo, C. S. Johnson, T. Rajh, E. V. Shevchenko, *Nano Lett.* **2012**, *12*, 2429.

[15] J. P. Liu, Y. Y. Li, H. J. Fan, Z. H. Zhu, J. Jiang, R. M. Ding, Y. Y. Hu, X. T. Huang, *Chem. Mater.* **2010**, *22*, 212.

[16] C. M. Ban, Z. C. Wu, D. T. Gillaspie, L. Chen, Y. F. Yan, J. L. Blackburn, A. C. Dillon, *Adv. Mater.* **2010**, *22*, E145.

[17] Y. Ma, C. Zhang, G. Ji, J. Y. Lee, *J. Mater. Chem.* **2012**, *22*, 7845.

[18] G. M. Zhou, D. W. Wang, F. Li, L. L. Zhang, N. Li, Z. S. Wu, L. Wen, G. Q. Lu, H. M. Cheng, *Chem. Mater.* **2010**, *22*, 5306.

[19] J. Su, M. H. Cao, L. Ren, C. W. Hu, *J. Phys. Chem. C* **2011**, *115*, 14469.

[20] A. K. Geim, K. S. Novoselov, *Nat. Mater.* **2007**, *6*, 183.

[21] D. Q. Wu, F. Zhang, H. W. Liang, X. L. Feng, *Chem. Soc. Rev.* **2012**, *41*, 6160.

[22] S. B. Yang, G. L. Cui, S. P. Pang, Q. Cao, U. Kolb, X. L. Feng, J. Maier, K. Müllen, *ChemSusChem* **2010**, *3*, 236.

[23] D. H. Wang, D. Choi, J. Li, Z. G. Yang, Z. M. Nie, R. Kou, D. H. Hu, C. M. Wang, L. V. Saraf, J. G. Zhang, I. A. Aksay, J. Liu, *ACS Nano* **2009**, *3*, 907.

[24] S. M. Paek, E. J. Yoo, I. Honma, *Nano Lett.* **2009**, *9*, 72.

[25] Z. S. Wu, W. C. Ren, L. Wen, L. B. Gao, J. P. Zhao, Z. P. Chen, G. M. Zhou, F. Li, H. M. Cheng, *ACS Nano* **2010**, *4*, 3187.

[26] D. J. Xue, S. Xin, Y. Yan, K. C. Jiang, Y. X. Yin, Y. G. Guo, L. J. Wan, *J. Am. Chem. Soc.* **2012**, *134*, 2512.

[27] S. B. Yang, X. L. Feng, K. Müllen, *Adv. Mater.* **2011**, *23*, 3575.

[28] H. L. Wang, L. F. Cui, Y. Yang, H. S. Casalongue, J. T. Robinson, Y. Y. Liang, Y. Cui, H. J. Dai, *J. Am. Chem. Soc.* **2010**, *132*,13978.

[29] B. J. Li, H. Q. Cao, J. Shao, H. Zheng, Y. X. Lu, J. F. Yin, M. Z. Qu, *Chem. Commun.* **2011**, *47*, 3159.

[30] B. J. Li, H. Q. Cao, J. Shao, M. Z. Qu, J. H. Warner, *J. Mater. Chem.* **2011**, *21*, 5069.

[31] M. Zhang, D. N. Lei, X. M. Yin, L. B. Chen, Q. H. Li, Y. G. Wang, T. H. Wang, *J. Mater. Chem.* **2010**, *20*, 5538.

[32] S. B. Yang, X. L. Feng, S. Ivanovici, K. Müllen, *Angew. Chem. Int. Ed.* **2010**, *49*, 8408.

[33] D. Y. Chen, G. Ji, Y. Ma, J. Y. Lee, J. M. Lu, *ACS Appl. Mater. Interfaces* **2011**, *3*, 3078.

[34] W. W. Zhou, J. X. Zhu, C. W. Cheng, J. P. Liu, H. P. Yang, C. X. Cong, C. Guan, X. T. Jia, H. J. Fan, Q. Y. Yan, C. M. Li, T. Yu, *Energy Environ. Sci.* **2011**, *4*, 4954.

[35] W. S. Hummers, R. E. Offeman, *J. Am. Chem. Soc.* **1958**, *80*, 1339.

[36] H. Deng, X. L. Li, Q. Peng, X. Wang, J. P. Chen, Y. D. Li, *Angew. Chem. Int. Ed.* **2005**, *44*, 2782.

[37] J. F. Zhou, L. J. Meng, X. L. Feng, X. K. Zhang, Q. H. Lu, *Angew. Chem. Int. Ed.* **2010**, *49*, 8476.

[38] Y. X. Xu, K. X. Sheng, C. Li, G. Q. Shi, *ACS Nano* **2010**, *4*, 4324.

[39] S. Stankovich, D. A. Dikin, R. D. Piner, K. A. Kohlhaas, A. Kleinhammes, Y. Jia, Y. Wu, S. T. Nguyen, R. S. Ruoff, *Carbon* **2007**, *45*, 1558.

[40] A. B. Bourlinos, D. Gournis, D. Petridis, T. Szabó, A. Szeri, I. Dékány, *Langmuir* **2003**, *19*, 6050.

[41] D. Li, M. B. Müller, S. Gilje, R. B. Kaner, G. G. Wallace, *Nat. Nanotech.* **2008**, *3*, 101.

[42] G. X. Wang, B. Wang, X. L. Wang, J. Park, S. X. Dou, H. Ahn, K. Kim, *J. Mater. Chem.* **2009**, *19*, 8378.

[43] X. Xin, X. F. Zhou, F. Wang, X. Y. Yao, X. X. Xu, Y. M. Zhu, Z. P. Liu, *J. Mater. Chem.* **2012**, *22*, 7724.

[44] W. Wei, J. L. Wang, L. J. Zhou, J. Yang, B. Schumann, Y. N. NuLi, *Electrochem. Commun.* **2011**, *13*, 399.

[45] Z. S. Wu, S. B. Yang, Y. Sun, K. Parvez, X. L. Feng, K. Müllen, *J. Am. Chem. Soc.* **2012**, *134*, 9082.

[46] W. F. Chen, S. R. Li, C. H. Chen, L. F. Yan, *Adv. Mater.* **2011**, *23*, 5679.

[47] S. Grugeon, S. Laruelle, L. Dupont, J. M. Tarascon, *Solid State Sci.* **2003**, *5*, 895.

[48] J. S. Do, C. H. Weng, *J. Power Sources* **2005**, *146*, 482.

Chapter 3

Graphene-Based Mesoporous Carbon Nanosheets for High-Performance Supercapacitor Electrode

Like lithium ion batteries (LiBs), supercapacitors (SCs) are also among the most popular types of energy storage devices. In the previous chapter, we demonstrated that controlled assembly of a graphene matrix into a hierarchical structure was crucial to strengthen structural integrity and electrochemical performance of the active material (Fe_3O_4) for LiBs. In regard to SCs, the performance of carbonaceous electrode materials is intimately dependent on the accessible specific surface area and pore structure; therefore, optimization of their pore size, pore structure and distribution is required. In this Chapter, we develop a combined self-assembly and nanocasting approach to synthesize highly porous carbon nanosheets (HPCN) with graphene layer sandwiched by continuous mesoporous carbon shells. Mesoporosity regulation over HPCN is found to be effective in promoting the accessible surface area and pore space. The HPCN possesses prominent porous features including highly open and regular mesopores (pore size: ~12 nm), large surface area (1273 $m^2 g^{-1}$) and pore volume (2.64 $cm^3 g^{-1}$). As a result, the electrode made of HPCN exhibits a high specific capacitance (222 F g^{-1} at a scan rate of 1 mV s^{-1}) and good rate capability for electrochemical double-layer capacitors.

3.1 Introduction

Whereas lithium ion batteries (LiBs) have a defined cycle life and take a long time to charge, supercapacitors (SCs) offer an efficient and reliable technology for energy storage and delivery.[1, 2] The potential of graphene as supercapacitor electrode materials has been demonstrated.[3, 4] However, the accessibility of surface area and capacitance performance of the graphene-derived materials (GHMs) are still highly limited, mainly attributable to the strong aggregation tendency of graphene sheets and random distribution of porous components.[5, 6] Recently developed activation and template approaches allow for fabricating GHMs with high surface areas and abundant porosity.[7-10] However, the etching-derived activation process eventually results in substantial structural defects and mass loss, while direct pyrolysis of a mixture of the template (e.g. silica, polystyrene etc.) and carbon precursors frequently fails in controlling the porous structure.[11-13]

In this Chapter, we describe a design and synthesis of highly porous carbon nanosheets (HPCN) with graphene sandwiched by mesoporous carbon shells. The mesopore distribution is regulated by employing a hierarchical graphene/silica template that is built up by in-situ growth of silica layers and electrostatic assembly of colloidal silica nanoparticles on graphene oxide (GO). As-obtained template is then cast with sucrose and subjected to pyrolysis/etching treatment to create size-defined mesopores. Notably, HPCN exhibits a specific surface area of 1273 $m^2 g^{-1}$ and large pore volume of 2.64 $cm^3 g^{-1}$, higher than that of porous carbon nanosheets (PCN, 910 $m^2 g^{-1}$ and 1.15 $cm^3 g^{-1}$ respectively) prepared through physical mixing. Electrochemical double-layer capacitors (EDLCs) manufactured on the basis of HPCN deliver a high specific capacitance of 222 F g^{-1} and an excellent high rate capability of 156 F g^{-1} (at a scan rate of 100 mV s^{-1}). We further

demonstrate that HPCN can serve as a two-dimensional (2D) substrate for incorporation of RuO_2 nanomaterial for high-performance pseudo-capacitor electrode.

3.2 Fabrication of highly porous carbon nanosheets

The overall synthetic procedure of HPCN is illustrated in Figure 3.1, and the detailed procedure is described in the Experimental part (7.2). A mesoporous silica shell is initially grown on GO using cetyltrimethyl ammonium bromide (CTAB)-directed hydrolysis of tetraethylorthosilicate (TEOS), to generate graphene-based silica nanosheets with a mesopore size of 2 nm (G-silica-I).[14] G-silica-I is then functionalized with polydiallyldimethylammonium chloride (PDDA-functionalized G-silica-I), and electrostatically assembled with negatively charged colloidal silica nanoparticles (NPs) in aqueous solution. As a result, G-silica-I is further sandwiched with shells comprising close-packed colloidal silica NPs (denoted as G-silica-II). Afterwards, G-silica-II is employed as template with sucrose as carbon source, to prepare HPCN by a nanocasting technology. Subsequent carbonization and etching of the silica template yield HPCN with size-defined mesopores. Further, RuO_2-embedded HPCN hybrids (RuO_2@HPCN) are synthesized via a sol-gel deposition method.[15] HPCN are dispersed in a solution of $RuCl_3$ (0.1M), and an aqueous solution of $NaHCO_3$ is added to adjust the pH value to 7. After stirring for 6 h, the collected precipitate is washed and annealed at 150°C in air to generate RuO_2@HPCN.

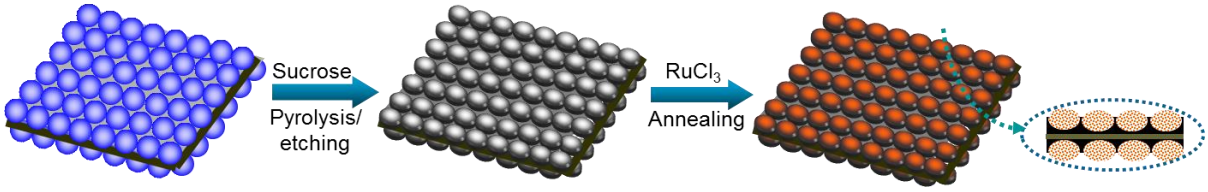

Figure 3.1 Fabrication processes of HPCN and RuO_2@HPCN via a nanocasting and sol-gel method respectively.

3.3 Characterizations of HPCN

To achieve a favorable electrostatic assembly between G-silica-I and colloidal silica NPs, the surface charges of colloidal silica NPs and G-silica-I before and after functionalization with PDDA depending on various pH values were monitored by zeta potential measurements (Figure 3.2a). Typically, the zeta potential of silica NPs and pristine G-silica-I was negative over the entire investigated pH range (1–12). As expected, the surface charge of PDDA-functionalized G-silica-I was positive over the pH range from 1 to 12, in contrast to that of pristine G-silica. Therefore, assembly between PDDA-functionalized G-silica-I and colloidal silica was carried out via electrostatic interactions under neutral conditions, where a broad zeta potential gap between PDDA-functionalized G-silica-I and silica NPs created strong mutual interactions. The transmission electron microscopy (TEM) measurement verified the successful construction of G-silica-II. Interestingly, all silica NPs homogeneously attached onto the G-silica-I surface in a close-packing manner with no individual particles observed from the TEM image (Figure 3.2b). Next, the G-silica-II was used as template to replicate 2D mesoporous nanosheets via nanocasting using sucrose as carbon precursor (Figure 3.2c). Owing to the presence of

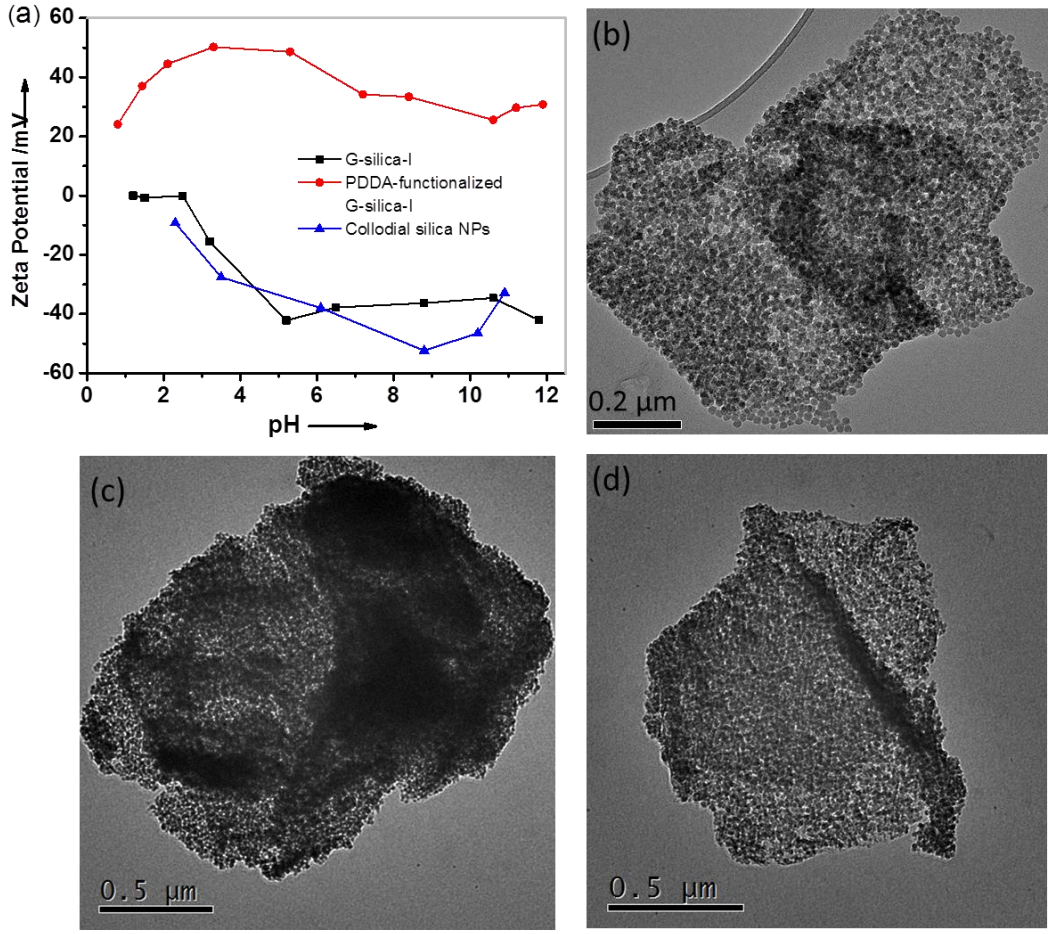

Figure 3.2 (a) Zeta potentials of colloidal silica NPs and G-silica-I before and after PDDA functionalization; (b) Typical TEM image of resulting G-silica-II template, revealing the uniform adhesion of colloidal silica NPs on the surface of G-silica-I; TEM images of sucrose-filled G-silica-II before (c) and after pyrolysis (d).

protecting silica shells, the 2D sandwich-like structure of the sucrose-filled template was well retained during the carbonization treatment (Figure 3.2d).

The morphology and microstructure of HPCN after removal of the silica template were characterized by TEM and scanning electron microscopy (SEM) measurements. As shown in Figure 3.3a and b, HPCN were hundreds of nanometers in lateral size and decorated with uniform mesopores, which obviously originated from the inverse replication

of G-silica-II template. Notably, regular mesopores with defined pore size of ~12 nm were interconnected on the graphene surface, resulting in unique planar carbon shells.

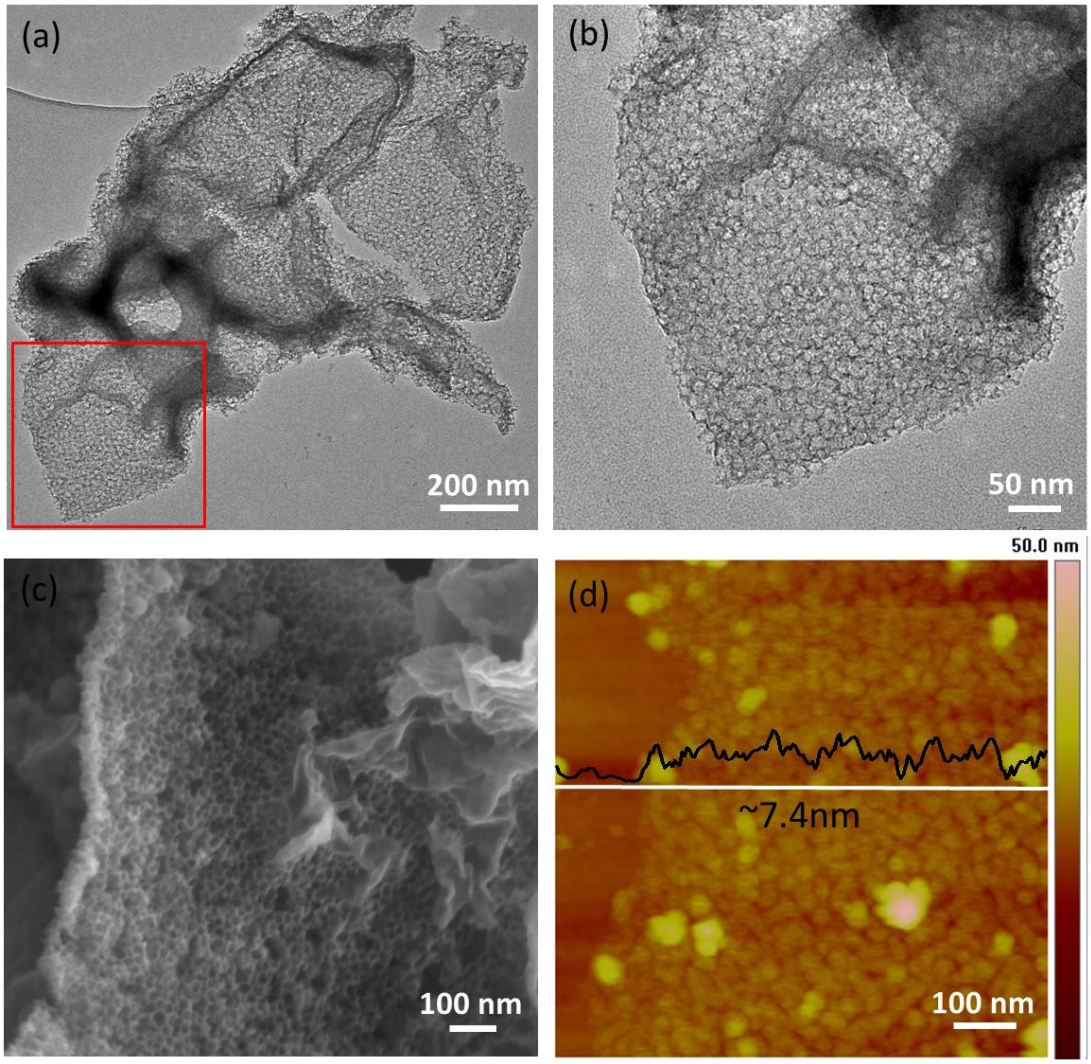

Figure 3.3 (a) Typical TEM images of HPCN nanosheets revealing that interconnected mesopores were uniformly coated on graphene surface; (b) TEM image of magnified square region marked in (a); (c) SEM image of HPCN; (d) Representative AFM image of HPCN, the height analysis indicate a mean thickness of ~7.4 nm across the edge area of HPCN (white line).

The sandwich-like structure of HPCN can also be observed from the SEM image (Figure 3.3c). Apparently, the HPCN exhibit highly open porous morphology with large amounts of mesopores arranged over both sides of graphene sheets. Further, the atomic force microscopy (AFM) image reveals the mesoporous feature of HPCN as observed from TEM and SEM visualizations. The height difference across the edge area of HPCN (white line in Figure 3.3d) shows a mean thickness of ~7.4 nm, implying the existence of ultrathin mesoporous shell. Such unique mesopore textures offer easy access of the electrolyte to HPCN surface, which is favorable for charge diffusion/accommodation and formation of electric double layers for EDLCs applications (see below).

To assess the effect of porosity regulation on physicochemical properties and capacitive performance of 2D carbonaceous hybrids, porous carbon nanosheeets (PCN) and carbon nanosheets (CN) were also prepared for the purpose of comparison. PCN was synthesized by employing physically mixed G-silica-I/silica NPs (physically mixed G-silica-II) as template, while CN was prepared using reduced graphene oxide (RGO) nanosheets as the substrates (without involving silica template). A sucrose solution in ethanol was then cast into physically mixed G-silica-II template and RGO nanosheets respectively. The weight ratio between sucrose and template/substrate was fixed to 2:1. Subsequent pyrolysis of sucrose and etching of the silica template gave birth to PCN and CN respectively. The TEM image of PCN (Figure 3.4a) discloses that the mesoporous carbon is aggregated and randomly intercalated into graphene nanosheets, which may be attributed to the non-uniform distribution of Si NPs within physically mixed G-silica-II template. In the case of CN, highly crumpled carbon nanosheets can be observed, which is possibly induced by the shrinkage of RGO during pyrolysis of sucrose precursor (Figure 3.4b).

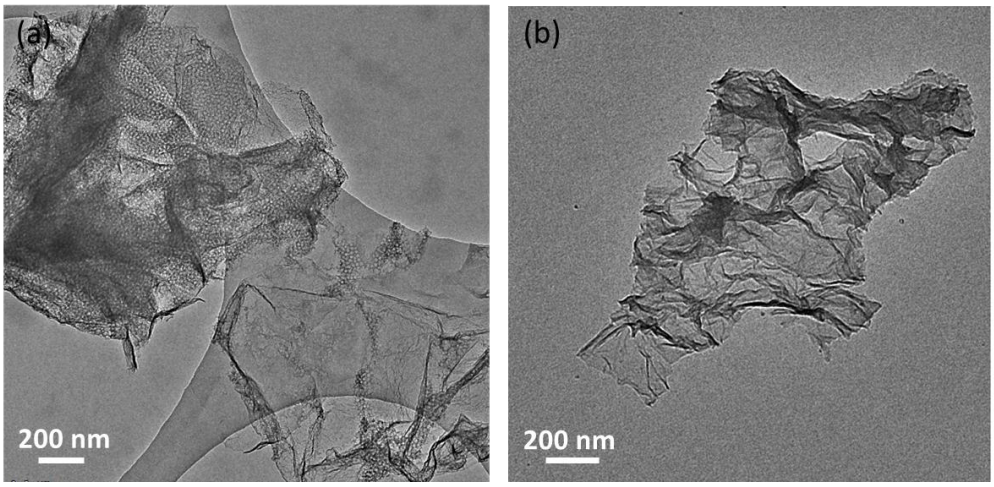

Figure 3.4 TEM images of as-obtained PCN (a) and CN (b) hybrids.

Figure 3.5a shows the X-ray diffraction (XRD) patterns of HPCN. Two diffraction peaks positioned near 24.5^{o} and 43.8^{o} arise from the (002) and (100) crystal planes of graphitic carbon in HPCN. Compared to pristine graphite and RGO nanosheets,[16] the markedly reduced intensity of the (002) peak indicates a much weaker stacking of graphene owing to the protection of mesoporous carbon shells. In the Raman spectrum (Figure 3.5b), the peaks around 1588 cm^{-1} and 2730 cm^{-1} correspond to the G (graphtic carbon) and D (disordered carbon) band, respectively. The intense D peak associated with a high intensity ratio of D to G band (I_D/I_G = 0.99) implies the existence of structurally disordered carbon, as expected for the case of RGO and sucrose-derived amorphous carbon.[17-20] In addition, the 2D band peak, which is characteristic for mono-/multi-layer graphene structures,[21] can hardly be observed. An X-ray photoelectron spectroscopy (XPS) measurement was performed to investigate the chemical compositions of HPCN (Figure 3.5c). The survey spectrum indicates the presence of carbon and oxygen, with an atomic content of 82.3 % and 17.7 %, respectively. The high-resolution C1s spectrum can be further deconvoluted into three signals with binding energies of 284.6, 285.8 and 289.2 eV that correspond to

C=C, C-O and C=O, respectively (Figure 3.5d).[22]

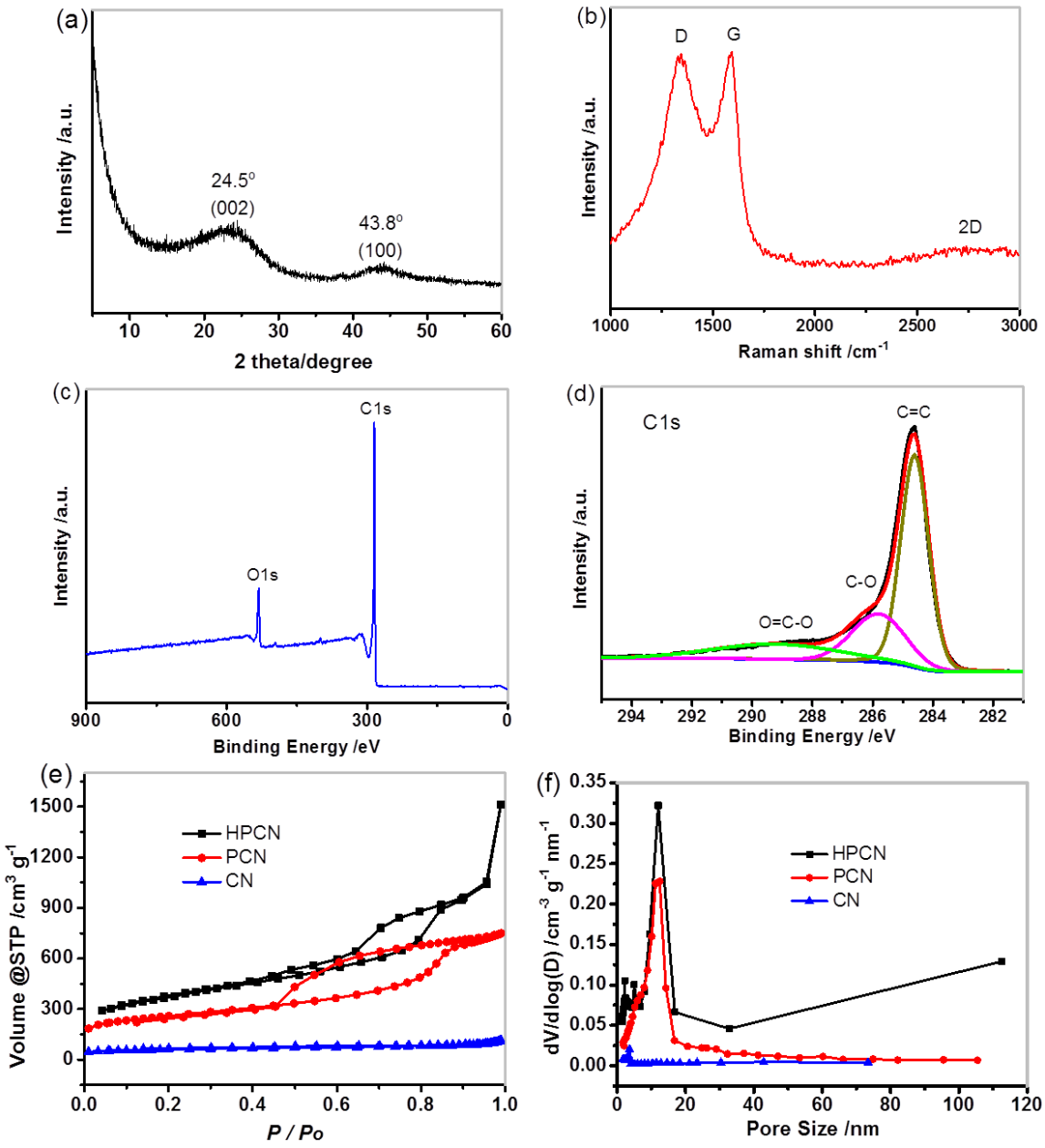

Figure 3.5 X-ray diffraction pattern (a) and Raman spectra (b) of HPCN; X-ray photoelectron spectroscopy (c) and C1s XPS spectrum (d) of HPCN; The deconvoluted spectrum of C1s fit into three energy components centered around 284.6, 285.8 and 289.2 eV, and correspond to C=C, C-O and C=O, respectively; Nitrogen adsorption/desorption isotherms (e) and BJH pore size distributions (f) of HPCN, PCN and CN samples.

The porous features of HPCN, PCN and CN were investigated by nitrogen physisorption measurements (Figure 3.5e). The adsorption-desorption isotherms of HPCN and PCN exhibit a type IV branch with remarkable hysteresis loops, indicating the presence of high density of mesopores.[23] Brunauer-Emmett-Teller (BET) analysis reveals a specific surface area of 1273 $m^2 g^{-1}$ and pore volume of 2.64 $cm^3 g^{-1}$ for HPCN, both of which are much higher than those of PCN (910 $m^2 g^{-1}$ and 1.15 $cm^3 g^{-1}$ respectively). In contrast, CN displays a low surface area of 212 $m^2 g^{-1}$ and pore volume of 0.17 $cm^3 g^{-1}$ respectively. These comparative results indicate that porosity regulation plays a crucial role for the porous characteristics of HPCN. With respect to PCN, the homogeneously distributed and size-defined mesopores contribute to a significant increase of accessible surface area and pore structures of HPCN. Further, the pore size of HPCN and PCN calculated by the Barrett–Joyner–Halenda (BJH) method indicates a narrow mesopore distribution centered at 12 nm (Figure 3.5f), consistent with the diameter of the colloidal silica template. In contrast, no evident mesopores are observed for CN hybrids.

Next, the influence of the carbon loading amount on the physicochemical properties of HPCN was investigated. A series of HPCN-X hybrids were prepared by casting different weight proportions of sucrose onto the G-silica-II template, followed by the same pyrolysis and etching of silica process of HPCN; X presents the weight ratio of sucrose to the G-silica-II template, e.g. 1:1, 2:1 and 4:1. TEM measurements (Figure 3.6a and b) disclose that both HPCN-1 and HPCN-4 possess a similar morphology as observed for HPCN-2 (Figure 3.3a and b), with 2D regular mesopores decorated on graphene nanosheets. The porous feature among HPCN-X samples was probed by nitrogen adsorption/desorption measurements (Figure 3.6c and d). The adsorption/desorption curves of HPCN-X exhibit the prominent type IV isotherms with a distinct hysteresis loop of H2 in the relative

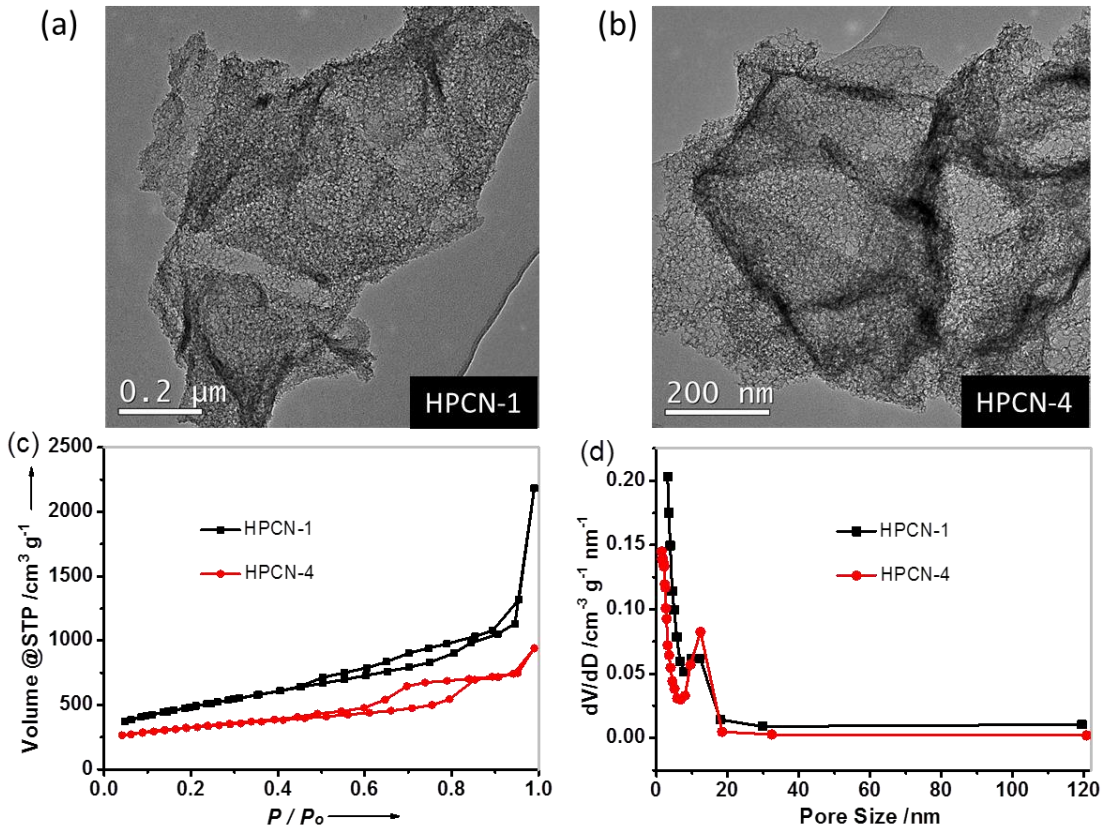

Figure 3.6 TEM image of HPCN-1 (a) and HPCN-4 (b); Nitrogen adsorption/desorption isotherms (c) and BJH pore size distributions (d) of HPCN-1 and HPCN-4.

Table 3.1 Physicochemical properties of HPCN-X hybrids.*

	HPCN-1	HPCN-2	HPCN-4
S_{BET} ($m^2\ g^{-1}$)	1690	1273	1068
V_t ($cm^3\ g^{-1}$)	3.38	2.64	1.45
V_m ($cm^3\ g^{-1}$)	0.09	0.14	0.17
V_m/V_t (%)	2.7	5.3	11.7

*S_{BET} : specific BET surface area;

V_t : total specific pore volume;

V_m : specific pore volume from the micropores.

pressure (P/Po) above 0.5, which is indicative of the presence of large amount of mesopores.[24] The porous characteristics calculated from the adsorption branches are summarized in Table 3.1. Upon increasing the carbon loading, both BET surface area and pore volume of HPCN-X decrease, which are consistence with other porous carbon materials produced via decomposition of hydrocarbon precursors.[25] Under an optimal weight ratio of sucrose/template (1:1), a maximum BET surface area (1690 $m^2 g^{-1}$) and pore volume (3.4 $cm^3 g^{-1}$) are obtained for HPCN-1 hybrids. It is noteworthy that the proportion of a specific volume of the micropores increases upon increasing the carbon loading. This can be attributed to the decomposition of sucrose into a large quantity of amorphous carbon with microporous structure.[26-28] In addition, the pore size analysis based on BJH model discloses the mesoporous feature of HPCN-1/-4 with a narrow pore distribution peak centered at 12 nm, which is in accordance with the pore configurations of HPCN-2 (Figure 3.5f).

3.4 Capacitive performance of HPCN

The prominent features including high surface area, regular and open mesoporous structure make HPCN a promising electrode material for electrochemical double-layer capacitors (EDLCs). We evaluated the electrochemical capacitive performance of HPCN and the reference samples PCN and CN in a three-electrode system, applying 1 M H_2SO_4 as electrolyte and Ag/AgCl as the reference electrode. The cyclic voltammetry (CV) profiles of all samples at a scan rate of 100 mV s^{-1} (Figure 3.7a) exhibit the typical electrical double layer behavior of a carbonaceous electrode.[29-31] It is noteworthy that the current density of HPCN is much higher than that of PCN and CN, demonstrating the enhanced transport

kinetics for both electrons and electrolyte ions. Figure 3.7b presents the CV curves of a HPCN electrode at various scan rates. Remarkably, the CV curve displays a typical rectangular shape between −0.1 and 0.6 V without obvious distortion upon increasing sweeping rates from 10 to 200 mV s^{-1}, which indicate the excellent charge storage capability of HPCN electrodes. The specific capacitances of HPCN, PCN, and CN calculated from their CV curves are plotted in Figure 3.7c. As expected, the HPCN exhibits the highest capacity among all measured samples at the same scan rate. For instance, a specific capacitance of 222 F g^{-1} is achieved at a scanning rate of 1 mV s^{-1}, significantly higher than that of PCN (157 F g^{-1}) and CN (103 F g^{-1}), respectively. Moreover, the HPCN displays good capacitance retention. At a high scan rate of 100 mV s^{-1}, HPCN still delivers a favorable specific capacitance of 156 F g^{-1} (108 and 50 F g^{-1} for PCN and CN respectively). The enhanced capacity may be attributed to the improvement of ion accessibility in HPCN during the cycling process which leads to an increased accommodation behavior for charges. Figure 3.7d presents the galvanostatic charge/discharge profiles of HPCN at different current rate from 2 to 20 A g^{-1}. Apparently, the charge/discharge profiles of HPCN are highly linear and symmetrical without obvious iR drop, indicating a rapid I-V response and an excellent electrochemical reversibility.[32]

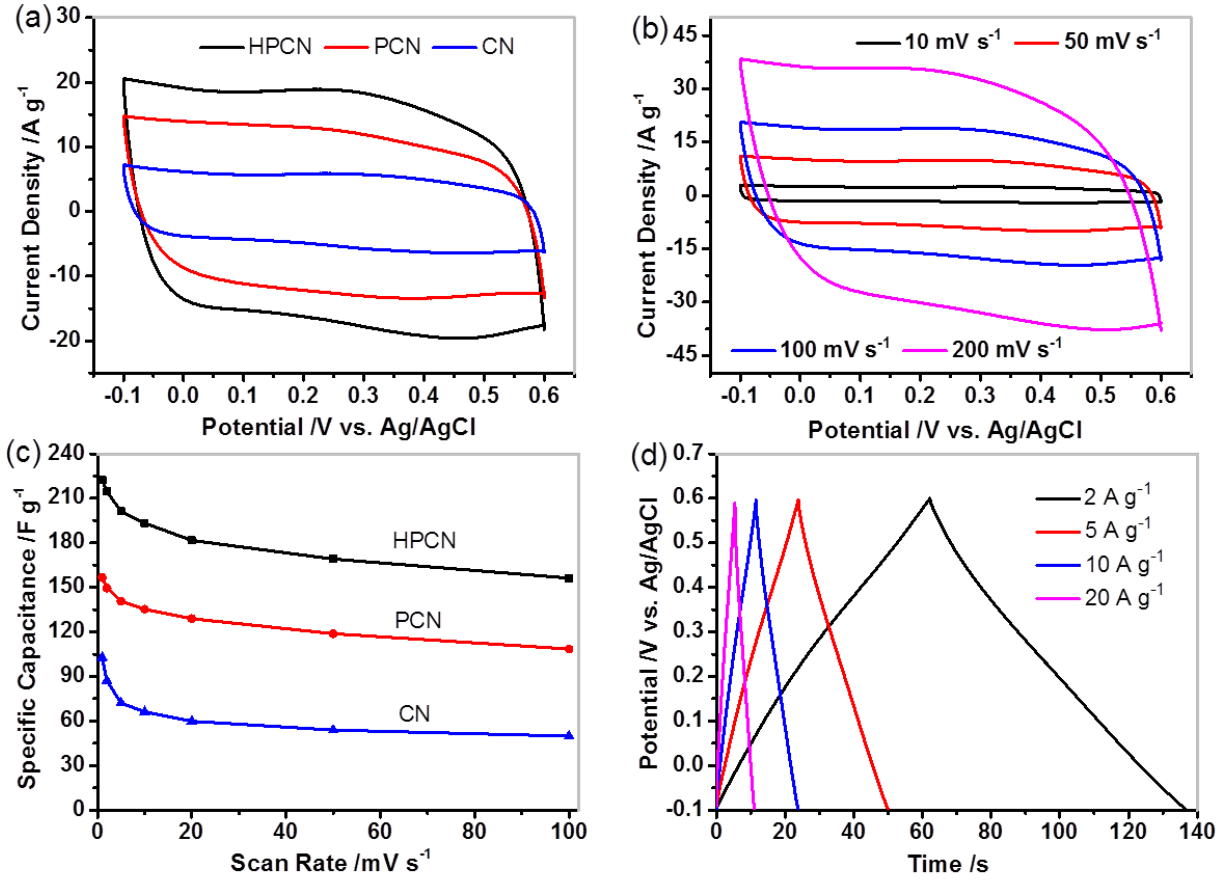

Figure 3.7 (a) CV curves of HPCN, PCN and CN hybrids at a scan rate of 100 mV s^{-1} in 1 M H_2SO_4 aqueous solution; (b) CV curves of HPCN at different scan rate; (c) Specific capacitance as a function of the potential scan rates for HPCN, PCN and CN hybrids; (d) Galvanostatic charge/discharge profiles of HPCN at different current densities.

3.5 Characterization of RuO_2@HPCN

A TEM measurement verifies a markedly reduced porous configuration of RuO_2@HPCN (Figure 3.8a) compared to that of pristine HPCN (as shown in Figure 3.3b). Instead, a dense RuO_2 layer with polycrystal structure is homogeneously decorated on the HPCN surface. This result suggests that the interconnected mesoproes of HPCN serve as

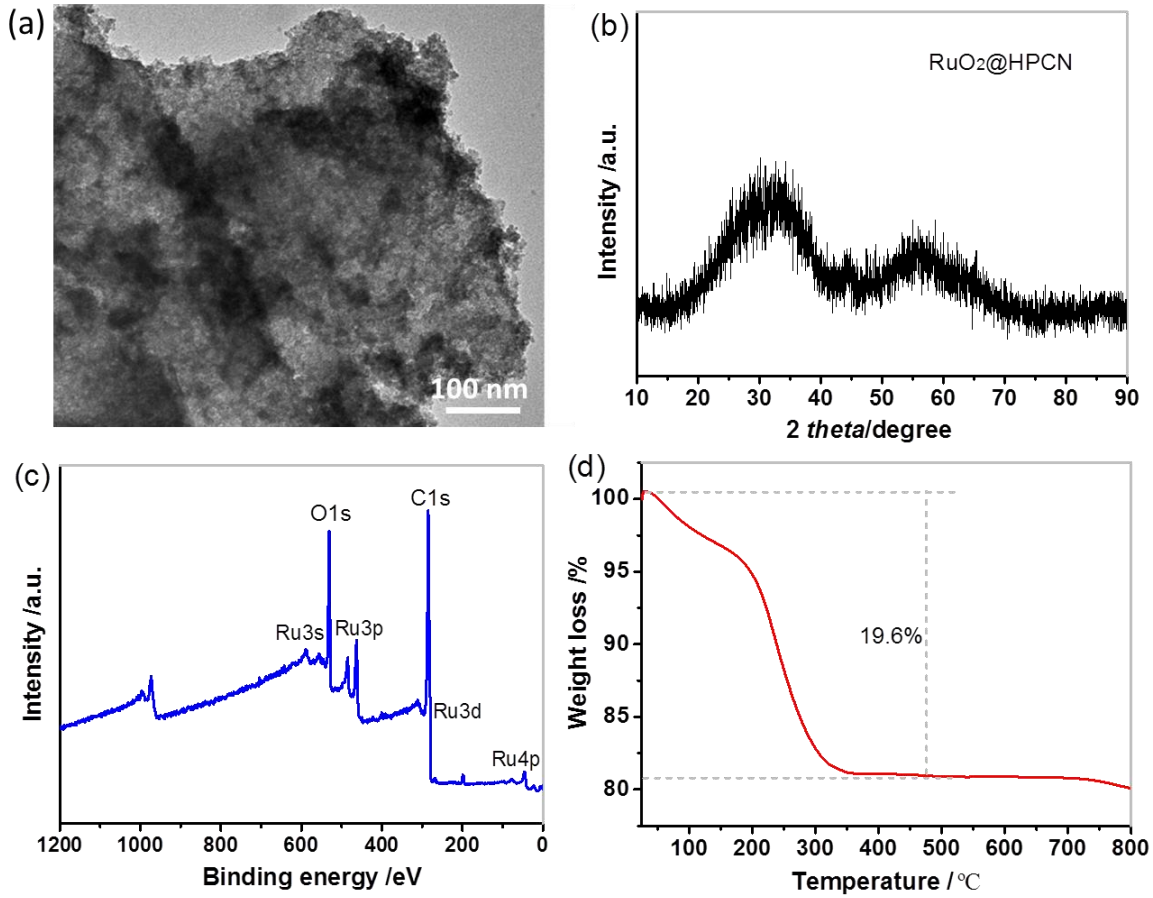

Figure 3.8 Typical TEM image (a) and X-ray diffraction pattern (b) of RuO_2@HPCN; (c) X-ray photoelectron spectroscopy of RuO_2@ HPCN; (d) TGA curve of RuO_2@HPCN carried out in air with a heating rate of 10 ºC min^{-1}.

numerous cavities for incorporation of RuO_2 NPs during the sol-gel deposition process. The phase of RuO_2 in hybrids was characterized by XRD measurement (Figure 3.8b). Notably, the (002) diffraction peak (at ~24.5 ^{o}) corresponding to the HPCN almost disappears, and two broad humps emerged at around 32^o and 54^o are observed, indicating an amorphous feature of RuO_2 NPs due to the low annealing temperature.[33] An XPS measurement was carried out to probe the chemical compositions of RuO_2@HPCN. As shown in Figure 3.8c, several distinct ruthenium signals including 3s, 3p, 3d and 4p appear in addition to the C1s

and O1s signals observed from HPCN (Figure 3.5c).[33] The RuO_2 content in the RuO_2@HPCN composite was further evaluated by thermogravimetric analysis (TGA) to be 80 wt% in an air flow (Figure 3.8d).

3.6 Capacitive performance of RuO_2@HPCN

The electrochemical capacitive performance of RuO_2@HPCN was evaluated based on three-electrode system (same to the measurement of HPCN electrode). Figure 3.9a shows the CV curves of RuO_2@HPCN electrode, which is measured at different scan rates in 1 M H_2SO_4 at a potential range of 0-1 V (vs. Ag/AgCl). In contrast to a HPCN electrode, the RuO_2@HPCN electrode exhibits broad redox peaks in the investigated potential region, which is indicative of a typical pseudocapacitive behavior of RuO_2.[34] Due to the decoration of uniform and electrochemically active RuO_2 NPs, the RuO_2@HPCN hybrids deliver a much higher specific capacitance of 543 F g^{-1} than that of HPCN (222 F g^{-1}) at the same scan rate of 1 mV s^{-1}. Figure 3.9b compares the specific capacitances of RuO_2@HPCN and physically mixed RuO_2/HPCN recorded at different scan rates (between 1-50 mV s^{-1}). Notably, the RuO_2@HPCN electrode displays enhanced rate capability with high specific capacitance at all scanning rates. For instance, a higher specific capacitance of 378 F g^{-1} is obtained at a scanning rate of 50 mV s^{-1} than that of physically mixed RuO_2/HPCN (340 F g^{-1}). This result implies that the mesoporous shells of HPCN not only improve the ion accessibility of hybrids electrode, but also promote the electrochemical faradaic reactions of embedded RuO_2 NPs.

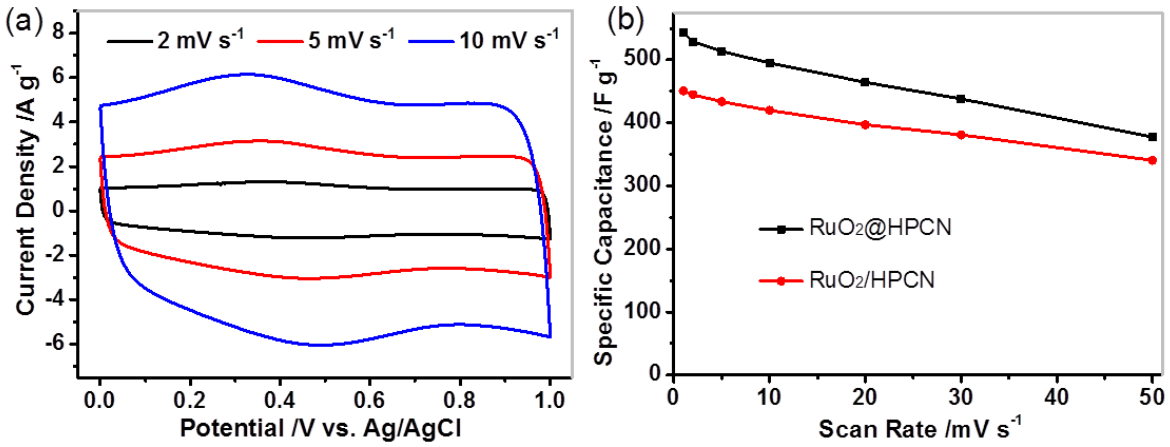

Figure 3.9 (a) CV curves of RuO_2@HPCN at different scan rate; (b) Specific capacitance as a function of the potential scan rates for RuO_2@HPCN and RuO_2/HPCN electrodes.

The above results clearly demonstrate the enhanced electrochemical performance of HPCN and RuO_2@HPCN as electrode materials for SCs, which can be attributed to the highly mesoporous architecture of 2D HPCN, as well as rational incorporation of a pseudocapacitive material (RuO_2). First, HPCN possesses uniform and well-controlled mesopores, which increases the accessible surface area and benefits the formation of electrical double layers; Second, the open and ultrathin porous shells of HPCN can buffer ions and shorten the diffusion distances of electrolyte to the interior space or incorporated RuO_2 NPs; Third, the in-between conductive graphene layers serve as two-dimensional pathways to facilitate electron transport within HPCN or RuO_2@HPCN electrodes.

3.7 Conclusion

In this chapter, we developed a combined self-assembly and nanocasting approach to fabricate graphene-based carbon nanosheet hybrids with highly mesoporous structure (HPCN). Porosity regulation exerted a significant influence on the physicochemical properties and capacitive performance of HPCN. Compared to the conventional porous carbon nanosheets (PCN, produced by physical mixing), HPCN exhibited not only regular mesopore distribution (~12 nm), higher surface area (1273 m^2 g^{-1}) and pore volume (2.6 cm^3 g^{-1}), but also excellent capacitive performance for electrochemical double-layer capacitors, including high specific capacitance (222 F g^{-1}) and good rate capability (156 F g^{-1} at scan rate of 100 mV s^{-1}). Additionally, the resulting HPCN could serve as novel 2D substrates for incorporating metal oxides (e.g. RuO_2) for application in pseudocapacitors. Porosity engineering of carbon materials in a controlled manner associated with incorporation of pseudocapacitive materials offers new possibilities to develop high-performance electrochemical supercapacitor devices for practical applications.

3.8 References

[1] H. Ji, X. Zhao, Z. Qiao, J. Jung, Y. Zhu, Y. Lu, L. L. Zhang, A. H. MacDonald, R. S. Ruoff, *Nat. Commun.* **2014**, *5*.

[2] M. Winter, R. J. Brodd, *Chem. Rev.* **2004**, *104*, 4245.

[3] H. Wang, Q. Hao, X. Yang, L. Lu, X. Wang, *Electrochem. Commun.* **2009**, *11*, 1158.

[4] S. R. C. Vivekchand, C. Rout, K. S. Subrahmanyam, A. Govindaraj, C. N. R. Rao, *J. Chem. Sci.* **2008**, *120*, 9.

[5] S. Han, D. Wu, S. Li, F. Zhang, X. Feng, *Adv. Mater.* **2014**, *26*, 849.

[6] Z. Xiong, C. Liao, X. Wang, *J. Mater. Chem. A* **2014**, *2*, 19141.

[7] B. G. Choi, M. Yang, W. H. Hong, J. W. Choi, Y. S. Huh, *ACS Nano* **2012**, *6*, 4020.

[8] T. Kim, G. Jung, S. Yoo, K. S. Suh, R. S. Ruoff, *ACS Nano* **2013**, *7*, 6899.

[9] Y. Zhu, S. Murali, M. D. Stoller, K. J. Ganesh, W. Cai, P. J. Ferreira, A. Pirkle, R. M. Wallace, K. A. Cychosz, M. Thommes, D. Su, E. A. Stach, R. S. Ruoff, *Science* **2011**, *332*, 1537.

[10] Z. Niu, J. Chen, H. H. Hng, J. Ma, X. Chen, *Adv. Mater.* **2012**, *24*, 4144.

[11] W. Fan, Y.-E. Miao, Y. Huang, W. W. Tjiu, T. Liu, *RSC Adv.* **2015**.

[12] D. Mhamane, A. Suryawanshi, S. M. Unni, C. Rode, S. Kurungot, S. Ogale, *Small* **2013**, *9*, 2801.

[13] C.-M. Chen, Q. Zhang, C.-H. Huang, X.-C. Zhao, B.-S. Zhang, Q.-Q. Kong, M.-Z. Wang, Y.-G. Yang, R. Cai, D. S. Su, *Chem. Commun.* **2012**, *48*, 7149.

[14] S. Yang, X. Feng, L. Wang, K. Tang, J. Maier, K. Müllen, *Angew. Chem. Int. Ed.* **2010**, *49*, 4795.

[15] J. G. Zhou, H. T. Fang, Y. F. Hu, T. K. Sham, C. X. Wu, M. Liu, F. Li, *J. Phys.Chem. C* **2009**, *113*, 10747.

[16] P. Cui, J. Lee, E. Hwang, H. Lee, *Chem. Commun.* **2011**, *47*, 12370.

[17] C. Mattevi, G. Eda, S. Agnoli, S. Miller, K. A. Mkhoyan, O. Celik, D. Mastrogiovanni, G. Granozzi, E. Garfunkel, M. Chhowalla, *Adv. Funct. Mater.* **2009**, *19*, 2577.

[18] L. Buglione, E. L. K. Chng, A. Ambrosi, Z. Sofer, M. Pumera, *Electrochem. Commun.* **2012**, *14*, 5.

[19] E. Ruiz-Hitzky, M. Darder, F. M. Fernandes, E. Zatile, F. J. Palomares, P. Aranda, *Adv. Mater.* **2011**, *23*, 5250.

[20] Q. Huang, D. Zeng, S. Tian, C. Xie, *Mater. Lett.* **2012**, *83*, 76.

[21] A. Ferrari, J. Meyer, V. Scardaci, C. Casiraghi, M. Lazzeri, F. Mauri, S. Piscanec, D. Jiang, K. Novoselov, S. Roth, *Phys. Rev. Lett.* **2006**, *97*, 187401.

[22] D. Yuan, X. Yuan, W. Zou, F. Zeng, X. Huang, S. Zhou, *J. Mater. Chem.* **2012**, *22*, 17820.

[23] Z. Hu, M. P. Srinivasan, *Microporous Mesoporous Mater.* **2001**, *43*, 267.

[24] R. J. Konwar, M. De, *J. Anal. Appl. Pyrolysis* **2014**, *107*, 224.

[25] K. Jayaramulu, K. K. R. Datta, K. Shiva, A. J. Bhattacharyya, M. Eswaramoorthy, T. K. Maji, *Microporous Mesoporous Mater.* **2015**, *206*, 127.

[26] L. Wei, G. Yushin, *J. Power Sources* **2011**, *196*, 4072.

[27] D. S. Jung, T. H. Hwang, J. H. Lee, H. Y. Koo, R. A. Shakoor, R. Kahraman, Y. N. Jo, M.-S. Park, J. W. Choi, *Nano Lett.* **2014**, *14*, 4418.

[28] P. Guo, Y. Gu, Z. Lei, Y. Cui, X. S. Zhao, *Microporous Mesoporous Mater.* **2012**, *156*, 176.

[29] D. Puthusseri, V. Aravindan, S. Madhavi, S. Ogale, *Energy & Environmental Science* **2014**, *7*, 728.

[30] Z. Lei, N. Christov, X. Zhao, *Energy Environ. Sci.* **2011**, *4*, 1866.

[31] J. Wang, S. Kaskel, *J. Mater. Chem.* **2012**, *22*, 23710.

[32] Z. Fan, J. Yan, T. Wei, L. Zhi, G. Ning, T. Li, F. Wei, *Adv. Funct. Mater.* **2011**, *21*, 2366.

[33] Z. S. Wu, D. W. Wang, W. Ren, J. Zhao, G. Zhou, F. Li, H. M. Cheng, *Adv. Funct. Mater.* **2010**, *20*, 3595.

[34] M. Min, K. Machida, J. H. Jang, K. Naoi, *J. Electrochem. Soc.* **2006**, *153*, A334.

Chapter 4

Nitrogen-Doped Carbon Nanosheets with Size-Defined Mesopores as Highly Efficient Metal-Free Catalyst for the Oxygen Reduction Reaction

Heteroatom-doped (e.g. nitrogen) carbon materials are promising alternatives of high-cost platinum catalysts for efficient oxygen reduction reaction (ORR). Nevertheless, further study is needed in order to design and develop carbon-based catalysts with a desirable activity and durability. In the previous chapter, we proved that porosity regulation exerted a significant influence on the accessible surface area/charge storage of carbon materials in supercapacitor applications. In this Chapter, we demonstrate that such a synthetic protocol associated with heteroatom (nitrogen) doping can promote exposure of active sites and boost the electrocatalytic ORR activity of metal-free carbon catalysts. Remarkably, the as-synthesized nitrogen-doped carbon nanosheets with defined mesopore size of 22 nm (NDCN-22) exhibit a more positive ORR onset potential than that of Pt/C and high diffusion-limiting current approaching that of Pt/C in alkaline medium. Moreover, NDCN-22 shows pronounced electrocatalytic activity and long-term stability towards the ORR under acidic conditions.

4.1 Introduction

Nitrogen-doped carbon materials (NCMs) represent the most investigated metal-free catalysts for the oxygen reduction reaction (ORR). Incorporation of nitrogen within the graphitic lattice can effectively modulate the catalytic sites, chemisorption energy of O_2, and the reaction mechanism ($2e^-/4e^-$) of NCMs, leading to improved electrocatalytic activity for ORR.[1-3] The unique planar structure makes graphene a suitable substrate for the development of NCMs containing numerous catalytic sites with the promise of efficient transport pathways.[4-6] To date, graphene-derived NCMs with various amount and types of nitrogen have been synthesized to promote the ORR activity in alkaline electrolyte.[7-9] However, the metal-free NCMs still suffer from low activity in acidic media, mostly due to the relatively few catalytic sites within the catalysts.[10-12]

As discussed in the last chapter, the uniform mesopores of HPCN afforded a large accessible surface area for ion transport/charge storage and thus enhanced electrochemical performance for supercapacitors. Given that the catalyst structure is highly related to the transport properties and exposure of the active sites, in this Chapter, we extend our synthetic protocol to fabricate a series of nitrogen-doped carbon nanosheet (NDCN) catalysts with size-defined mesopores. The pore size of NDCN is precisely tailored by assembly of colloidal silica template with different particle sizes. Surface coating of polydopamine (PDA) followed by pyrolysis and removal of the silica template yield NDCN with abundant and exposed highly electroactive sites (graphitic- and pyridinic-N). The optimization of mesopore size of NDCN as well as their detailed electrocatalytic studies in both alkaline and acidic media will be presented. Notably, NDCN with a mesopore size of 22 nm (NDCN-22) exhibits the highest ORR performance, with a well-defined plateaux for

the diffusion-limiting current and a more positive onset potential than that of a Pt/C catalyst in an alkaline medium (–0.01 V vs. –0.02 V). Moreover, the NDCN-22 catalyst manifests pronounced catalytic activity in acidic medium, with mainly a 4-electron transfer process, an ORR onset potential of 0.72 V versus the reversible hydrogen electrode (RHE) and a high current density of 3.57 mA cm^{-2} at 0.50 V.

4.2 Fabrication of nitrogen-doped carbon nanosheets

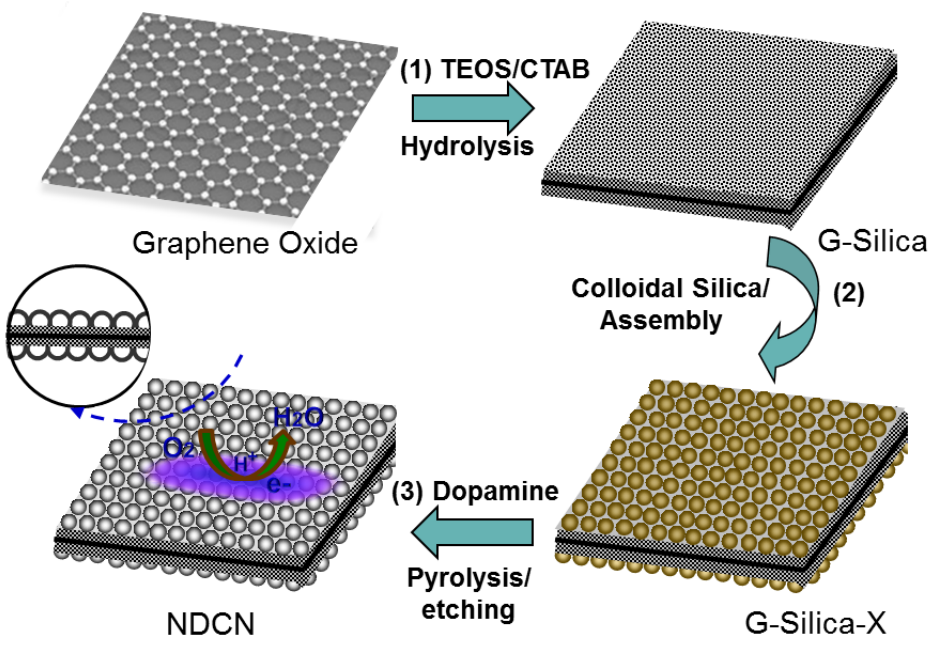

Figure 4.1 Synthetic procedures of NDCN catalysts. (1) CTAB-directed hydrolysis of TEOS on GO nanosheets; (2) Electrostatic assembly of G-silica and colloidal silica NPs; (3) Self-polymerization of dopamine, pyrolyisis, and silica removal treatment.

The overall synthetic procedure for the NDCN is presented in Figure 4.1. Graphene-based silica template with mesopore size of 2 nm (G-silica-2), and the G-silica-X template

comprising G-silica-2 sandwiched by close-packed silica nanoparticles (NPs) are synthesized according to the procedures of G-silica-I/-II in Chapter 3; X represents the particle size of colloidal silica template or the pore size of the resultant NDCN. G-silica-X is dispersed in an aqueous solution of dopamine (DA), and homogeneous PDA layers are readily coated onto the G-silica-X surface by the self-polymerization of DA.[13, 14] The subsequent thermal treatment of PDA-coated G-silica-X in nitrogen combined with etching of the silica template generate NDCN-X with size-defined mesopores. The detailed fabrication procedure is described in the Experimental part (7.3).

4.3 Characterizations

4.3.1 Morphology and structure

The morphology of as-prepared G-silica-2 was first characterized by transmission electron microscopy (TEM) measurements. As shown in Figure 4.2a, free-standing graphene/silica sheets with flat shape and mesoporous structure were observed. The silica shells comprised homogenous mesopores with the size of ~2 nm.[15] Further, TEM measurement verified the successful fabrication of G-silica-7 and G-silica-22 (Figures 4.2b and c). Notably, neither free silica NPs nor bare areas of G-silica-2 were observed. For comparison, silica-22 was mixed with pristine G-silica-2 without PDDA functionalization. It was found that most of the silica-22 were randomly distributed around the G-silica-2 instead of uniform coating (Figure 4.2d), thus validating the electrostatic interaction as the crucial driving force of assembly.

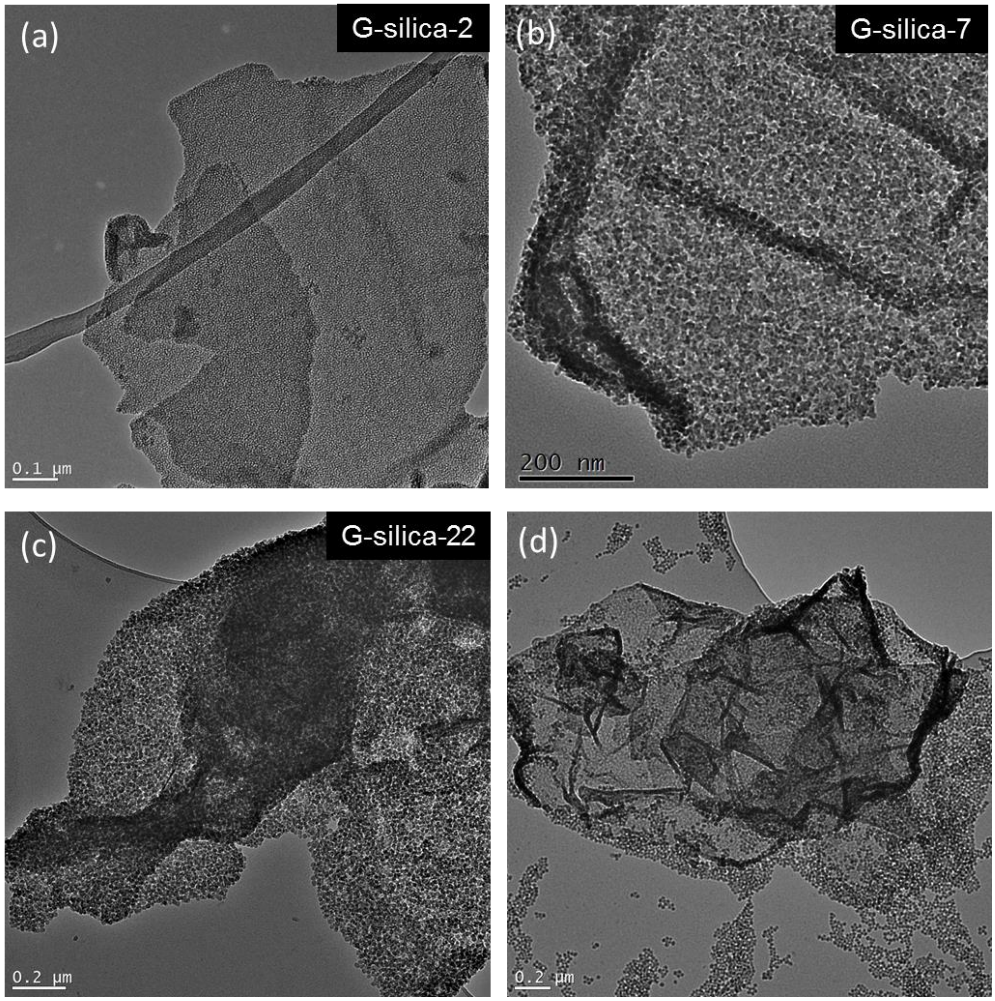

Figure 4.2 (a) Typical TEM image of G-silica-2; (b, c) TEM image of resulting G-silica-7/-22, revealing the uniform adhesion of silica-7/-22 on the surface of G-silica-2; (d) TEM image of G-silica-22 obtained via mixing silica-22 and pristine G-silica-2 (without PDDA functionalization), disclosing a random distribution of silica NPs around G-silica. Such comparative results highlight the significant role of electrostatic interaction as driving force for the self-assembly.

Gentle stirring of resultant G-silica-22 and G-silica-7 in a DA aqueous solution (buffered to pH 8.5 with Tris) resulted in the spontaneous coating of adherent PDA layers (Figure 4.3a and b). PDA-wrapped G-silica-22 or G-silica-7 was then placed in a tube

furnace for carbonization at 900°C in a nitrogen atmosphere. The carbon layer was continuous without any cracks after thermal treatment, as validated by the TEM measurement (Figure 4.3c and d).

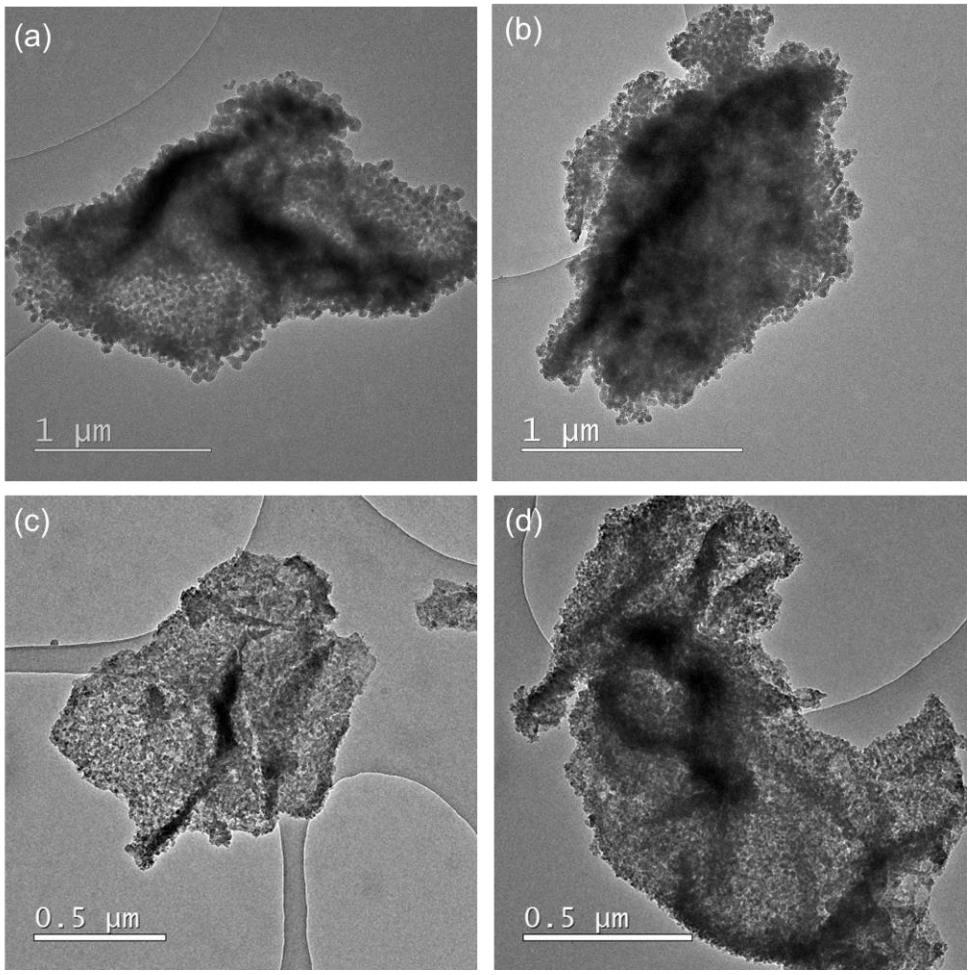

Figure 4.3 TEM images of PDA coated G-silica-22 and G-silica-7 before (a,c) and after (b,d) pyrolysis at 900°C.

The morphology and microstructure of NDCN-22 and NDCN-7 after etching of silica were characterized by TEM measurements (Figures 4.4a, b and e, f, respectively). Both sides of NDCN-22 and NDCN-7 were decorated with uniform and size-defined mesopores. The mesopores were interconnected on the surface of the graphene to form 2D planar

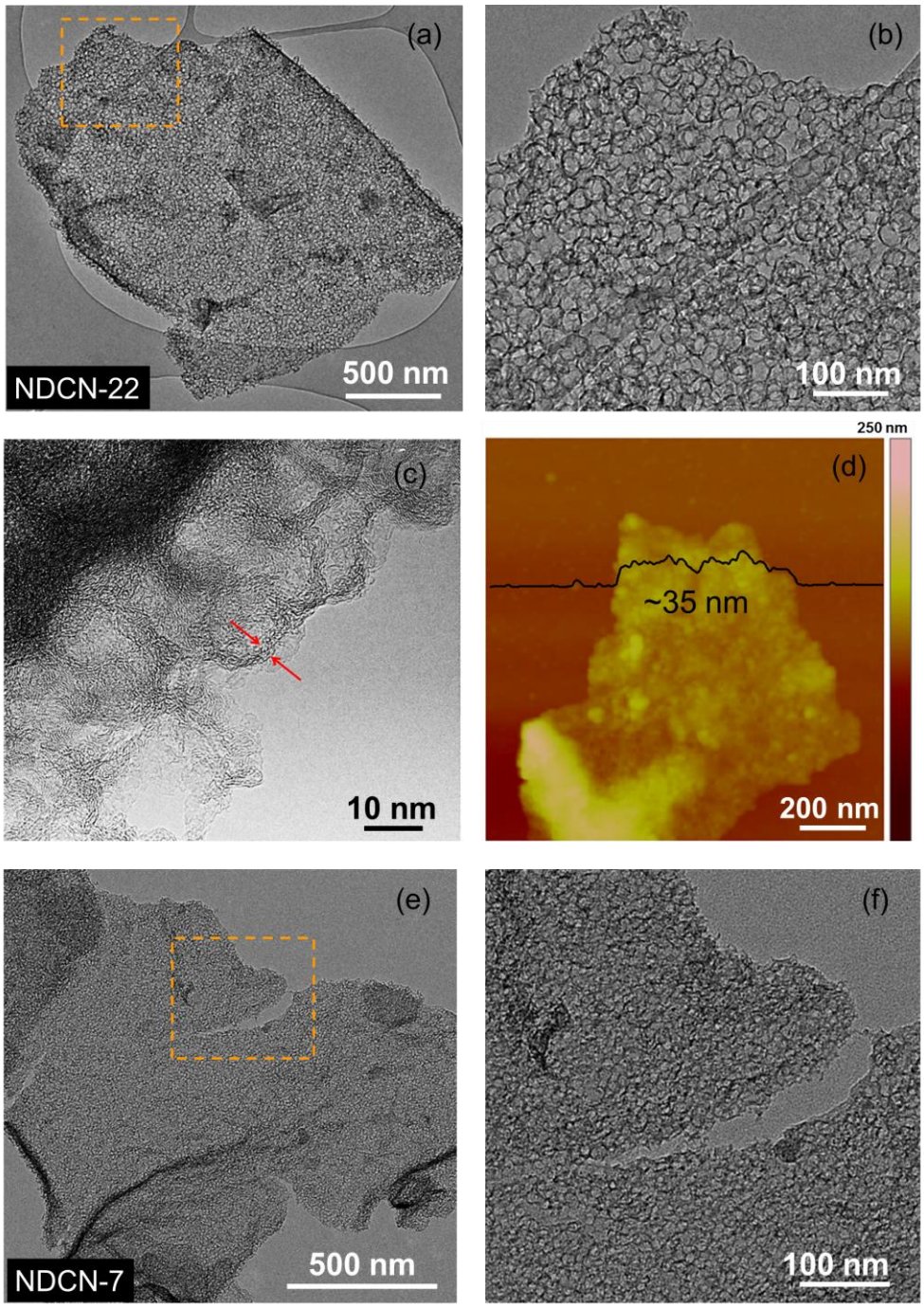

Figure 4.4 Morphology of NDCN-22 (a, b) and NDCN-7 (e, f); image (b) and (f) are of the magnified square regions marked in (a) and (e) respectively. (c) HR-TEM image of NDCN-22, revealing a shell wall thickness of ≤5 nm; (d) Representative AFM image of NDCN-22 and the corresponding thickness analysis taken around the black line.

mesoporous shells. High-resolution TEM (HR-TEM) of NDCN-22 disclosed that the carbon layer obtained was less than 5 nm in thickness (Figure 4.4c). The typical atomic force microscopy (AFM) image and thickness analyses of NDCN-22, shown in Figure 4.4d, revealed a 2D porous feature with an average thickness of 35 nm.

The wall thickness of the catalysts could be controlled by adjusting the polymerization time of DA, which was elucidated by the thickness variation of NDCN-22 (Figure 4.5). TEM measurement indicated that the wall thickness of the mesoporous shell of NDCN-22 increased upon raising self-polymerization time of PDA from 6 h to 24 h

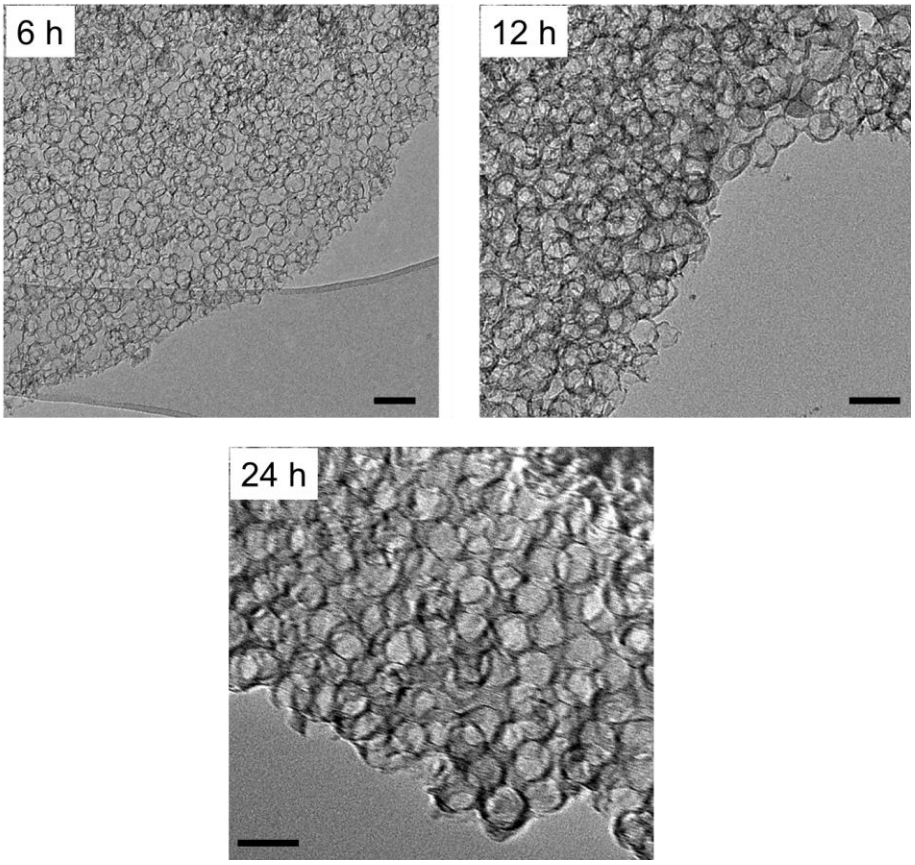

Figure 4.5 Wall thickness evolution of the mesoporous shell of NDCN-22. (Scale bar: 50 nm, the head square indicates the self-polymerization time of DA).

Further, control experiments of PDA coating were conducted on pristine graphene nanosheets and G-silica-2 to produce NDCN and NDCN-2 respectively. The morphology of as-obtained NDCN and NDCN-2 was presented in Figure 4.6.

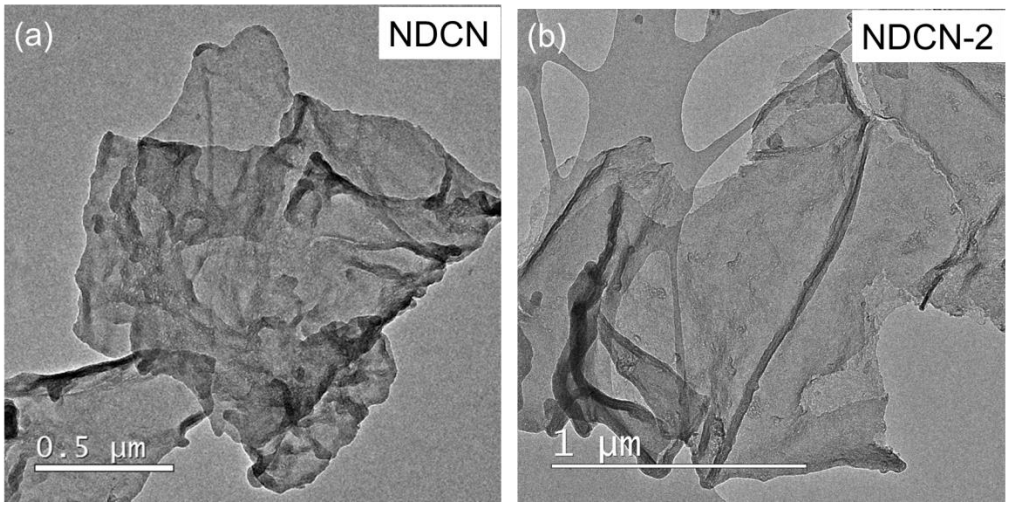

Figure 4.6 Typical TEM images of NDCN (a) and NDCN-2 (b) nanosheets.

4.3.2 Chemical structure and compositions

We then used Raman spectroscopy to identify the graphitic structure of NDCN and NDCN-X samples. In the Raman spectra of samples (Figure 4.7a), two peaks emerge near 1590 cm^{-1} and 1352 cm^{-1}, which can be assigned to the G (graphitic carbon) and D bands (disordered carbon), respectively. The I_D/I_G values (indicated above the spectra) disclose a similar graphitic nature among all prepared samples. X-ray photoelectron spectroscopy (XPS) measurements were carried out to probe the chemical composition of all materials. The survey scan spectra from the XPS analysis reveal the presence of C1s, O1s, and N1s (Figure 4.7b and c). The atomic content is summarized in Table 4.1. As expected, NDCN and NDCN-X show a high content of carbon (above 87.7 at.%) and doped nitrogen with a

narrow content distribution (3.2–3.7 at.%). Typically, NDCN-22 have an atomic content of 89.2%, 7.3%, and 3.5% for carbon, oxygen, and nitrogen, respectively (Figure 4.7c). The complex N1s spectrum can be further deconvoluted into three signals with binding energies of 398.5, 401.0 and 402.4 eV that correspond to pyridinic-N (35.4 at.%), graphitic-N (55.0 at.%) and pyridinic N^{+}-O^{-} (9.6 at.%), respectively (Figure 4.7d).[16, 17]

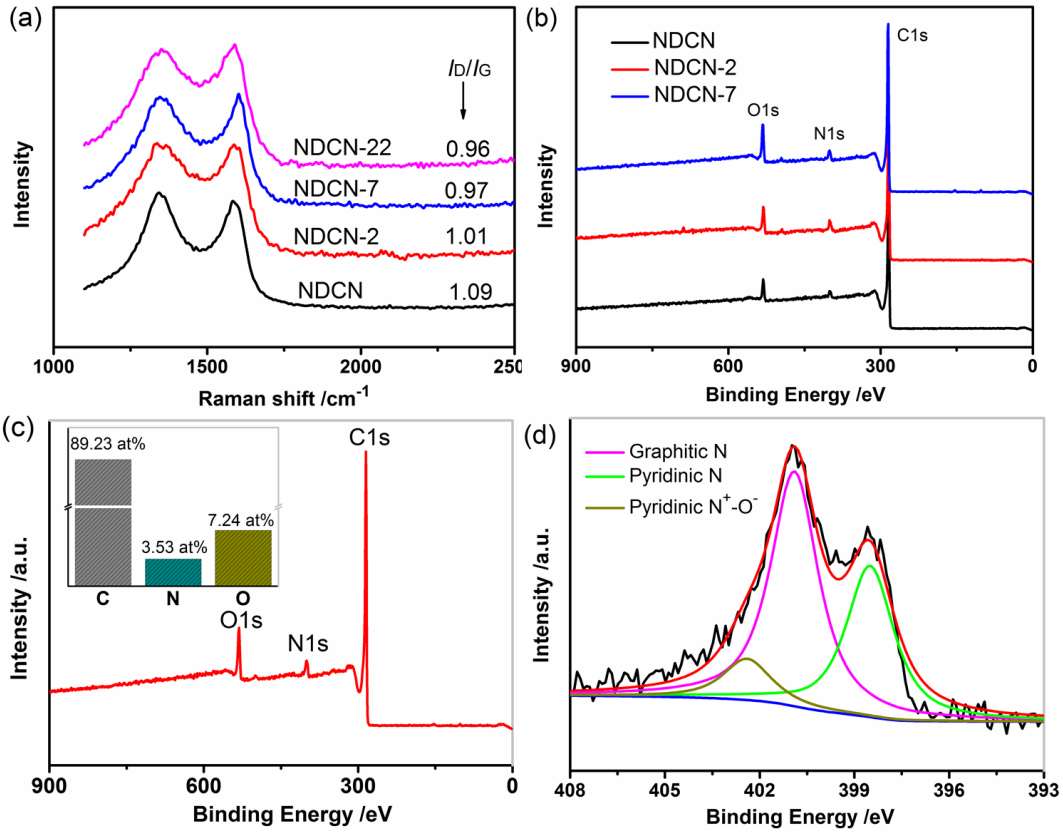

Figure 4.7 (a) Raman spectra of NDCN and NDCN-X and calculated I_D/I_G values; (b) XPS survey spectra of NDCN and NDCN-X. All samples were prepared by PDA-coating for 6 h, pyrolysis at 900 ℃. For NDCN-X, the silica template was further removed by NaOH etching; (c) XPS spectrum and (d) N1s XPS spectrum of NDCN-22. Inset of (c): corresponding atomic content of NDCN-22. The deconvoluted spectrum of N1s fit into three energy components centered around 398.5, 401.0 and 402.4 eV, which correspond to pyridinic-N, graphitic-N and pyridinic N^{+}-O^{-}, respectively.

Table 4.1 Atomic content of NDCN/NDCN-X calculated from the XPS survey spectra.

Elements	NDCN	NDCN-2	NDCN-7	NDCN-22
C (at. ±0.5%)	91.7	88.7	87.7	89.2
O (at. ±0.5%)	5.1	7.9	8.6	7.3
N (at. ±0.5%)	3.2	3.4	3.7	3.5

Further, we evaluated the effect of the pyrolysis temperature on the composition of NDCN-X materials. As typical example, NDCN-22 were synthesized by carbonization of PDA-coated G-silica-22 at 800, 900, and 1000 °C, and the resulting samples were denoted as NDCN-22-800, NDCN-22-900, and NDCN-22-1000, respectively. The XPS analysis revealed that the atomic N content decreased from 5.3 to 3.5 % upon increasing the pyrolysis temperature from 800 to 900 °C (Figure 4.8a and b). Further increase of the pyrolysis temperature resulted in a slight decrease of N content (3.4 % for NDCN-22-1000). It is noteworthy that the shape of the complex N1s spectrum and the fitted signals varied (Figure 4.8c and d), suggesting that different configurations and amounts of N-bonding were formed within NDCN-22 samples. For example, the atomic ratio of graphitic-N/pyridinic-N (Table 4.2) increased from 1.5 to 1.8 %, which might exert a large influence on their electrocatalytic performances for oxygen reduction (see below).

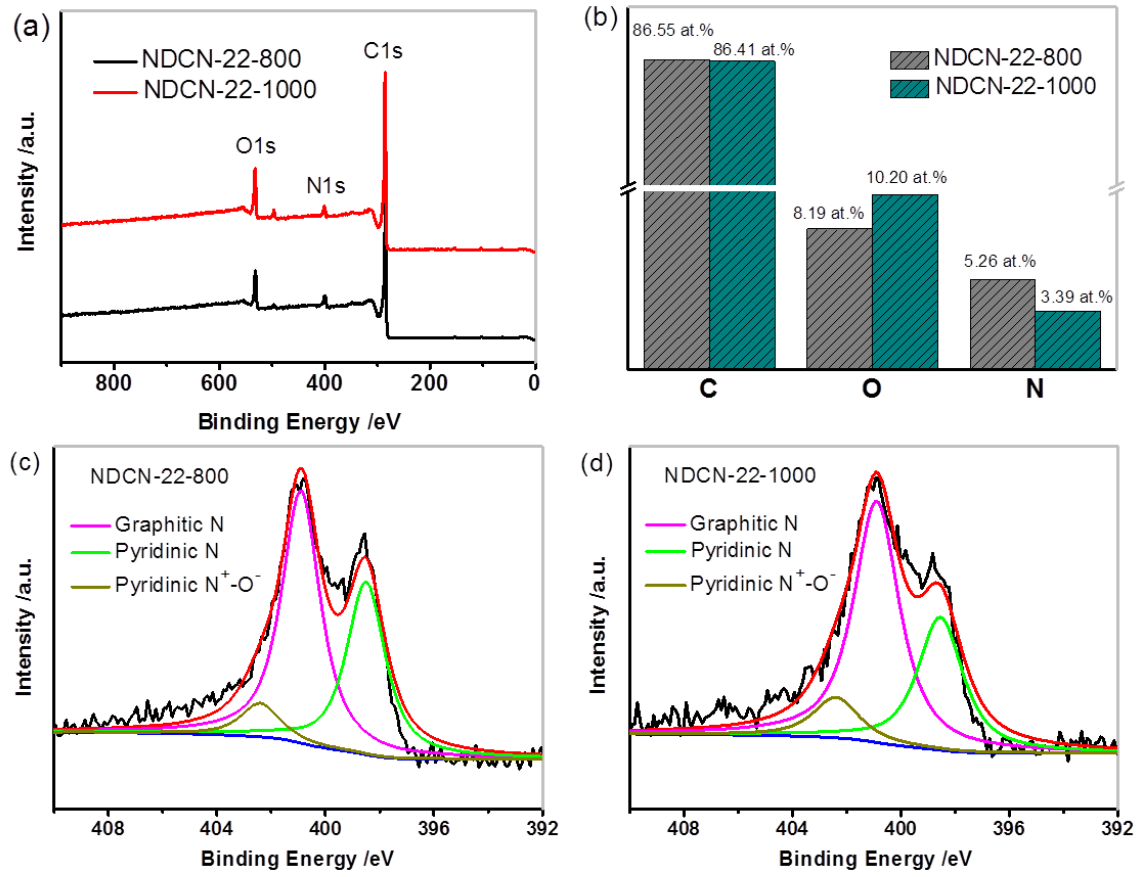

Figure 4.8 XPS survey spectra (a) and corresponding atomic content (b) of NDCN-22-800 and NDCN-22-1000; N1s XPS spectra of NDCN-22-800 (c) and NDCN-22-1000 (d).

Table 4.2 Atomic nitrogen content and ratio calculated from the XPS survey spectra.

Catalysts	N content (at. ±0.5%)	Graphitic N (at. %)	Pyridinic N (at. %)	Pyridinic N^+-O^- (at. %)	Ratio (Graphitic N/Pyridinic N)
NDCN-22-800	5.3	55.0	37.7	7.3	1.5
NDCN-22-900	3.5	55.0	35.4	9.6	1.6
NDCN-22-1000	3.4	58.2	32.0	9.8	1.8

4.3.3 Physicochemical properties

The porous features and Brunauer–Emmett–Teller (BET) specific surface areas of NDCN and NDCN-X were investigated by nitrogen isothermal adsorption/desorption measurements (Figure 4.9a). The BET specific surface areas for NDCN-2, NDCN-7, and NDCN-22 were calculated to be 578, 652, and 589 $m^2\ g^{-1}$, respectively, which were much higher than that of NDCN (55 $m^2\ g^{-1}$). Notably, upon increasing the pore size of NDCN-X, the pore volume significantly increased from 0.38 $cm^3\ g^{-1}$ for NDCN-2 to 1.52 $cm^3\ g^{-1}$ for NDCN-22. The steep increase in nitrogen adsorption for NDCN-22 and NDCN-7 at a relatively high pressure (P/P_0 = 0.80–0.99) clearly suggested that the pore volume was mainly contributed by size-enlarged mesopores.[18] Based on the Barrett–Joyner–Halenda model (Figure 4.9b), the pore size distribution calculated from the adsorption branch revealed the mesoprous feature for all NDCN-X samples. Moreover, NDCN-22 and NDCN-7 exhibited a mesopore distribution peak centered at 22 nm and 7 nm, respectively, consistent with the diameter of the silica-22 and silica-7 template. In contrast, no evident mesopores were observed for NDCN.

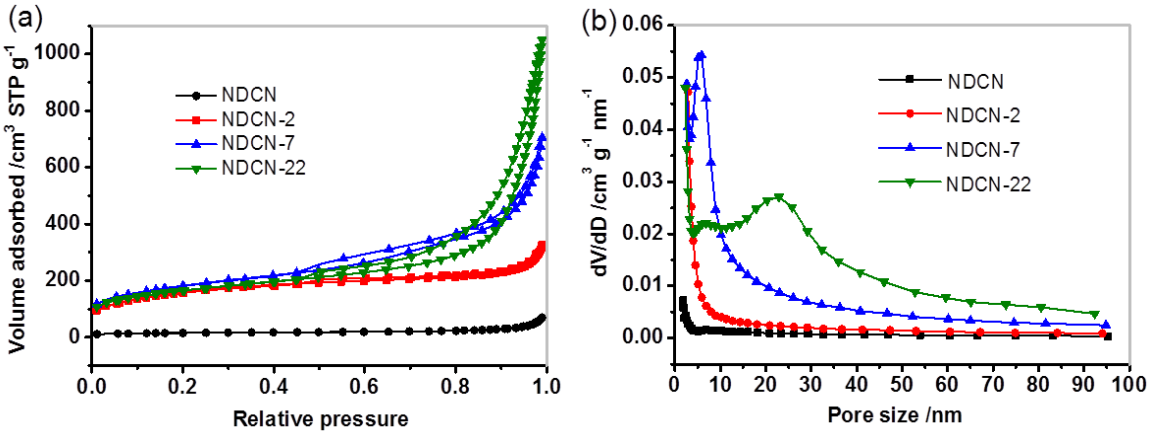

Figure 4.9 Nitrogen adsorption/desorption isotherms (a) and BJH pore distributions (b) of NDCN and NDCN-X.

4.4 Electrocatalytic performance

4.4.1 Alkaline conditions

The electrocatalytic activity of NDCN-X for the ORR was first examined by cyclic voltammetry (CV) in an Ar- or O_2-saturated 0.1 M KOH solution at a scan rate of 100 mV s^{-1}. As shown in Figure 4.10a, a quasi-rectangular voltammogram without any obvious peak was observed for NDCN-22 in the Ar-saturated solution. In contrast, a well-defined cathodic ORR peak, centered at –0.28 V with a high reaction current of –5.8 mA cm^{-2} occurred in the CV analysis when the electrolyte solution was saturated with O_2, highlighting pronounced electrocatalytic activity of NDCN-22 for oxygen reduction. To gain insight into the reaction kinetics of NDCN-22, linear sweep voltammetry (LSV) with a rotating disk electrode (RDE) was undertaken at different rotating speeds from 400 to 2500 rpm in an O_2-saturated 0.1 M KOH solution (Figure 4.10b). NDCN-22 showed a well-defined plateaux of diffusion-limiting currents below –0.3 V at all rotational speeds, indicating an efficient surface electrocatalytic reaction with a direct four-electron transfer pathway. We further used the RDE to probe the pore size effect on the ORR catalytic activity of different catalysts. The LSV results for NDCN and NDCN-X were presented in Figure 4.10c. Notably, the onset potential of all NDCN-X catalysts was more positive than that of NDCN. In particular, NDCN-22 exhibited the most positive half-wave potential ($E_{1/2}$) and the highest kinetic current density among its counterparts (Table 4.3). This result thus strongly suggested that the controlled mesoporous structure in NDCN exerted an essential influence on the electrocatalytic behavior.

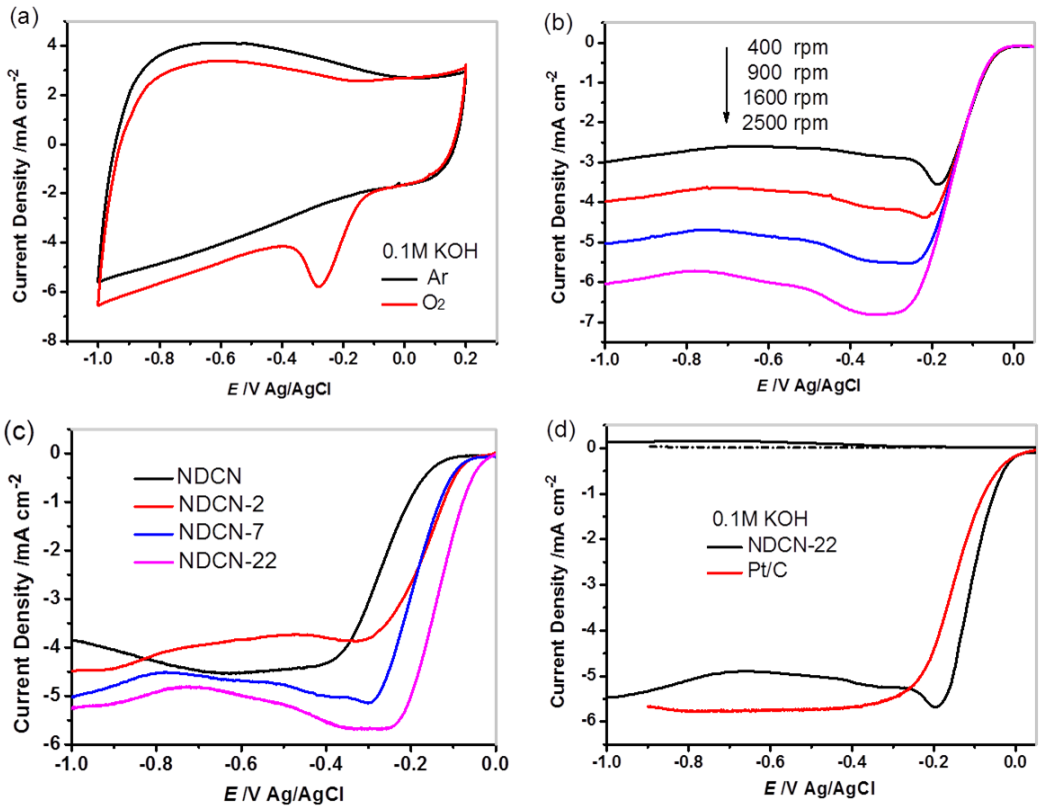

Figure 4.10 (a) CV of NDCN-22 in Ar- and O_2-saturated 0.1 M KOH solution at a scan rate of 100 mV s^{-1}; (b) LSV of NDCN-22 in O_2-saturated 0.1 M KOH at a scan rate of 10 mV s^{-1} at different RDE rotation rates; (c) LSV of NDCN and NDCN-X in O_2-saturated 0.1 M KOH at a scan rate of 10 mV s^{-1} with an RDE rotation rate of 1600 rpm; (d) RRDE polarization curves for NDCN-22 and Pt/C in O_2-saturated 0.1 M KOH at a scan rate of 10 mV s^{-1} with an RDE rotation rate of 1600 rpm. For all the RDE and RRDE measurements, the loading of catalysts was 20 μg_{Pt} cm^{-2} for Pt/C and 0.6 mg cm^{-2} for NDCN-X and NDCN.

Table 4.3 Comparison of ORR electrocatalytic performance of NDCN and NDCN-X in alkaline condition.

Catalyst	Half-wave potential ($E_{1/2}$, V)	Current density (mA m^{-2}, at -0.28 V)
NDCN	-0.26	2.60
NDCN-2	-0.18	3.70
NDCN-7	-0.19	5.01
NDCN-22	-0.13	5.68

To assess the electrocatalytic activity of NDCN-X, rotating ring-disk electrode (RRDE) measurements were also carried out on NDCN-22 and commercial Pt/C (20 wt%) in O_2-saturated 0.1 M KOH at a rotation rate of 1600 rpm (Figure 4.10d). Remarkably, NDCN-22 exhibited a diffusion-limiting current approaching that of Pt/C (5.45 vs. 5.78 mA cm^{-2}), and even a more positive onset and half-wave potential (–0.01 and –0.11 V) than those of Pt/C (–0.02 and –0.15 V). The ORR performance including the onset/half-wave potential and the diffusion-limiting current are superior to previously reported NCMs as metal-free ORR catalysts in an alkaline medium (summarized in Table 4.4). For example, at the potential corresponding to the cathodic peak in CV curve, NDCN-22 exhibits a current density as high as 5.68 mA m^{-2}, which is much higher than those of reported NCMs (2.0-4.0 mA m^{-2}). The slight decrease in the current density at the overpotential of about –0.2 V might be caused by the rapid O_2 consumption in the test cells. On the basis of the ring and disk currents, the electron transfer number (n) for NDCN-22 was calculated to be 3.67−3.94 over the potential range from –0.2 to –0.9 V (Figure 4.11), emphasizing that NDCN-22 proceeded mainly via a four-electron ORR mechanism.

Table 4.4 Comparison of ORR electrocatalytic performance of NDCN-22 with some NCMs catalysts reported in literatures.

Materials	Catalyst loading (mg cm^{-2})	Onset potential (V vs. Ag/AgCl)[a]	Current density (at *E*p, mA m^{-2})[b]
Mesoporous N-doped carbon [19]	~0.66	-0.035	~3.9
N-doped graphene [20]	0.14	-0.10	~2.0
Dual-doped graphene [21]	------	-0.06	~3.0
N-doped carbon spheres [17]	------	-0.1	~2.0
N-doped carbon nanosheets (this work)	0.6	-0.01	5.68

a: the onset potential was measured at the rotation speed of 1600 rpm;

b: the current density was obtained at the potential corresponding to the cathodic peak in cyclic voltammetry (CV) curves; rotation speed: 1600 rpm.

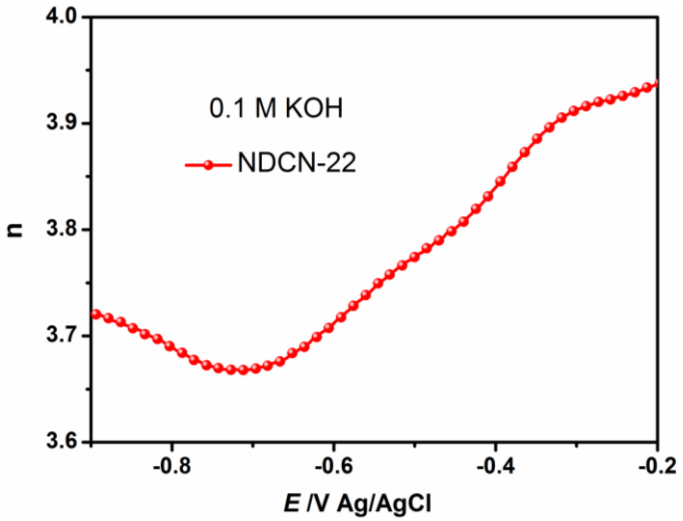

Figure 4.11 Electron transfer number (n) of NDCN-22 as a function of the overpotential in O_2-saturated 0.1 M KOH.

4.4.2 Acidic conditions

The effect of the mesopore size characteristics on electrocatalytic performance in an acidic medium was investigated. The CV curve indicated a significant reduction process for NDCN-22, with a pronounced cathodic ORR peak at 0.50 V versus the reversible hydrogen electrode (RHE) when the electrolyte (0.5 M H_2SO_4) was saturated with O_2 (Figure 4.12a). The RDE polarization curves of NDCN and NDCN-X (Figure 4.12b) indicated that the onset and half-wave potential of catalysts were shifted positively upon increasing pore size, which is in agreement with the trend of their performance in alkaline conditions (Figure 4.10c). RRDE polarization curves for NDCN-22 are presented in Figure 4.12c. It is striking to note that NDCN-22 exhibited high catalytic activity with a more positive onset potential (0.72 V) and much higher current density (3.57 mA cm^{-2} at 0.50 V) than those of reported nitrogen-doped graphene and nanostructured carbon catalysts.[22-24] Moreover, NDCN-22 exhibited an almost four-electron transfer process (n = 3.67–3.91 over the potential 0.03−0.63 V, Figure 4.12d) with a low H_2O_2 yield of 4.3–16.5% over the measured potential range (inset of Figure 4.12c).

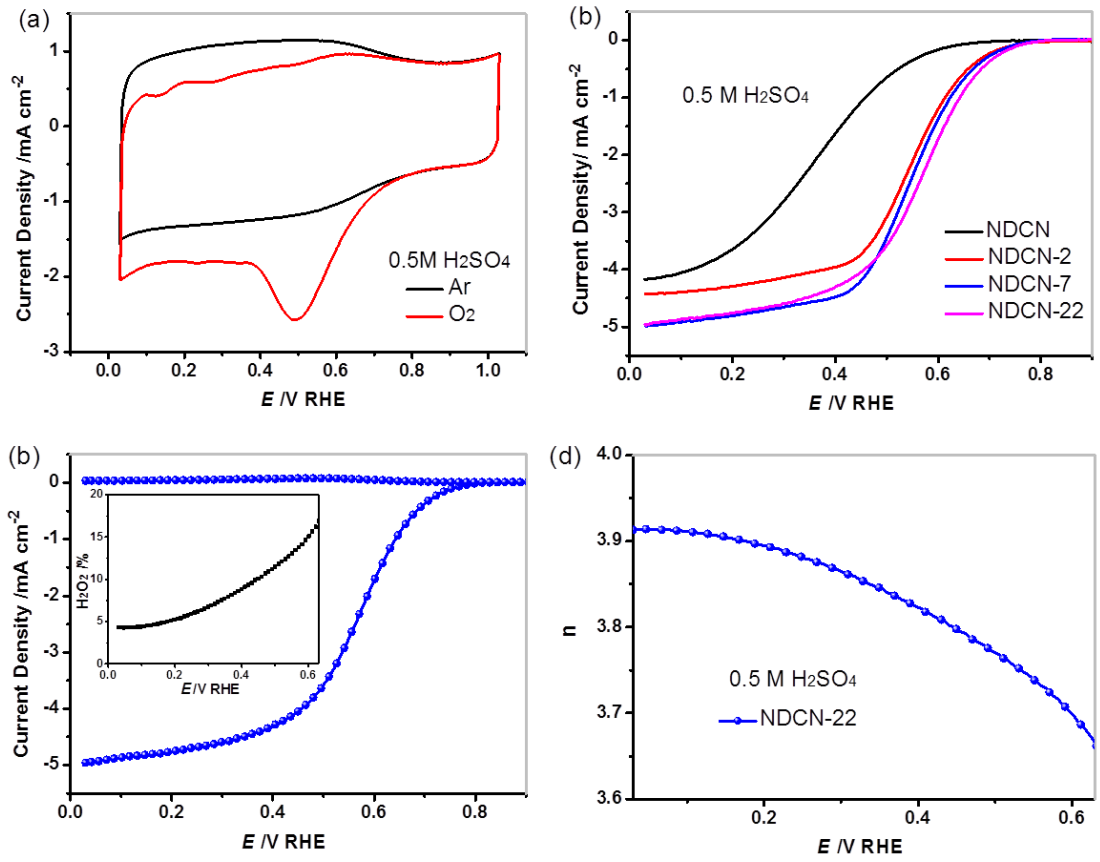

Figure 4.12 (a) CV of NDCN-22 in Ar- and O_2-saturated 0.5 M H_2SO_4 solution at a scan rate of 100 mV s^{-1}; (b) LSVs of NDCN and NDCN-X in O_2-saturated 0.5 M H_2SO_4 at a scan rate of 10 mV s^{-1} with RDE rotation rate of 1600 rpm; (c) The RRDE voltammetric response and H_2O_2 yield plots (inset) of NDCN-22 in O_2-saturated 0.5 M H_2SO_4; (d) Electron transfer number (n) of NDCN-22 as a function of the overpotential in O_2-saturated 0.5 M H_2SO_4. For all the RDE and RRDE measurements, the catalyst loading was 0.6 mg cm^{-2}.

4.4.3 Effect of annealing temperature

As the pyrolysis temperature plays an essential role in the formation of active sites for metal-free carbon catalysts, the activity of NDCN-22-800/-900/-1000 samples was examined. The activity in acidic medium (0.5 M H_2SO_4), as measured by the ORR onset and half-wave potentials ($E_{1/2}$) in the RRDE polarization curves (Figure 4.13), increased from 0.67 and 0.50 V for NDCN-22-800 to 0.72 and 0.56 V for NDCN-22-900. The performance of NDCN-22-1000 is very similar to that of NDCN-22-900. In association with an XPS analysis (Figure 4.8), the atomic ratio of graphitic-N/pyridinic-N (Table 4.2) is assumed to be responsible for the considerable activity enhancement of NDCN-22-900/-1000 compared to NDCN-22-800.[16]

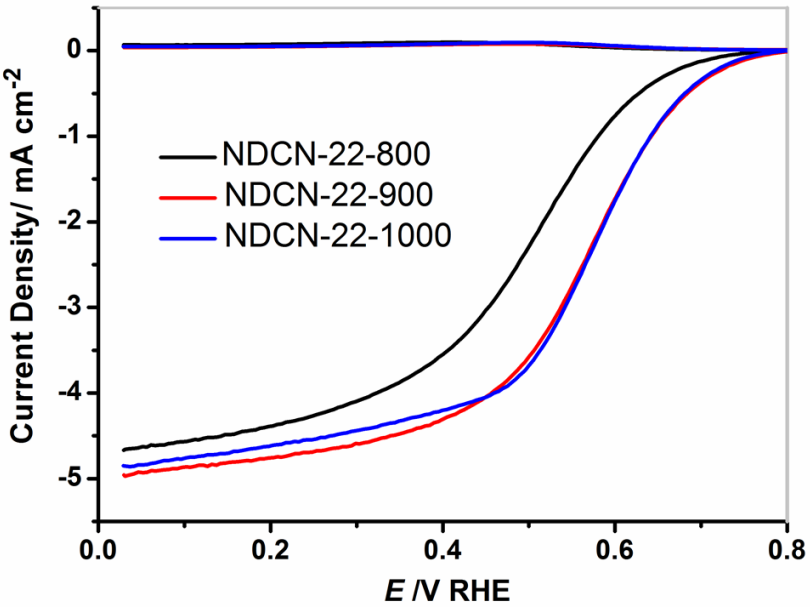

Figure 4.13 RRDE voltammetric response of NDCN-22-800/-900/-1000 in O_2-saturated 0.5 M H_2SO_4.

4.4.4 Durability

The high cycling stability of the NDCN-22-900 catalyst is demonstrated in Figure 4.14. The cycling was carried out with CV within a potential range of 0.6–1.0 V in O_2-saturated 0.5 M H_2SO_4.[4, 34] After 4000 continuous cycles, the half-wave potential $E_{1/2}$ exhibited a small negative shift of ~40 mV under O_2, validating the high durability of NDCN catalysts in acidic medium. The low H_2O_2 yield (Figure 4.12d) of the NDCN-22 catalyst would be beneficial to its electrochemical stability.[25] On the other hand, the active sites were homogeneously distributed in 2D interconnected porous carbon shells of self-supported graphene plane, which would prevent the structural collapse or component detachment.

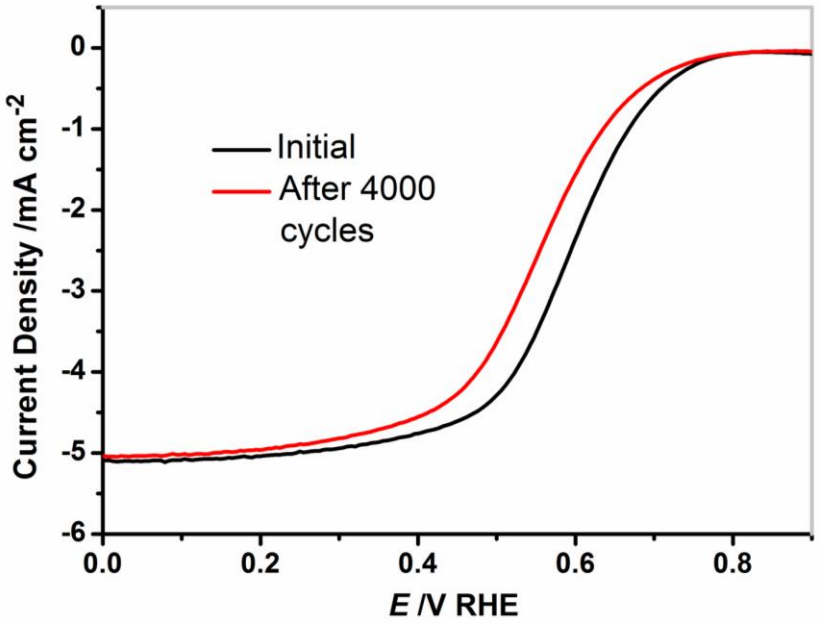

Figure 4.14 Polarization curves for the NDCN-22-900 catalyst before and after 4000 potential cycles in O_2-saturated 0.5 M H_2SO_4. Potential cycling was carried out between 0.6 and 1.0 V versus an RHE at 50 mV s^{-1}.

4.5 Conclusion

In this chapter, we developed a controlled hard template assembly approach to synthesize novel mesoporous nitrogen-doped carbon nanosheets (NDCN). The unique planar porous shells associated with nitrogen doping afforded abundant catalytic sites and facilitated the electrolyte/reactant diffusion of NDCN catalysts for the oxygen reduction reaction (ORR). NDCN catalyst with mesopore size of 22 nm exhibited a more positive ORR onset potential than that of Pt/C and high diffusion-limiting current approaching that of Pt/C in alkaline medium. Moreover, it showed pronounced electrocatalytic activity and long-term stability towards the ORR under acidic conditions. The synthetic strategy toward porous carbon nanosheets described in this work appears to boost the electrocatalytic activity of metal-free catalysts via mesoporosity control, and can be further extended to develop porous non-precious metal catalysts for high-performance ORR.

4.6 References

[1] D. S. Yu, E. Nagelli, F. Du, L. M. Dai, J. *Phys. Chem. Lett.* **2010**, *1*, 2165.

[2] N. Ramaswamy, S. Mukerjee, *Adv. in Phys. Chem.* **2012**, 491604.

[3] F. X. Ma, J. Wang, F. B. Wang, X. H. Xia, *Chem.Commun.* **2015**, *51*, 1198.

[4] H. Fei, R. Ye, G. Ye, Y. Gong, Z. Peng, X. Fan, E. L. G. Samuel, P. M. Ajayan, J. M. Tour, *ACS Nano* **2014**, *8*, 10837.

[5] Q. Wen, S. Wang, J. Yan, L. Cong, Y. Chen, H. Xi, *Bioelectrochemistry* **2014**, *95*, 23.

[6] H.-P. Cong, P. Wang, M. Gong, S.-H. Yu, *Nano Energy* **2014**, *3*, 55.

[7] Y. Zhao, C. G. Hu, Y. Hu, H. H. Cheng, G. Q. Shi, L. T. Qu, *Angew. Chem. Int. Ed.* **2012**, *51*, 11371.

[8] I. Y. Jeon, H. J. Choi, M. Choi, J. M. Seo, S. M. Jung, M. J. Kim, S. Zhang, L. P. Zhang, Z. H. Xia, L. M. Dai, N. Park, J. B. Baek, *Sci. Rep.* **2013**, *3*, 1810.

[9] M. Vikkisk, I. Kruusenberg, U. Joost, E. Shulga, I. Kink, K. Tammeveski, *Applied Catalysis B: Environmental* **2014**, *147*, 369.

[10] Y. G. Li, W. Zhou, H. L. Wang, L. M. Xie, Y. Y. Liang, F. Wei, J. C. Idrobo, S. J. Pennycook, H. J. Dai, *Nat. Nanotechnol.* **2012**, *7*, 394.

[11] W. Xiong, F. Du, Y. Liu, A. P. Jr., M. Supp, T. S. Ramakrishnan, L. M. Dai, L. Jiang, *J. Am. Chem. Soc.* **2010**, *132*, 15839.

[12] C. Jin, T. C. Nagaiah, W. Xia, B. Spliethoff, S. S. Wang, M. Bron, W. Schuhmann, M. Muhler, *Nanoscale* **2010**, *2*, 981.

[13] H. Lee, S. M. Dellatore, W. M. Miller, P. B. Messersmith, *Science* **2007**, *318*, 426.

[14] R. J. Li, K. Parvez, F. Hinkel, X. L. Feng, K. Müllen, *Angew. Chem. Int. Ed.* **2013**, *52*. 5535.

[15] S. B. Yang, X. L. Feng, L. Wang, K. Tang, J. Maier, Klaus Müllen, *Angew. Chem. Int. Ed.* **2010**, *49*, 4795.

[16] K. Parvez, S. B. Yang, Y. Hernandez, A. Winter, A. Turchanin, X. L. Feng, K. Müllen, *ACS Nano* **2012**, *6*, 9541.

[17] K. L. Ai , Y. L. Liu , C. P. Ruan , L. H. Lu , G. Q. Lu, *Adv. Mater.* **2013**, *25*, 998.

[18] X. D. Huang , K. Qian , J. Yang , J. Zhang , L. Li , C. Z. Yu, D. Y. Zhao, *Adv. Mater.* **2012**, *24*, 4419.

[19] W. Yang, T. P. Fellinger, M. Antonietti, *J. Am. Chem. Soc.* **2011**, *133*, 206.

[20] J. Liang, Y. Jiao, M. Jaroniec, S. Z. Qiao, *Angew. Chem. Int. Ed.* **2012**, *51*, 11496.

[21] J. Liang, Y. Jiao, M. Jaroniec, S. Z. Qiao, *Angew. Chem. Int. Ed.* **2012**, *51*, 11496.

[43] M. Chisaka, T. Iijima, A. Tomita, T. Yaguchi, Y. Sakurai, *J. Electrochem. Soc.* **2010**, *157*, B1701.

[44] D. S. Geng, H. Liu, Y. G. Chen, R. Y. Li, X. L. Sun, S. Y. Ye, S. Knights, *J. Power Sources* **2011**, *196*, 1795.

[45] S. Kundu, T. C. Nagaiah, W. Xia, Y. M. Wang, S. V. Dommele, J. H. Bitter, M. Santa, G. Grundmeier, M. Bron, W. Schuhmann, M. Muhler, *J. Phys. Chem. C* **2009**, *113*, 14302.

[46] K. Kwon, Y. J. Sa, J. Y. Cheon, S. H. Joo, *Langmuir* **2012**, *28*, 991.

[47] H. W. Liang, W. Wei, Z. S. Wu, X. L. Feng, K. Müllen, *J. Am. Chem. Soc.* **2013**, *135*, 16002.

Chapter 5

Assembly of Electrochemically Exfoliated Graphene/Nanoparticle Two-Dimensional Hybrids

In previous chapters, controllable assembly of graphene hybrid materials (GHMs) was achieved using graphene oxide (GO) as the basic building blocks. Although GO can be produced in bulk scale with high solution-processability, the large amount of defect density and low electrical conductivity constitute the major drawbacks. Recently, high-quality electrochemically exfoliated graphene (EEG) emerged as attractive target for replacing GO to produce GHMs on a large scale and low cost. However, owing to the hydrophobic nature and inert surface properties, solution processing and hybrid assembly of EEG remain the major challenges. To overcome the intrinsic limitations, in this Chapter, we establish a novel strategy to synthesize two-dimensional GHMs with EEG nanosheets sandwiched by functional nanoparticles (NPs). Polyaniline (PANI), in the emeraldine base form, is used as bi-functional agent that adsorbs on EEG sheets and drives assembly of functional NPs and EEG sheets. This methodology can be applied to fabricate various new EEG hybrids, including EEG-Si, EEG-Fe_3O_4 and EEG-Pt. Moreover, the EEG-Si hybrids exhibit great potential as an anode material for lithium storage.

5.1 Introduction

Integration of graphene with various functional components is of great importance in materials synthesis, because the formation of graphene hybrid materials (GHMs), preferably by a controlled assembly procedure, can lead to unconventional properties and diverse applications.[1-3] Owing to the presence of oxygen containing functional groups, engineering GO surface through either covalent (chemical modification and grafting) [4-6] or non-covalent (π-π stacking, hydrogen-bonding, electrostatic interactions) [7-9] approach was feasible to anchor various organic or inorganic species. However, the bottleneck of GO-derived building block is their poor quality in terms of structural defects and low electrical conductivity. Within the scope of production techniques for graphene (e.g. mechanical cleavage, liquid-phase exfoliation, and chemical vapor deposition, amongst others), electrochemical exfoliation is considered as one of the most desirable routes to prepare high-quality graphene in a large scale under mild conditions.[10-12] Very recently, mass production of electrochemically exfoliated graphene (EEG) with low defect density and remarkable electronic properties in aqueous solutions was realized,[13-15] which opened up enormous opportunities to fabricate various GHMs for numerous advanced applications.

Assembly of EEG into GHMs requires the individual dispersion of EEG in solvent medium and strong interface interactions between EEG and functional compounds. Similar to the processing approaches for RGO, non-covalent wrapping with surfactants or polymers offers alternative solutions to stabilize EEG in aqueous medium and introduce adequate functional groups on EEG surface.[16] However, the presence of foreign stabilizers is undesirable for most applications due to their limited electronic conductivity and poor stability,[17-19] while the complete removal of residual stabilizers involves tedious

purification or pyrolysis that results in high cost. Therefore, overcoming these limitations, to simultaneously build up EEG assembly or hybrids with well-defined nanostructures, as well as to retain the superior properties of EEG, has become the main challenge for the further development of hybrid materials based on EEG.

In this Chapter, we present a facile bottom-up strategy to construct a series of novel 2D hybrids with EEG nanosheets sandwiched by different colloidal nanoparticles (CNPs). Polyaniline (PANI), in the emeraldine base form (PANB), was employed as a bi-functional linker to bridge the counterparts of EEG and CNPs via a self-assembly approach. Specially, the backbone chains of PANB spontaneously adsorb on the EEG surface via π-π interactions, whereas the exposed amine/imine groups serve as numerous reactive sites to couple with CNPs via electrostatic forces and hydrogen-bonding. Importantly, the conductivity of PANB components can be recovered by simple protonic acid doping method, accompanied by a conductivity enhancement of the resulting EEG hybrids. This strategy can be applied to fabricate various 2D hybrids, including EEG-Si, EEG-Fe_3O_4 and EEG-Pt, interesting for a variety of possible applications. As exemplified by EEG-Si hybrids serving as anode material for lithium storage, a high initial reversible capacity (2357 mAh g^{-1} at 105 mA g^{-1}) and excellent cycling stability (86% capacity retention after 100 cycles at 1 A g^{-1}) are achieved. Even at a high current density of 8.4 A g^{-1}, a reversible capacity of 460 mAh g^{-1} is maintained with excellent cycling stability.

5.2 Fabrication of EEG-nanoparticle hybrids

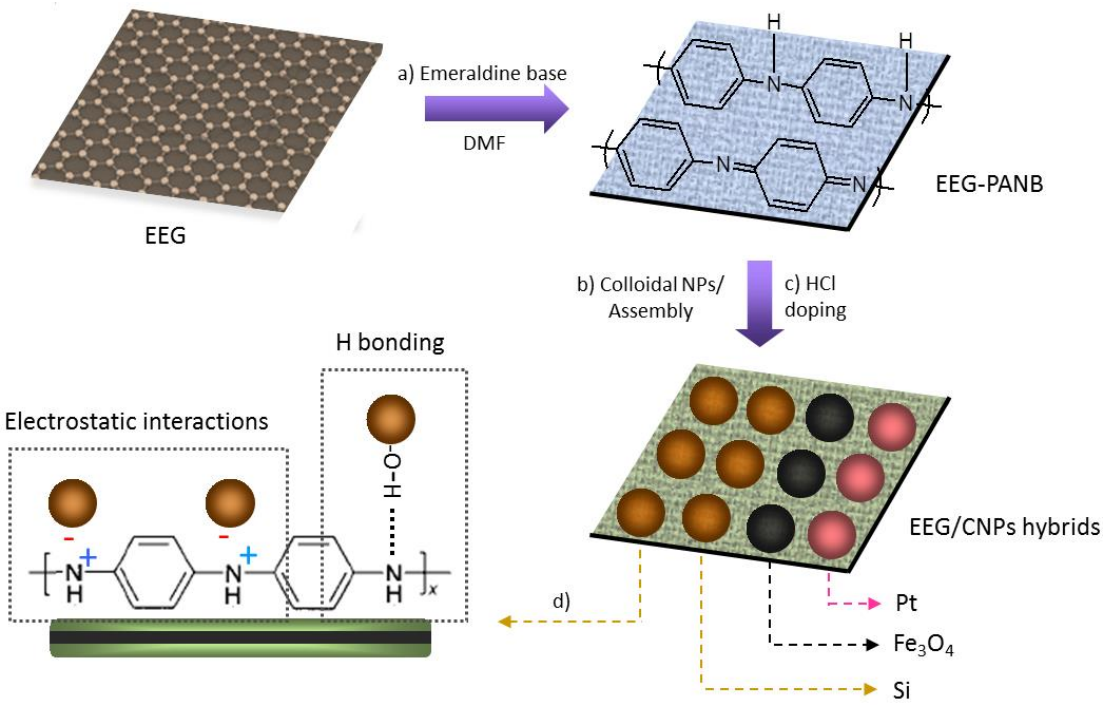

Figure 5.1 Synthetic concept and procedure for EEG-CNP hybrids. EEG is synthesized by electrochemical exfoliation of graphite and used as building block for construction of EEG hybrids. (a) EEG is functionalized with emeraldine base (PANB) in DMF solutions via π-π interactions; (b) EEG-PANB sheets are assembled with a variety of colloidal nanoparticles (CNPs, e.g. Si, Fe_3O_4, Pt) through electrostatic forces and hydrogen bonding interactions; (c) Protonaiton of PANB with HCl gives rise to emeraldine salt (PANS) and enhances the electric conductivity of the EEG hybrids; (d) Simplified cross-section view of interactions between EEG and CNPs.

The overall synthetic procedure of 2D EEG-CNPs hybrids is illustrated Figure 5.1. EEG is first prepared according to a modified procedure via electrochemical exfoliation of graphite (see detailed procedure in the Experimental part).[14] PANB-functionalized EEG (EEG-PANB) is prepared by mixing EEG and PANB component in *N*,*N*-dimethyl

formamide (DMF) with a concentration of 0.1 and 0.2 mg mL^{-1} respectively. Within this step, the PANB molecules are expected to anchor on EEG surface through π-π interactions. Afterwards, CNPs (e.g. Si, Fe_3O_4 and Pt) containing a variety of surface functionalities are added into the EEG-PANB dispersion in DMF. During this process, CNPs are bound with amine/imine groups of PANB and assemble into EEG-PANB via the electrostatic interaction and hydrogen-bonding. Subsequent protonic acid doping with HCl (0.5M) generate EEG-CNPs with sandwich-like nanostructures.

5.3 Characterization of EEG

5.3.1 Morphology of EEG

The microstructure of EEG sheets was examined by scanning electron microscopy (SEM) and transmission electron microscopy (TEM) measurement. As shown in Figure 5.2a and b, free-standing sheets with lateral sizes ranging from hundreds of nanometer to several micrometers are observed. In some cases the sheet edges tend to scroll and fold slightly, which is associated with the flexible and corrugated nature of graphene. The typical atomic force microscopy (AFM) image reveals that EEG has a flake structure (Figure 5.2c), and the height profile verifies that EEG mainly comprises thin sheets (≤3 layers) with a mean thickness of 0.89 nm and 1.56 nm for monolayer and bilayer sheet, respectively (Figure 5.2d).

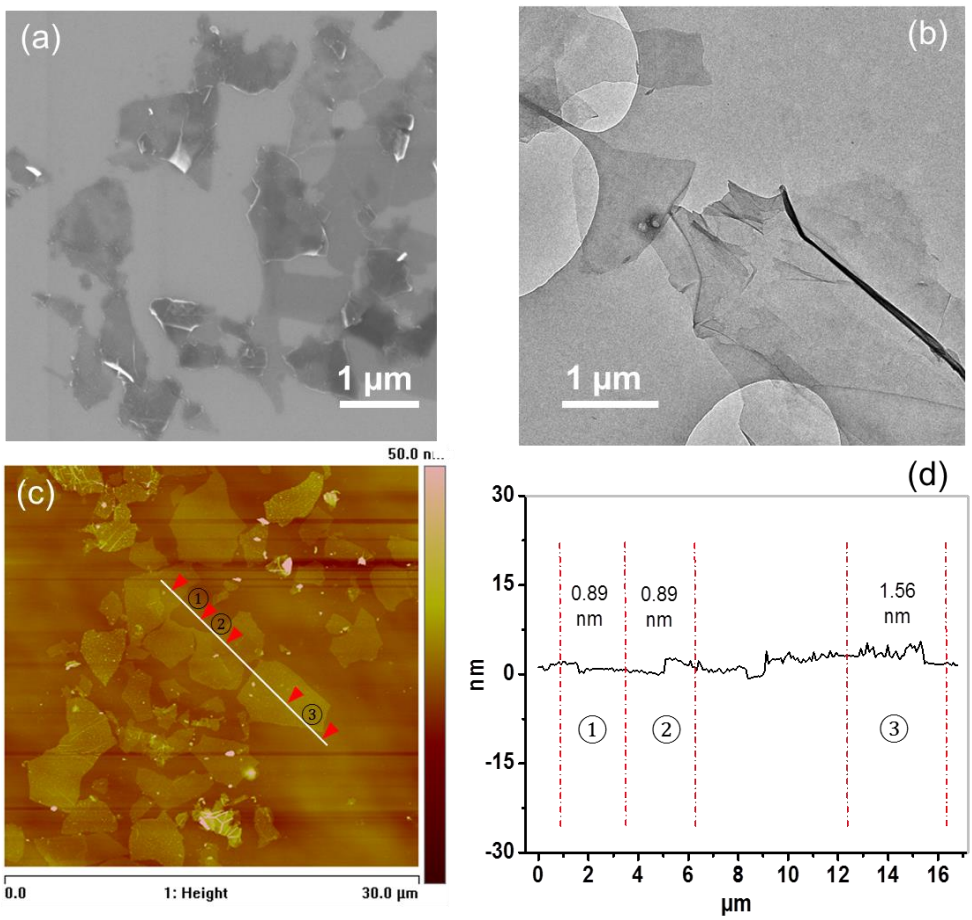

Figure 5.2 Typical SEM (a) and TEM (b) image of EEG sheets; (c) AFM image of EEG sheets; (d) Height profile of EEG taken around the white line in (c), revealing a uniform thickness of 0.89 nm for monolayer and 1.56 nm for bilayer of EEG sheets.

5.3.2 Chemical structure and composition

The chemical nature of the as-prepared EEG sheets was investigated by X-ray photoelectron spectroscopy (XPS). Approximately 13.2 at.% of oxygen is present in EEG, which is attributable to the oxidation of graphene during the electrochemical process (Figure 5.3a). The Raman spectra of EEG sheet display an intense 2D and G peak at ~2704

and ~1584 cm^{-1}, respectively (Figure 5.3b). Moreover, a defect-related D peak is observed at ~1352 cm^{-1}. The intensity ratio of D to G (I_D/I_G) is calculated to be 0.54, which is much lower than that of chemically or thermally reduced GO (~1.2 to 1.5).[20, 21]

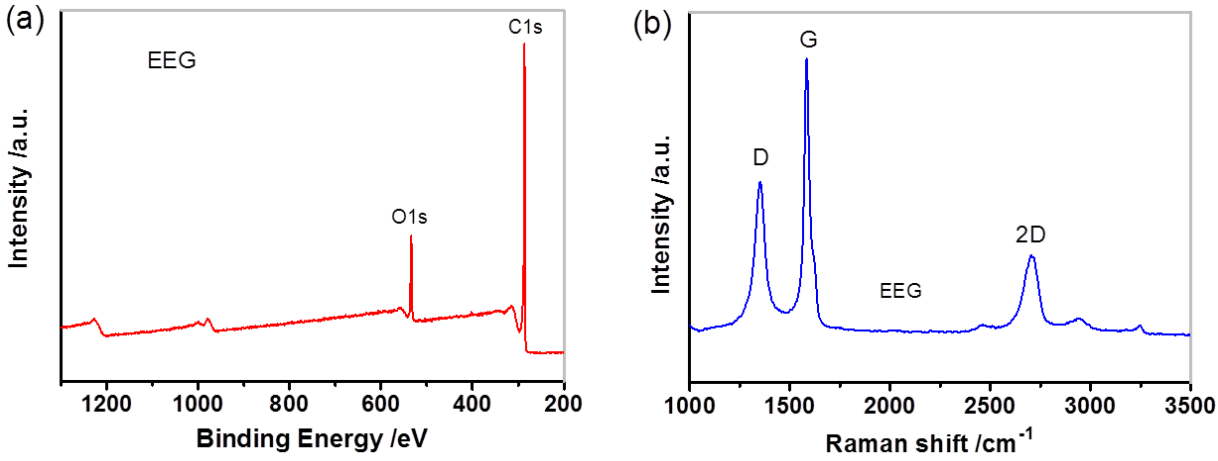

Figure 5.3 XPS (a) and Raman (b) spectra of EEG sheets.

5.4 Characterization of EEG-PANB

EEG was functionalized with PANI via π-π interactions. PANI is known to exist in several different oxidation states including completely reduced, half-oxidized, and completely oxidized polymer,[22] as shown in Figure 5.4. PANI-derived materials were generally obtained as the emeraldine salt (PANS), with less focus on the utilization of the solution-processable polymer form, the emeraldine base (PANB). Compared to other oxidation states, the PANB exhibits multiple advantages for EEG functionalization and processing. First, PANB is the state best suited for processing due to its high solubility in polar aprotic solvents (e.g. DMF),[23] which allow for efficient adsorption and non-covalent functionalization of EEG; second, the PANB contains exposed amine and imine groups,

which provide a sufficient number of binding sites to interact with foreign species; third, the unique electrical switching property of PANB enables to restore the conductivity of the EEG hybrids by simple protonic acid doping (e.g. by HCl).[22]

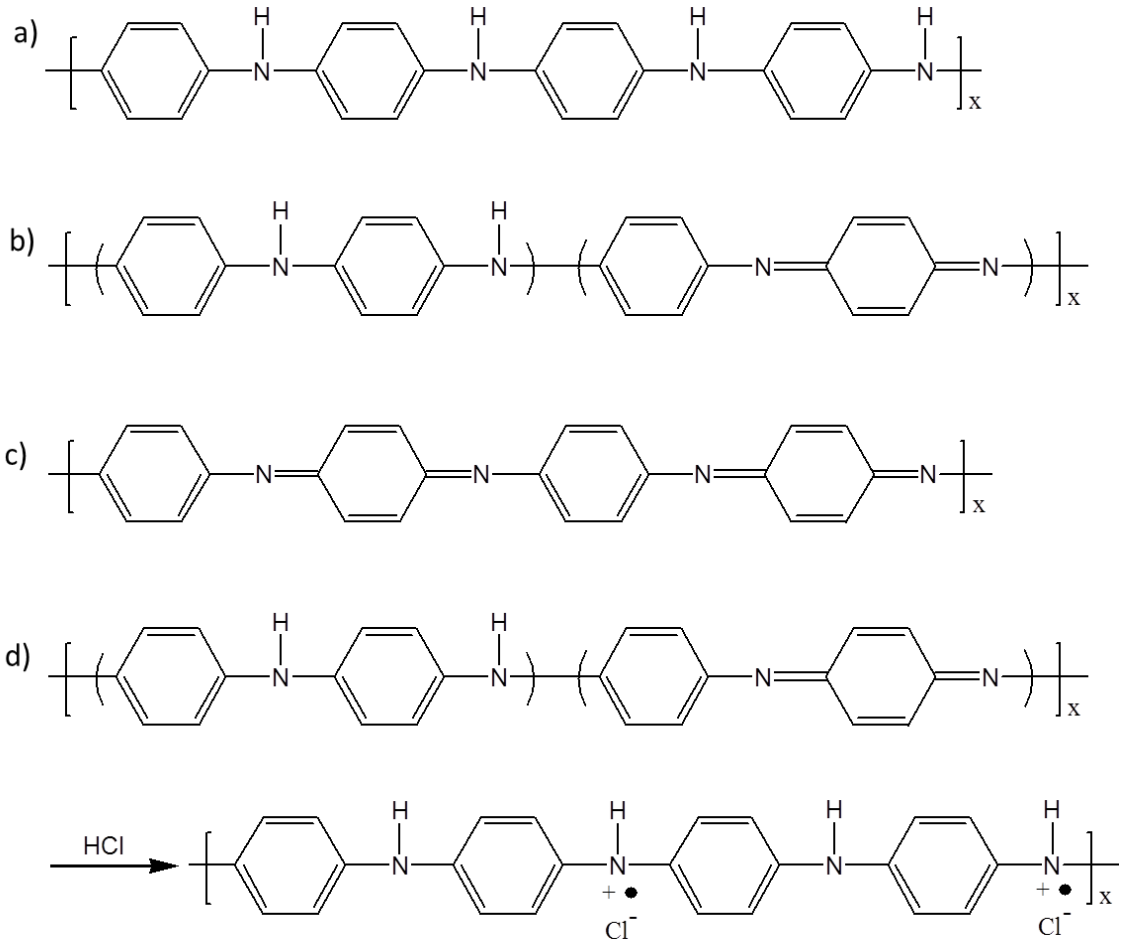

Figure 5.4 Chemical structures of the three oxidation states of polyaniline (PANI), including (a) completely reduced PANI (Leucoemeraldine), (b) half-oxidized PANI (Emeraldine base) and (c) fully oxidized PANI (Pernigraniline); (d) Protonic acid doping of emeraldine base (PANB) and chemical structure of resulting emeraldine salt (PANS).

5.4.1 Morphology of EEG-PANB

Both TEM and high resolution-TEM image (HR-TEM) disclose that as-obtained EEG-PANB possesses a similar morphology as the original EEG sheet, with no obvious PANB agglomerates detected on the EEG surface (Figure 5.5).

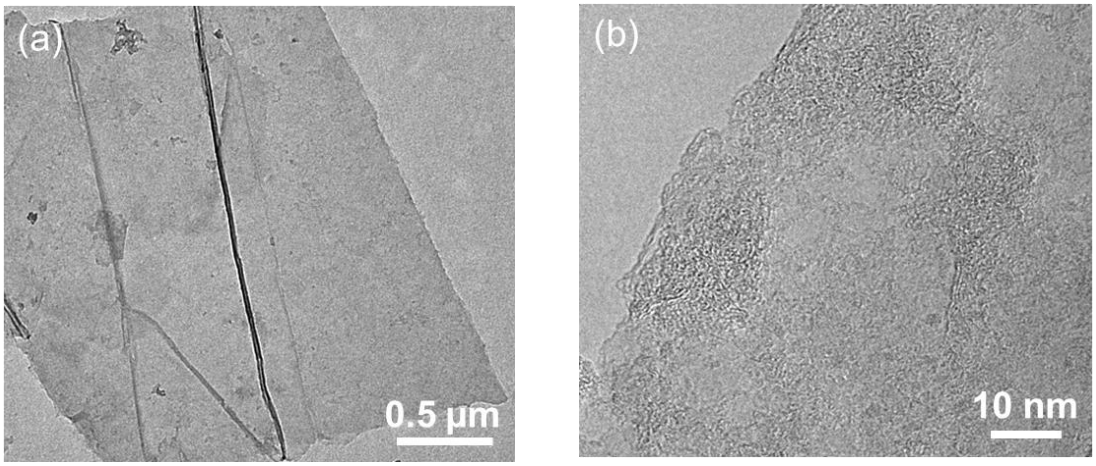

Figure 5.5 Typical TEM (a) and HR-TEM (b) image of EEG-PANB.

5.4.2 Chemical structure and composition

The chemical structure of EEG-PANB was investigated by Fourier-transform infrared (FT-IR) and Raman spectroscopy measurements. In the FT-IR spectrum (Figure 5.6a) of EEG-PANB, the peaks at 1581, 1496, 1311, 1168 and 830 cm^{-1} are consistent with the profiles of pure PANB, and correspond to the vibration of –C=N, -C=C, -C-N and -C-H in-plane bending and out-of-plane deformation, respectively.[24] In the Raman spectra of EEG-PANB (Figure 5.6b), three representative peaks arising from PANB can be observed at 1163, 1224 and 1484 cm^{-1} in addition to the D, G and 2D band of EEG, which are associated with the C-H vibrations and C-N, C=N stretching of PANB chains.[25] Notably,

the G-band of EEG-PANB (1568 cm^{-1}) is downshifted by 12 cm^{-1} compared to that of EEG (1580 cm^{-1}) (inset of Figure 5.6b), suggesting the strong electronic coupling between EEG and PANB (n-type doping of EEG).[7] XPS was used to probe the chemical compositions of EEG-PANB. The XPS spectra reveal the presence of C1s, O1s, and N1s (Figure 5.6c). Typically, the EEG-PANB has an atomic content of 88.9, 8.0 and 3.1% for carbon, oxygen and nitrogen, respectively. The complex N1s spectra can be further deconvoluted into three signals with binding energies of 398.8, 399.9 and 402.0 eV that correspond to ═N─, ─NH─ and ─N^{+}─, respectively (Figure 5.6d).[26]

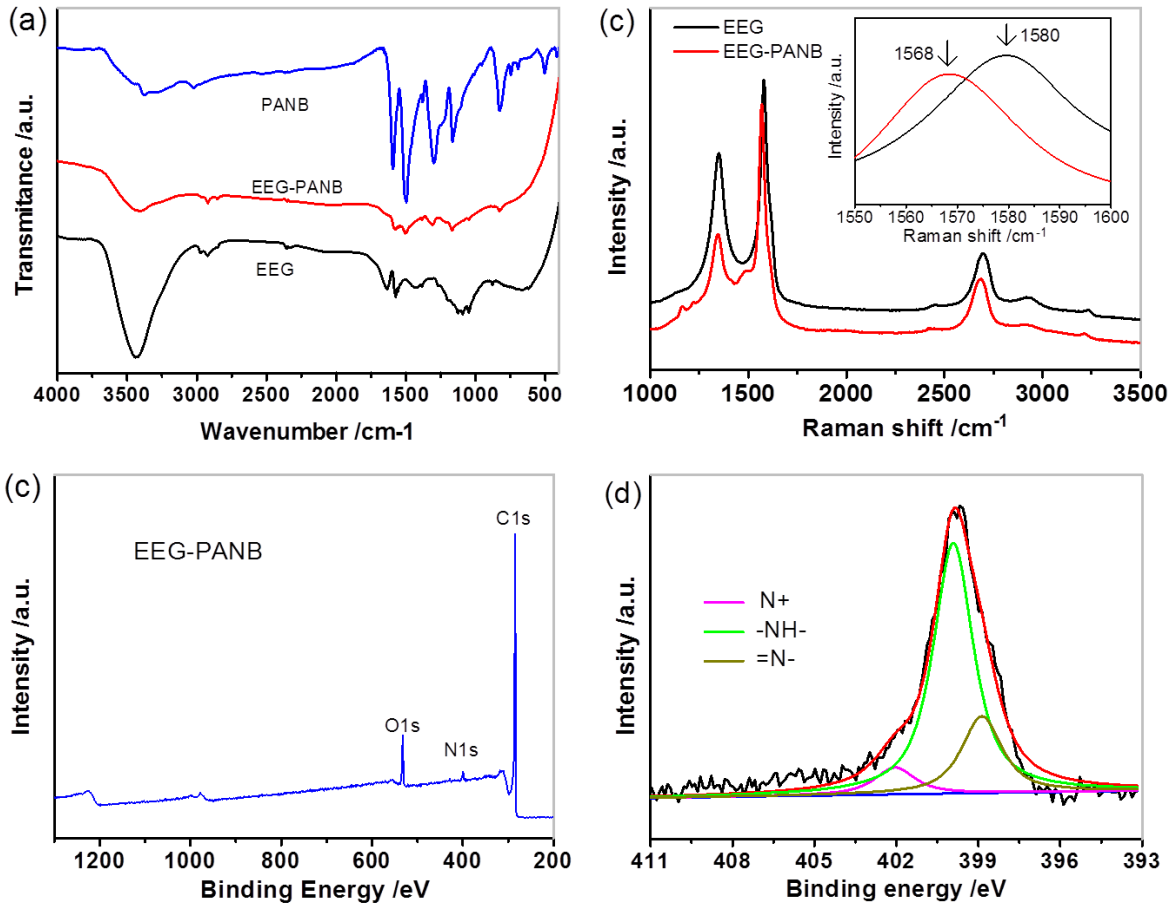

Figure 5.6 (a) FT-IR spectra of EEG, EEG-PANB and pure PANB; (b) Raman spectra of EEG-PANB; XPS spectra (c) and N1s XPS spectra (d) of EEG-PANB.

5.4.3 PANB loading amount

We found that the loading amount of PANB component is tuneable by simply adjusting the concentration of PANB/DMF solution. In a controlled experiment, EEG was functionalized in DMF solution with different PANB concentrations (0.5, 1 and 2 mg mL^{-1}) to produce EEG-PANB-X samples (X represents the concentration of PANB, mg mL^{-1}).

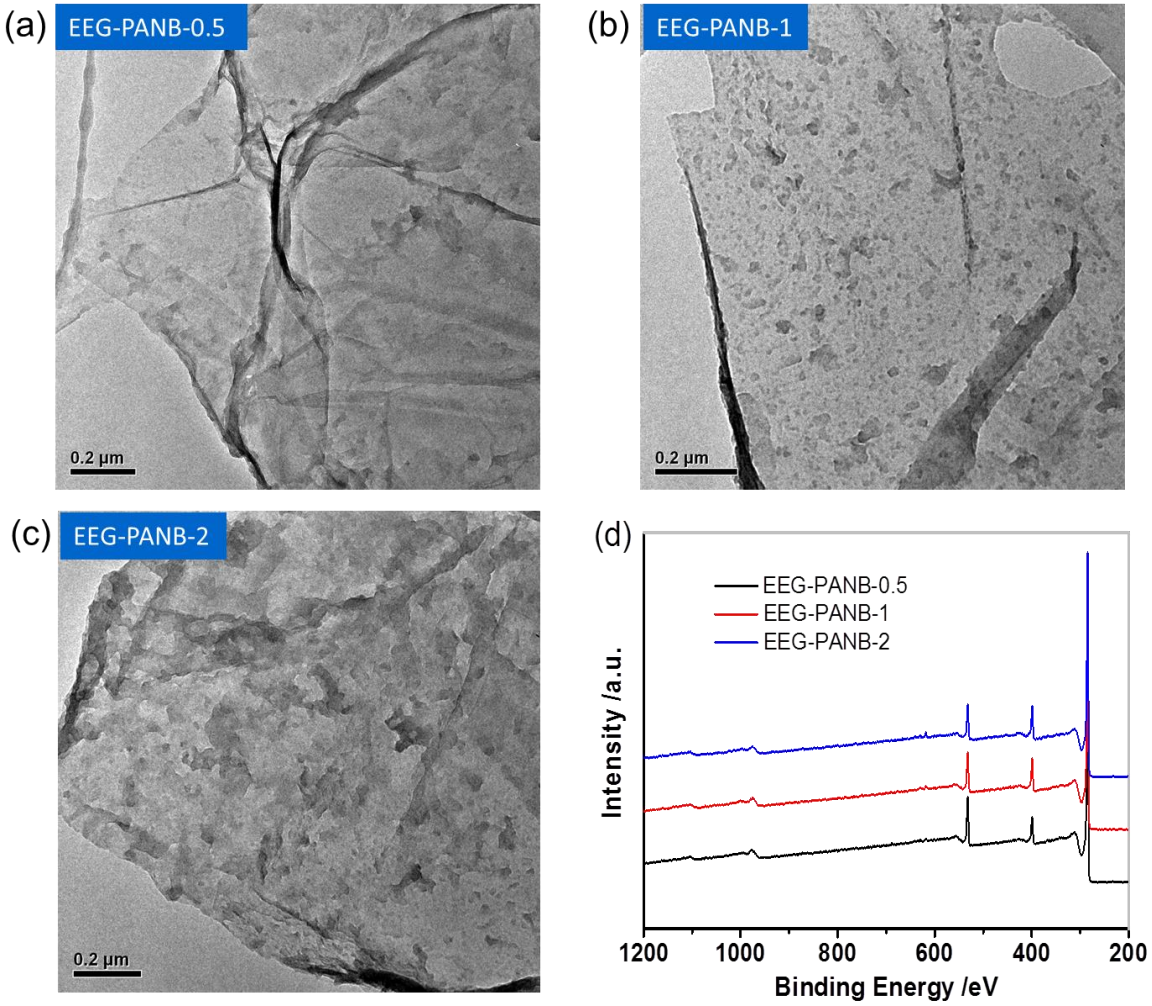

Figure 5.7 (a-c) TEM images of EEG-PANB-X samples. A significant PANB component in the solid state was detected on the EEG surface upon increasing the concentration of PANB/DMF solution (0.5-2 mg mL^{-1}) for EEG functionalization; (d) XPS spectra of EEG-PANB-X samples.

The morphology of EEG-PANB-X was characterized by TEM measurement. As shown in Figure 5.7a-c, a significant PANB component in the solid state was detected on the EEG surface upon increasing the concentration of PANB. At a high concentration of 2 mg mL^{-1}, the PANB molecules homogeneously deposited and formed a dense coating layer on EEG (Figure 5.7c). We then performed XPS measurements to identify the chemical compositions and the corresponding atomic content of all EEG-PANB-X samples (Figure 5.7d and Table 5.1). As expected, the nitrogen content significantly increased from 3.1 at.% for EEG-PANB-0.2 to 8.2 at.% for EEG-PANB-2, confirming an increased PANB loading amount on EEG-PANB nanosheets.

Table 5.1 Atomic content of EEG, EEG-PANB-X samples calculated from the XPS survey spectra.

Sample	C (at. ±0.5%)	O (at. ±0.5%)	N (at. ±0.5%)
EEG	86.8	13.2	------
EEG-PANB(-0.2)	88.9	8.0	3.1
EEG-PANB-0.5	87.1	6.6	6.3
EEG-PANB-1	86.7	5.7	7.6
EEG-PANB-2	86.8	5.0	8.2

5.4.4 Electronic property of EEG-PANS

Next, the electrical conductivity of EEG-PANB before and after protonic acid doping was examined. As the acid concentration plays an essential role for the degree of

protonation of PANB,[27, 28] EEG-PANB was treated with HCl with different concentrations (e.g. 0.1M, 0.5M and 1M) to produce EEG-emeraldine salt sheets (denoted as EEG-PANS-Y, where Y represents the HCl concentration). Figure 5.8 compares the resistance of EEG, EEG-PANB and EEG-PANS-Y film (R_f) obtained by the four-point probe method. The sample films (with an average thickness of 1μm) on SiO_2/Si substrates were prepared by a vacuum filtration and dry transfer method (see Experimental part). The EEG film exhibited an average R_f as low as 62.3 Ω sq^{-1}. After functionalization with PANB, the R_f of EEG-PANB substantially increased to 21.0 kΩ sq^{-1}. This can be attributed to the PANB barrier layers, resulting in a perturbed charge transport of EEG sheets. Remarkably, after protonation with HCl, the R_f of EEG-PANS-Y resumed reasonable levels. In particular, the

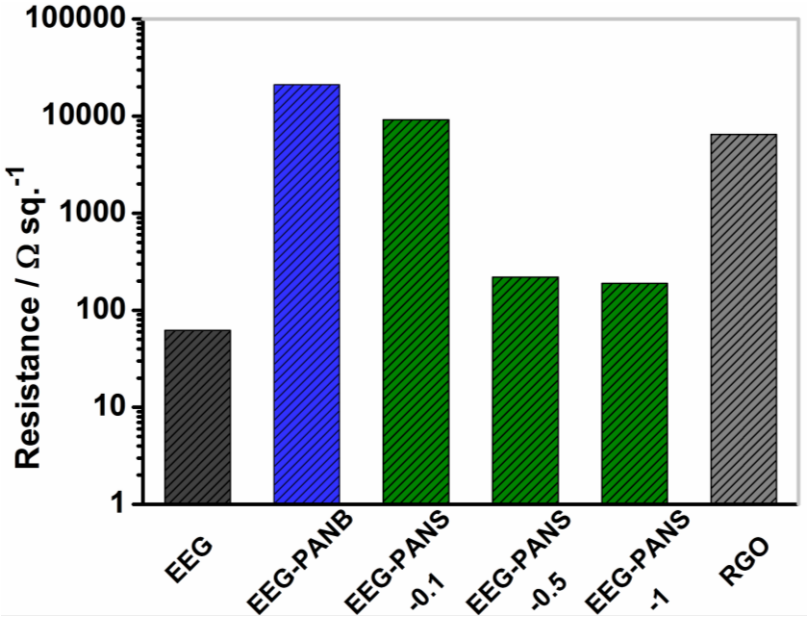

Figure 5.8 Resistance comparison of EEG, RGO, EEG-PANB before and after doping with HCl in various concentrations. The film resistance decreases with an increase of HCl concentration, indicative of enhanced protonation degree and successful restoration in conductivity of EEG-PANS-Y.

average R_f of EEG-PANS-Y dropped dramatically from 9.2 kΩ sq^{-1} to 189.4 Ω sq^{-1} as the HCl concentration increased from 0.1M to 1M. The average R_f between EEG-PANS-1 and RGO was also compared. The RGO was obtained by chemical reduction of GO with hydrazine in the aqueous ammonia solution. It is noteworthy that although EEG-PANS-1 exhibited a higher R_f compared to pristine EEG film, this value is still far below that of RGO film (6.5 kΩ sq^{-1}).

5.5 Characterization of EEG-nanoparticle hybrids

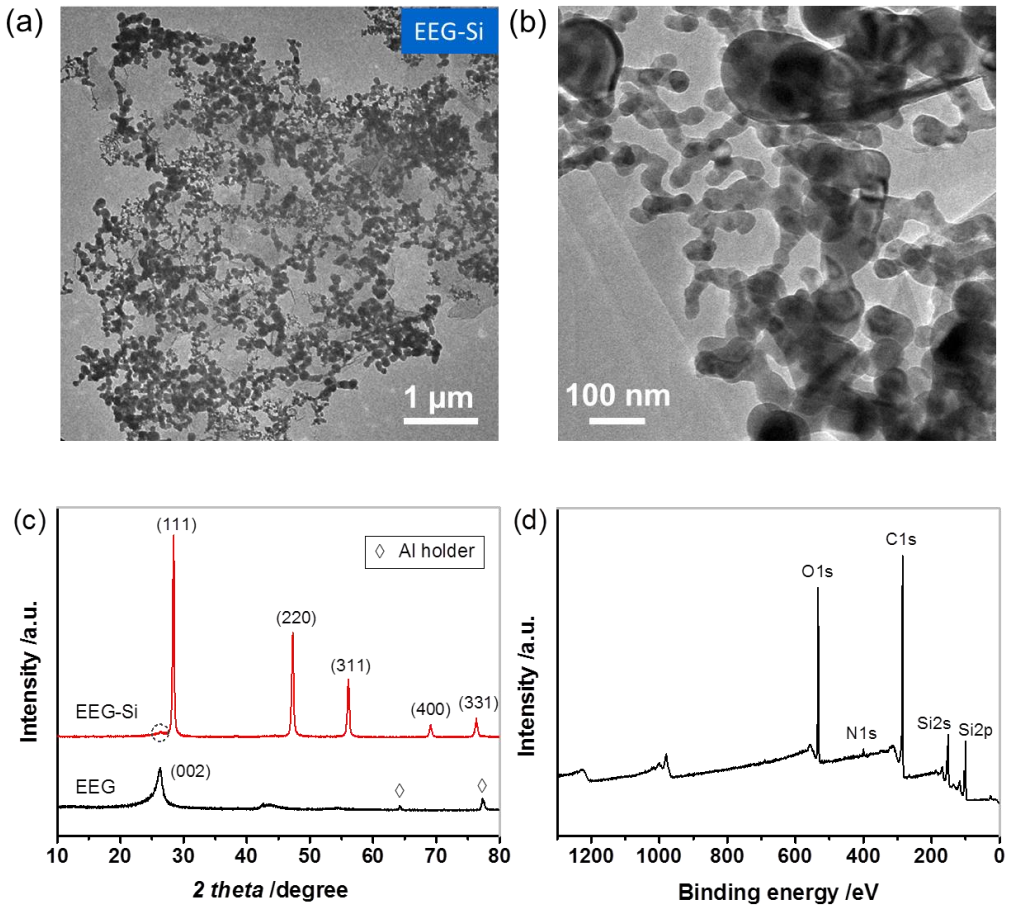

Figure 5.9 Typical TEM (a) and HR-TEM (b) image of EEG-Si hybrids; (c) XRD patterns of EEG and EEG-Si hybrids; (d) XPS spectra of EEG-Si hybrids.

Given that PANB affords abundant amine and imine groups on EEG basal planes, assembly of EEG-PANB with functional components is expected to produce EEG-based hybrid materials with defined nanostructure. For a typical example, EEG-Si sandwich-like hybrids were synthesized by co-assembly of EEG-PANB nanosheets and commercial Si NPs (with average particle size of ≤50 nm) in DMF solution. Si NPs possess a high content of hydroxyl groups around the surface SiO_2 layers, which facilitates binding of Si NPs on EEG-PANB via multiple interactions (e.g. electrostatic interaction, hydrogen-bonding). TEM and HR-TEM images (Figure 5.9a and b) verified the successful construction of EEG-Si. Notably, all Si NPs were homogeneously adhering to the EEG surface with no individual Si NPs observed from a large-scale TEM image. Both X-ray diffraction (XRD) and XPS measurement (Figure 5.9c and d) indicate the presence of the silicon component in the EEG-Si hybrids.[29] The diffraction hump appearing in the XRD pattern (at ~26.4°) is ascribed to the EEG substrates.

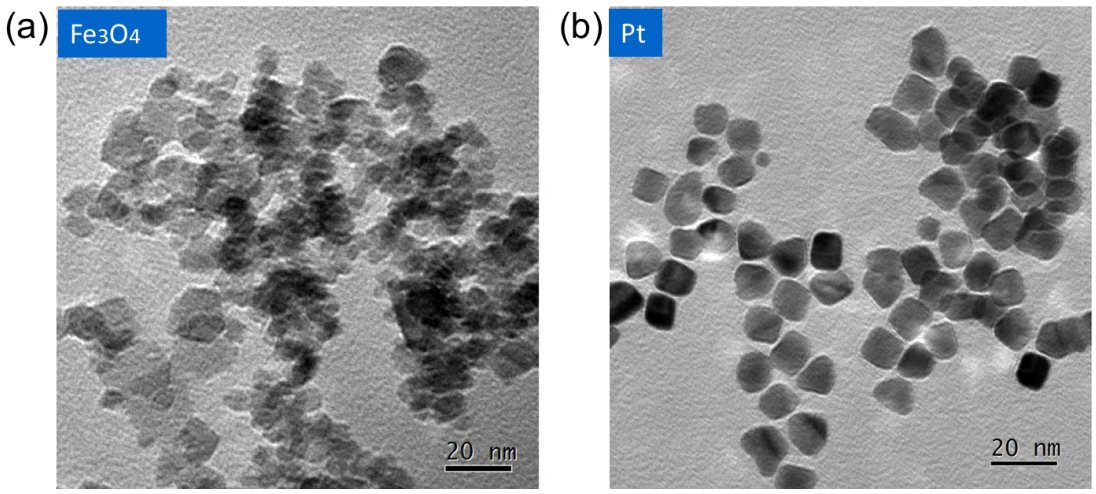

Figure 5.10 Representative TEM images of as-synthesized Fe_3O_4 (a) and Pt NPs (b).

Such a co-assembly protocol could be further extended to constructing other 2D EEG-CNPs hybrids by employing different functional CNPs such as Fe_3O_4 and Pt NPs. Monodispersed Fe_3O_4 and polyvinylpyrrolidone (PVP)-capped Pt NPs were synthesized

prior to assembly with EEG-PANB. TEM images show that as-synthesized Fe_3O_4 and Pt NPs have average particle sizes of ~10 and ~12 nm, respectively (Figure 5.10). TEM images of EEG-Fe_3O_4 and EEG-Pt demonstrate that in each case, the CNPs are uniformly decorated on the EEG surface, and no obvious CNPs are detected outside of the EEG sheets (Figure 5.11). Further, thermogravimetric analysis (TGA) of EEG-Si, EEG-Fe_3O_4 and EEG-Pt hybrids revealed that the weight fraction of Si, Fe_3O_4 and Pt NPs is 78%, 71% and 31%, respectively (Figure 5.12).

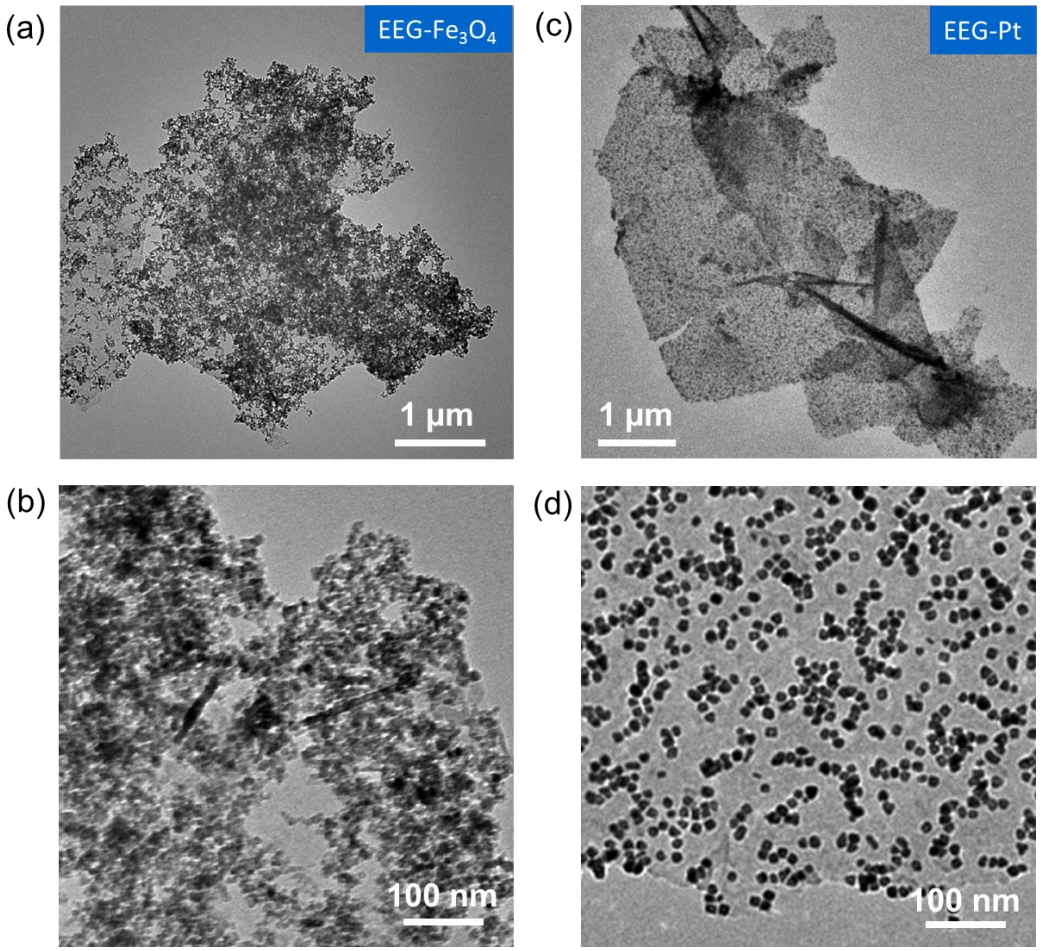

Figure 5.11 TEM and HR-TEM images of EEG-Fe_3O_4 (a, b) and EEG-Pt hybrids (c, d).

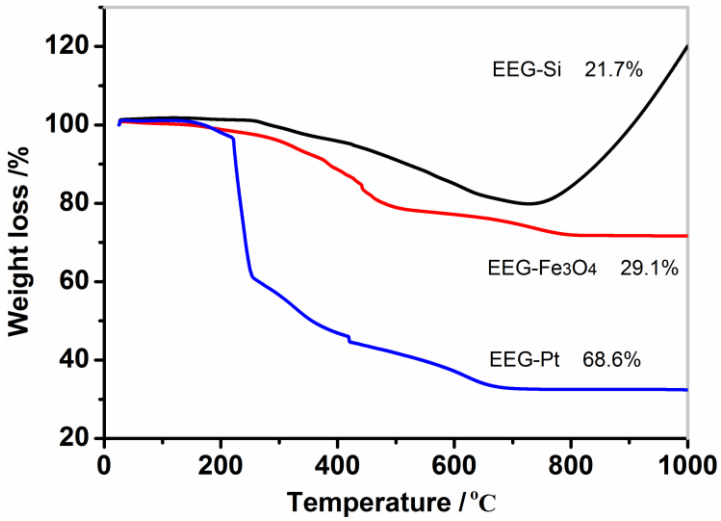

Figure 5.12 TGA curves of EEG-Si, EEG-Fe_3O_4 and EEG-Pt hybrids carried out in air with a heating rate of 10 °C min^{-1}.

5.6 Assembly mechanism

To determine the mode of interactions between EEG-PANB and Si NPs, the surface charges of Si NPs and EEG before and after functionalization with PANB were monitored by zeta potential (ζ) measurements (Figure 5.13a). Typically, EEG nanosheets and Si NPs are negatively charged in DMF solutions (ζ = –21.8 mV and –41.1 mV respectively). This result suggests that the formation of stable EEG/DMF dispersions can be partially attributed the electrostatic repulsion, similar to the colloidal behavior of GO in aqueous solution.[30] To simulate the assembly condition, we explored the surface charge of EEG-PANB in DMF solutions with various methanol volume fraction (V_m, 0–0.95). Herein, the methanol serves as a "soft" reagent to interact with EEG-PANB as the same functionality of hydroxyl groups on Si NPs surface. Figure 5.13b reveals that the surface charge of EEG-PANB switched from negative (ζ = –21.8 mV, V_m=0) to positive (ζ = 3.6 mV, V_m=0.05) and

increased linearly upon increasing V_m to 0.3 (ζ = 28.6). Further addition of methanol resulted in a slight increase of the ζ value. We surmise that as more hydroxyl groups were present in the dispersion (upon adding Si NPs or methanol), more imine nitrogen atoms in PANB chains were protonated, leading to an increase of positive charges on PANB chains and the EEG surface. Subsequently, the mutual assembly could be readily triggered when the positively charged EEG-PANB encountered negatively charged Si NPs.

Similarly, the Fe_3O_4 and Pt NPs are negatively charged as a result of ionization of the surface functional groups. It follows that the CNPs protonated imine side chains of PANB and subsequently assemble with EEG-PANB sheets. In the case of Pt NPs that stabilized by neutral capping ligands (PVP) with a low charge density (ζ = –9.0 mV), we assume that the interaction is primarily derived from the hydrogen bonding between PANB and PVP rather than the electrostatic interaction.[31]

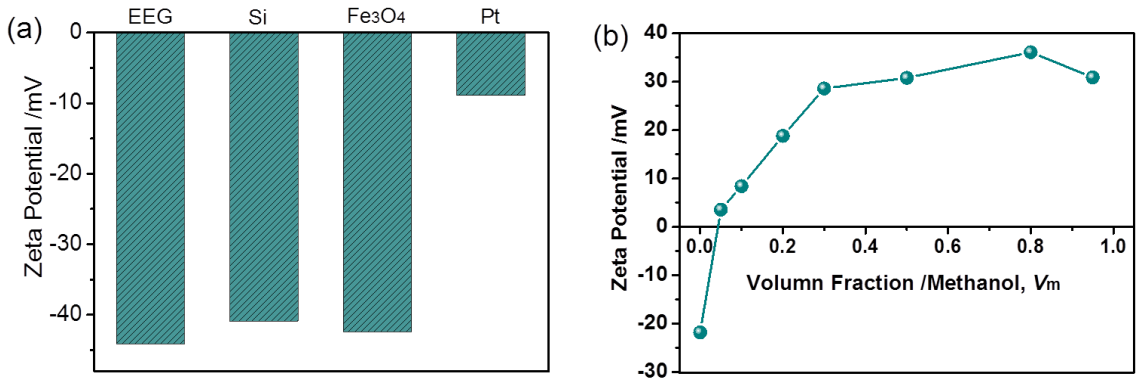

Figure 5.13 (a) Zeta potential measurement of EEG and various colloidal nanoparticles (including Si, Fe_3O_4, Pt); (b) Surface charge investigation of EEG-PANB in DMF solutions with different methanol volume fraction.

5.7 Electrochemical performance for lithium storage

Graphene-based hybrids hold promise as electrode materials for energy storage applications like lithium-ion batteries (LiBs).[32] Recently, design and fabrication of graphene/silicon anode materials attract particular attention owing to the combination of high-capacity Si active material (4200 mAh g^{-1}) and the unique graphene matrix.[33-35] Apart from improving electrical conductivity, graphene layers afford elastic buffering space to accommodate the volume change of Si during lithiation/delithiation process.[36] Silicon nanoparticles (Si NPs) represent the most investigated candidates for LiBs anode because of the mature synthetic technology and potential scalability.[37, 38] However, the conventional methods for preparing graphene/Si NPs hybrids involve direct mixing or filtration method and frequently fail in controlling the distribution/uniformity of Si NPs, thus leading to limited interfacial interactions between Si NPs and graphene.[39, 40] In this work, monodispersed Si NPs assembled with high-quality EEG and formed unique 2D sandwich-like structure, which may provide unique benefits towards lithium storage. To determine the effect of EEG on electrochemical performance, RGO-based Si hybrids (RGO-Si) was prepared for the purpose of comparison (see detailed procedure in the Experimental part).

5.7.1 Cycle stability

The electrochemical properties of EEG-Si hybrids were first examined by cyclic voltammetry (CV) measurements (Figure 5.14a). Similar to the pristine Si powders, the peak at 0.01 and 0.16 V in the cathodic process corresponds to the conversion of crystalline

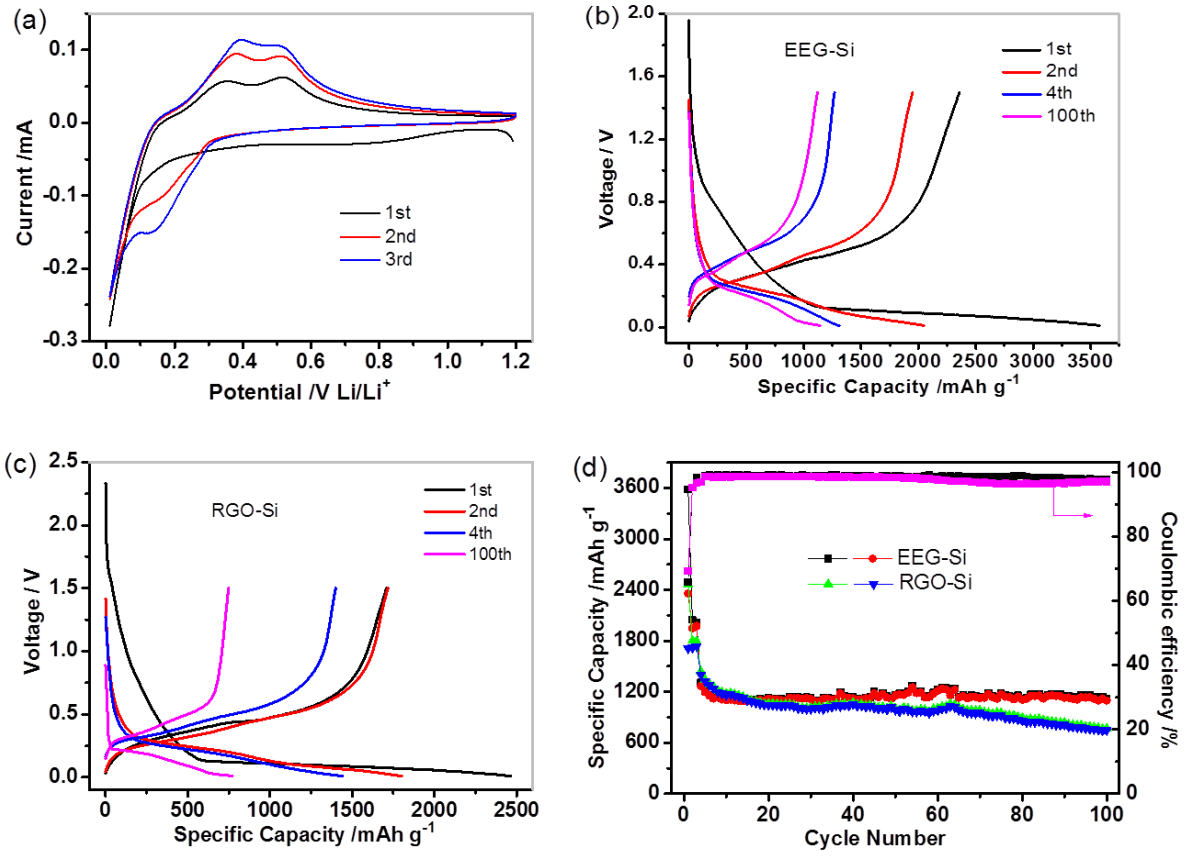

Figure 5.14 (a) Initial three cyclic voltammetry (CV) curves of EEG-Si at a scan rate of 0.1 mV s^{-1}; Galvanostatic cycling profiles of EEG-Si (b) and RGO-Si (c) hybrids for the 1st, 2nd, 4th and 100th cycle; (d) Cycling performance and Coulombic efficiency of EEG-Si and RGO-Si hybrids.

Si to the LixSi phase, while the two peaks at 0.35 and 0.52 V in the anodic process correspond to the delithiation of amorphous LixSi to Si.[41] The electrochemical cycling performance of EEG-Si and RGO-Si electrode was evaluated using discharge/charge galvanostatic cycling over the potential of 0.01-1.5V versus Li/Li^+. The capacity values reported here are based on the total weight of active material. As shown in Figure 5.14b and c, the EEG-Si electrode delivered a reversible capacity of 2357 and 2048 mAh g^{-1} in the first and second cycle at a current density of 105 and 210 mA g^{-1}, higher than that of RGO-

Si electrode (1709 and 1718 mAh g^{-1} respectively). On the basis of silicon mass ratio (78%) in EEG-Si hybrids, the capacity with respect to silicon is calculated to be 3022 and 2660 mAh g^{-1}. From the 4th cycle at a high current rate of ~1 A g^{-1}, the reversible capacity of both electrodes dropped. Remarkably, the EEG-Si electrode exhibits much better cycling performance in comparison to RGO-Si electrode (Figure 5.14d). After 100 cycles, the reversible capacity of EEG-Si is still as high as 1310 mAh g^{-1}, which corresponds to 86% capacity retention, while that of RGO-Si in only 748 mAh g^{-1} (capacity retention: 53%). Accordingly, higher Coulombic efficiency of EEG-Si (above 97% after initial three cycles) than that of RGO-Si was obtained.

5.7.2 Rate capability

Further, EEG-Si manifests superior rata capability in comparison to the RGO-Si electrode (Figure 5.15). As the current density increased from 0.42 to 4.2 A g^{-1}, the EEG-Si electrode displayed reversible and stable capacities of 1710 and 720 mAh g^{-1}. At a high current density of 8.4 A g^{-1}, EEG-Si electrode still delivered a favorable capacity of 460 mAh g^{-1}, while RGO-Si exhibited a capacity of 275 mAh g^{-1}.

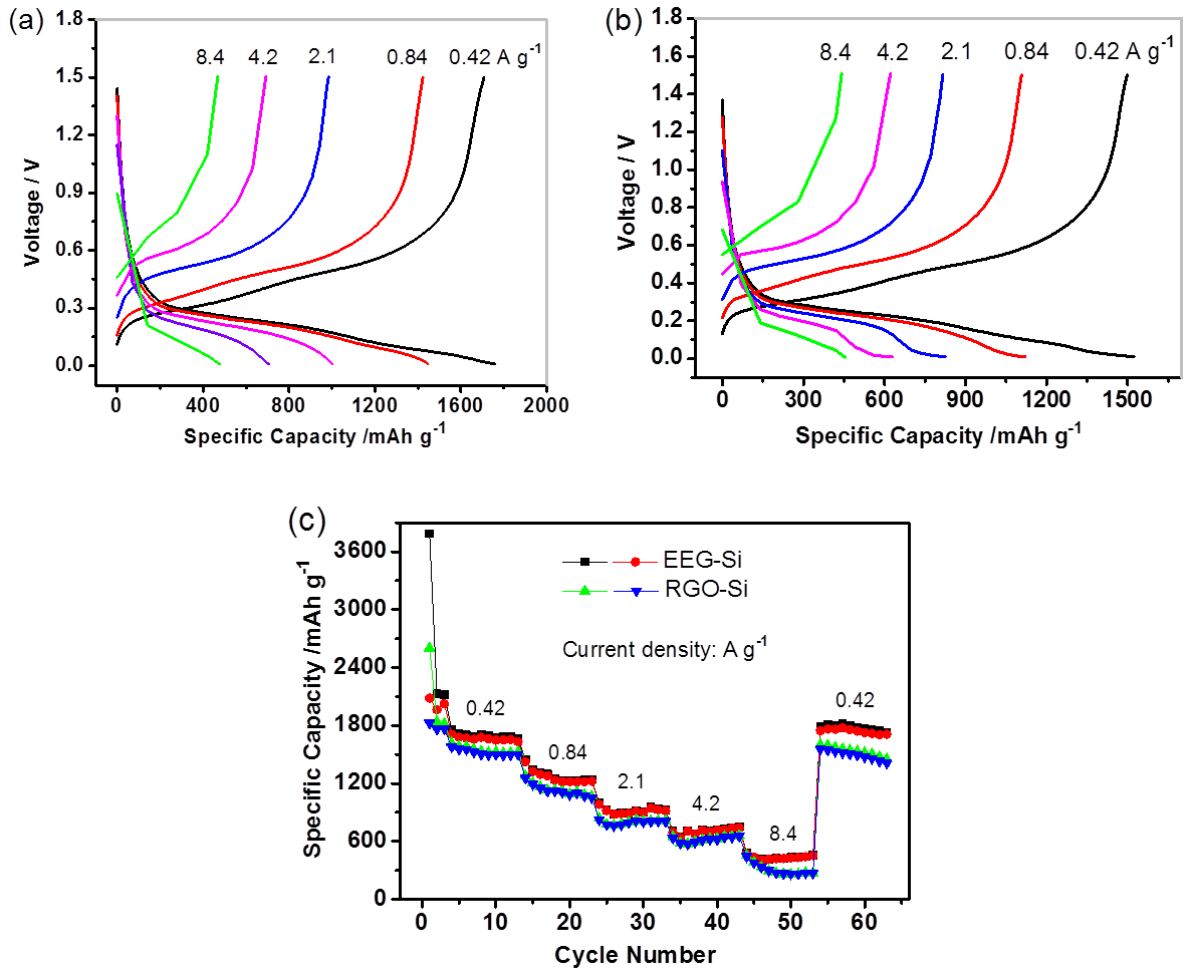

Figure 5.15 Galvanostatic cycling profiles of EEG-Si (a) and RGO-Si (b) hybrids at various current densities; (c) Rate capability of EEG-Si and RGO-Si electrodes. The current densities of initial three cycles for all electrodes are 105, 210, 210 mA g^{-1} respectively.

5.7.3 Effect of EEG

To verify the superior electrochemical performance of EEG-Si to RGO-Si, the structure and morphology of both electrodes after the 80th cycle were examined by scanning electron microscopy. As EEG-Si and RGO-Si were obtained by the same assembly procedure, the electrode materials show similar morphology with uniform

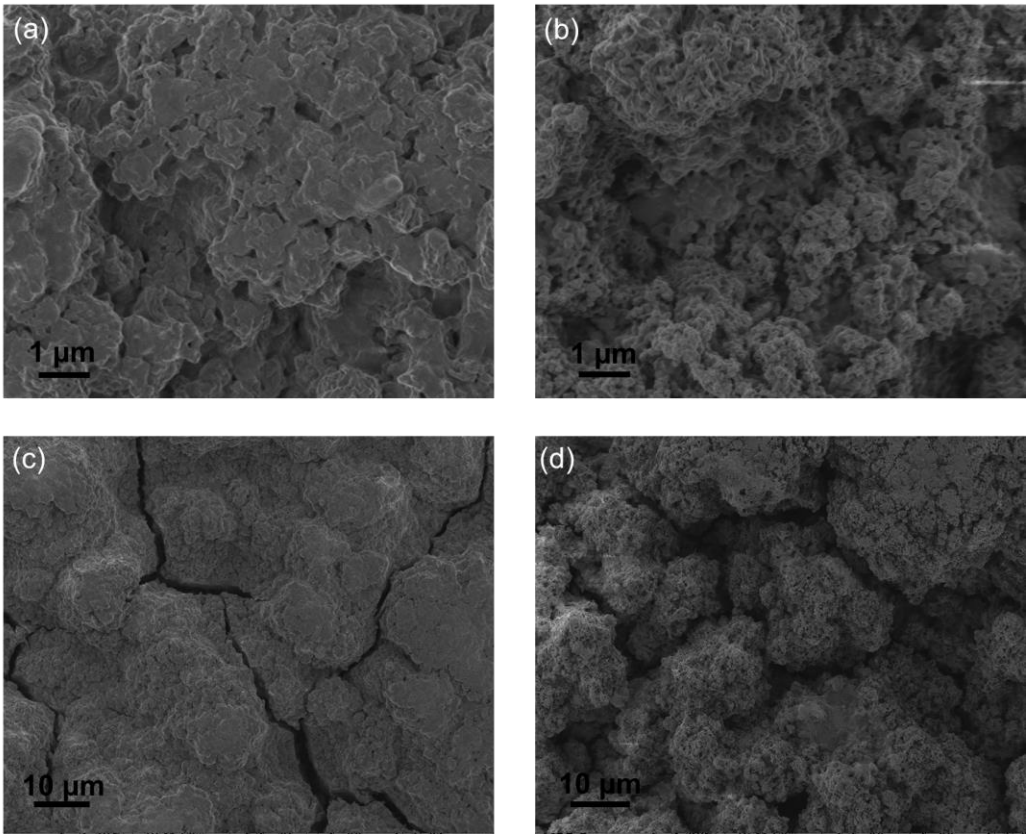

Figure 5.16 SEM images of EEG-Si and RGO-Si electrodes after 80 discharge/charge cycles.

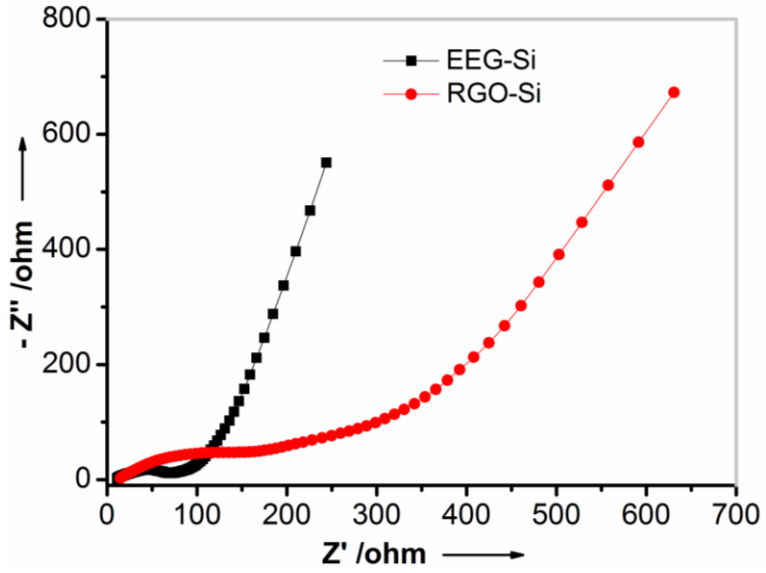

Figure 5.17 Nyquist plots of EEG-Si and RGO-Si electrodes after 80 discharge/charge cycles.

formation of solid-electrolyte interphase (SEI) on the hybrids (Figure 5.16a and b). SEM images at a large scale indicate that both electrode films exhibit cracks due to the extreme volume swing of Si active material (Figure 5.16c and d). Notably, RGO-Si electrode film underwent severe cracking and disassembly of active materials compared to that of EEG-Si electrode, which led to loss of electrical contact and eventual fading of capacity. This comparative result indicates that the EEG nanosheets with higher mechanical strength and chemical stability can better withstand the stress buildup within Si anode in comparison with RGO. This stabilizing effect of EEG substrates was confirmed by electrochemical impedance spectroscopy (EIS) measurement. Nyquist plots (Figure 5.17) show that the diameter of the semicircle for the EEG-Si electrode in the high–medium frequency region is much smaller than that of RGO-Si, indicating lower contact and charge-transfer impedances of EEG-Si compared with RGO-Si electrode.

We attribute the exceptional electrochemical cycling and rate performance of EEG-Si to the assembled architecture and high quality of EEG matrix. First, monodispersed Si NPs are integrated with EEG nanosheets via controlled assembly approach. The conformal contact between EEG sheets and individual Si NP is beneficial to stabilize Si NPs fracture during electrochemical reactions; second, adequate free space between Si NPs is retained on EEG surface as depicted by TEM image, which allow for efficient volume accommodation of Si NPs during lithium insertion; third, the EEG nanosheets provides robust matrix to accommodate the strain and retain structural integrity of Si hybrids electrode.

5.8 Conclusion

In this Chapter, a synthetic concept utilizing electrochemically exfoliated graphene (EEG) that assembled colloidal nanoparticles (CNPs) into 2D nanohybrids was investigated in an attempt to promote structural control and potential applications of EEG. Polyaniline in the emeraldine base (PANB) form was used as a powerful dopant for the functionalization of EEG and the controlled assembly with functional CNPs. We found that the association of electrostatic interaction and hydrogen bonding qualified PANB as a versatile "bridge" binding the CNPs to the EEG surface. This synthetic method is distinctive in its use of low-cost ingredients, ease in processing, applicability to other EEG materials with complex morphology for multiple end-uses.

5.9 References

[1] X. Huang, C. Tan, Z. Yin, H. Zhang, *Adv. Mater.* **2014**, *26*, 2185.

[2] W. Wei, H. Liang, K. Parvez, X. Zhuang, X. Feng, K. Müllen, *Angew. Chem. Int. Ed.* **2014**, *53*, 1570.

[3] S. H. Lee, D. H. Lee, W. J. Lee, S. O. Kim, *Adv. Funct. Mater.* **2011**, *21*, 1338.

[4] L. Yan, Y. B. Zheng, F. Zhao, S. Li, X. Gao, B. Xu, P. S. Weiss, Y. Zhao, *Chem. Soc. Rev.* **2012**, *41*, 97.

[5] D. R. Dreyer, S. Park, C. W. Bielawski, R. S. Ruoff, *Chem. Soc. Rev.* **2010**, *39*, 228.

[6] H. Wang, H. S. Casalongue, Y. Liang, H. Dai, *J. Am. Chem. Soc.* **2010**, *132*, 7472.

[7] Q. Su, S. Pang, V. Alijani, C. Li, X. Feng, K. Müllen, *Adv. Mater.* **2009**, *21*, 3191.

[8] Y. Xu, K. Sheng, C. Li, G. Shi, *ACS Nano* **2010**, *4*, 4324.

[9] Y. Su, S. Li, D. Wu, F. Zhang, H. Liang, P. Gao, C. Cheng, X. Feng, *ACS Nano* **2012**, *6*, 8349.

[10] Y. L. Zhong, T. M. Swager, *J. Am. Chem. Soc.* **2012**, *134*, 17896.

[11] J. Wang, K. K. Manga, Q. Bao, K. P. Loh, *J. Am. Chem. Soc.* **2011**, *133*, 8888.

[12] N. Liu, F. Luo, H. Wu, Y. Liu, C. Zhang, J. Chen, *Adv. Funct. Mater.* **2008**, *18*, 1518.

[13] K. Parvez, R. Li, S. R. Puniredd, Y. Hernandez, F. Hinkel, S. Wang, X. Feng, K. Müllen, *ACS Nano* **2013**, *7*, 3598.

[14] K. Parvez, Z.-S. Wu, R. Li, X. Liu, R. Graf, X. Feng, K. Müllen, *J. Am. Chem. Soc.* **2014**, *136*, 6083.

[15] K. S. Rao, J. Senthilnathan, Y.-F. Liu, M. Yoshimura, *Sci. Rep.* **2014**, *4*.

[16] G. Wang, B. Wang, J. Park, Y. Wang, B. Sun, J. Yao, *Carbon* **2009**, *47*, 3242.

[17] RamanathanT, A. A. Abdala, StankovichS, D. A. Dikin, M. Herrera Alonso, R. D. Piner, D. H. Adamson, H. C. Schniepp, ChenX, R. S. Ruoff, S. T. Nguyen, I. A. Aksay, R. K. Prud'Homme, L. C. Brinson, *Nat. Nanotechnol.* **2008**, *3*, 327.

[18] S. Stankovich, D. A. Dikin, G. H. B. Dommett, K. M. Kohlhaas, E. J. Zimney, E. A. Stach, R. D. Piner, S. T. Nguyen, R. S. Ruoff, *Nature* **2006**, *442*, 282.

[19] S. Stankovich, R. D. Piner, X. Chen, N. Wu, S. T. Nguyen, R. S. Ruoff, *J. Mater. Chem.* **2006**, *16*, 155.

[20] V. López, R. S. Sundaram, C. Gómez-Navarro, D. Olea, M. Burghard, J. Gómez-Herrero, F. Zamora, K. Kern, *Adv. Mater.* **2009**, *21*, 4683.

[21] C. Mattevi, G. Eda, S. Agnoli, S. Miller, K. A. Mkhoyan, O. Celik, D. Mastrogiovanni, G. Granozzi, E. Garfunkel, M. Chhowalla, *Adv. Funct. Mater.* **2009**, *19*, 2577.

[22] A. G. MacDiarmid, *Angew. Chem. Int. Ed.* **2001**, *40*, 2581.

[23] A. Pron, P. Rannou, *Prog. Polym. Sci.* **2002**, *27*, 135.

[24] D. Kim, J. Choi, J.-Y. Kim, Y.-K. Han, D. Sohn, *Macromolecules* **2002**, *35*, 5314.

[25] D.-W. Wang, F. Li, J. Zhao, W. Ren, Z.-G. Chen, J. Tan, Z.-S. Wu, I. Gentle, G. Q. Lu, H.-M. Cheng, *ACS Nano* **2009**, *3*, 1745.

[26] K. L. Tan, B. T. G. Tan, E. T. Kang, K. G. Neoh, *Phys. Rev. B* **1989**, *39*, 8070.

[27] A. MacDiarmid, J. Chiang, A. Richter, A. Epstein, *Synth. Met.* **1987**, *18*, 285.

[28] J.-C. Chiang, A. G. MacDiarmid, *Synth. Met.* **1986**, *13*, 193.

[29] N. Liu, H. Wu, M. T. McDowell, Y. Yao, C. Wang, Y. Cui, *Nano Lett.* **2012**, *12*, 3315.

[30] D. Li, M. B. Müller, S. Gilje, R. B. Kaner, G. G. Wallace, *Nat. Nanotechnol.* **2008**, *3*, 101.

[31] R. Cruz-Silva, L. Arizmendi, M. Del-Angel, J. Romero-Garcia, *Langmuir* **2006**, *23*, 8.

[32] X. Huang, X. Qi, F. Boey, H. Zhang, *Chem. Soc. Rev.* **2012**, *41*, 666.

[33] J. Ji, H. Ji, L. L. Zhang, X. Zhao, X. Bai, X. Fan, F. Zhang, R. S. Ruoff, *Adv. Mater.* **2013**, *25*, 4673.

[34] K. Evanoff, A. Magasinski, J. Yang, G. Yushin, *Adv. Energy Mater.* **2011**, *1*, 495.

[35] X. Zhou, Y. X. Yin, L. J. Wan, Y. G. Guo, *Adv. Energy Mater.* **2012**, *2*, 1086.

[36] F. Zhang, X. Yang, Y. Xie, N. Yi, Y. Huang, Y. Chen, *Carbon* **2015**, *82*, 161.

[37] N. Liu, Z. Lu, J. Zhao, M. T. McDowell, H.-W. Lee, W. Zhao, Y. Cui, *Nat. Nanotechnol.* **2014**, *9*, 187.

[38] H. Wu, G. Yu, L. Pan, N. Liu, M. T. McDowell, Z. Bao, Y. Cui, *Nat. Commun.* **2013**, *4*.

[39] X. Zhou, Y.-X. Yin, L.-J. Wan, Y.-G. Guo, *Chem. Commun.* **2012**, *48*, 2198.

[40] J. K. Lee, K. B. Smith, C. M. Hayner, H. H. Kung, *Chem. Commun.* **2010**, *46*, 2025.

[41] A. Magasinski, P. Dixon, B. Hertzberg, A. Kvit, J. Ayala, G. Yushin, *Nat. Mater.* **2010**, *9*, 353.

Chapter 6 Conclusion and Outlook

6.1 Conclusion

In conclusion, this PhD work focuses on the controllable assembly of graphene and various functional components (inorganic or carbon components) to produce hybrid materials with well-defined structures as well as their applications for energy storage and conversion systems (ESCSs). Graphene-based hybrid materials (GHMs) with diverse morphology, such as core-shell, two-dimensional (2D) sandwich-like/porous nanosheets and three-dimensional (3D) macroporous foams, were designed and fabricated to meet the requirements of specific energy applications. Typically, three ESCSs including lithium-ion batteries (LiBs), supercapacitores (SCs) and fuel cells (FCs) have been employed to evaluate the advantages of GHMs with well-defined nanostructures compared to those physically mixed or commercial ones. It is noteworthy that in the end of this thesis, great advances for GHM assembly were achieved by replacing conventional graphene oxide (GO) building blocks with high-quality electrochemically exfoliated graphene (EEG). It thus opens up a unique opportunity for the large-scale production of new GHMs for a broad range of applications.

LiBs are by far the most common energy storage devices. Compared to commercial graphite anode (theoretical capacity: 372 mAh g^{-1}), silicon and metal oxides (e.g. Fe_3O_4) are promising anode candidates for high-energy LiBs and devices (e.g. electric vehicles) due to their higher storage capacity and energy density.[1] Unfortunately, these electrode materials cannot be used in their bulk/pristine form as a result of the extreme structural degradation during lithiation/delithiation process. In the first subject of this thesis, a cost-

effective method for the fabrication of 3D graphene foam hybrids was developed to strengthen the structural integrity and electrochemical performance of active materials. Specifically, Fe_3O_4 nanospheres (with a diameter of ~200 nm) were encapsulated with graphene sheets via electrostatic interactions and further confined within continuous graphene frameworks by hydrothermal assembly procedure. Such hierarchical porous structures afforded sufficient free space and constant mechanical support to accommodate the volume expansion of Fe_3O_4. The different structural features among graphene/Fe_3O_4 hybrids exerted a significant influence on their electrochemical performance, which was elucidated by the galvanostatic discharge/charge and TEM measurement. Notably, electrodes with a core-shells structure (Fe_3O_4@GS) deteriorated within several tens of cycles due to the extremely large volumetric change, and gave a low reversible capacity of 614 mAh g^{-1} after 80 cycles. In contrast, hierarchical graphene foam hybrids (Fe_3O_4@GS/GF), provided complementary strengthening of graphene shells and core Fe_3O_4 nanospheres, thus achieved a highly reversible capacity of 1059 mAh g^{-1} over 150 cycles and excellent rate capability.

Specific surface area and pore structure serve as the key to optimize GHMs properties for SCs applications. A critical challenge for preparing porous GHMs is to counter the stacking behavior of graphene sheets and obtain highly accessible surface areas and pores. Towards this end, graphene-based carbon nanosheets with highly mesoporous carbon shells (HPCN) were presented in Chapter 3. The uniform mesopores were derived from a hierarchical graphene/silica template that was built up by in-situ growth of silica layers and electrostatic assembly of colloidal silica nanoparticles on graphene oxide. Sucrose was employed as carbon precursor to generate HPCN via a simple nanocasting technology. We found that the porosity configurations of GHMs had a significant impact on both

physicochemical properties and electrochemical performance for SCs. Remarkably, HPCN possessed regular mesopore distribution (pore size: ~12nm), high specific surface area (1273 m^2 g^{-1}) and large pore volume (2.64 cm^3 g^{-1}), and eventually led to an outstanding specific capacitance (222 F g^{-1}) and high rate capability for electrochemical double-layer capacitors. In contrast, porous carbon nanosheets (PCNs) prepared via conversional physically mixing/pyrolysis method gave a lower specific surface area (910 m^2 g^{-1}) and capacitance (157 F g^{-1}). Moreover, HPCN could serve as robust carbon matrix for accommodating metal oxide (RuO_2) for application in pseudocapacitors.

Porous GHMs doped with heteroatoms are attractive catalyst targets for efficient oxygen reduction reaction (ORR) in FCs. However, the ORR performance of reported metal-free GHMs is generally poor in both alkaline and acidic media compared to commercial Pt/C, primarily due to the low density of surface active sites. In Chapter 4, we described a novel approach to fabricate nitrogen-doped carbon nanosheets (NDCNs) with size-defined mesopores towards highly efficient ORR. The typical synthesis protocol involved the employment of hierarchical graphene/silica nanosheets (as developed in Chapter 3) as template and dopamine as nitrogen-rich precursor. Spontaneous coating of polydopamine layer followed by pyrolysis and etching of the silica template yielded NDCN with exposed highly electroactive and stable catalytic sites. Besides the regular mesoporous features, the pores size of NDCN could be precisely tailored in this work by selection of the colloidal silica template with different particle sizes. This synthetic protocol towards mesoporosity control appeared to modulate the active sites and boosted the electrocatalytic activity of metal-free carbonaceous catalysts. Notably, NDCN catalyst with mesopore size of 22 nm (NDCN-22) displayed high current density, almost four electron transfer process and lower onset potential (-0.01V *vs* Ag/AgCl) than that of commercial Pt/C catalyst (-

0.02V) in alkaline conditions. Moreover, the NDCN-22 catalyst exhibited pronounced catalytic behavior with positive onset potential and low H_2O_2 yield in acidic conditions.

In previous chapters, significant progress on the controllable assembly of GHMs and their application for ESCSs has been achieved using GO as basic building blocks. It should be emphasized that the intrinsic bottleneck of GO or RGO is the poor quality and high cost, which hinder the mass production of high-performance GHMs for energy applications. Electrochemical exfoliation methods have been recently developed to obtain high quality graphene (EEG) in bulk-scale.[2] However, the poor solution-processability and inert surface properties of EEG constitute the major drawbacks for utilization of EEG in material synthesis. To overcome these intrinsic limitations, we demonstrated a rational and facile protocol for surface functionalization of EEG and controlled assembly of EEG-based hybrid materials in Chapter 5. Particularly, polyaniline (PANI), in the Emeraldine base form (PANB), was employed as a bi-functional linker to bridge the counterparts of EEG nanosheets and various inorganic functional nanoparticles. The backbone rings of PANB spontaneously adsorbed on EEG surface via π-π interactions, whereas the exposed amine/imine groups served as numerous active sites to interact with CNPs surface via electrostatic force and hydrogen bonding. For the first time, we combine the solution-processable EEG and PANI to build up 2D EEG hybrids in a controlled assembly manner, such as EEG-Si, EEG-Fe_3O_4 and EEG-Pt. The resultant EEG hybrids hold great promise for a variety of possible applications like lithium storage. As exemplified by EEG-Si hybrids serving as anode material for LiBs, a high initial reversible capacity (2357 mAh g^{-1} at 105 mA g^{-1}) and excellent cycling stability (86% capacity retention after 100 cycles at 1 A g^{-1}) were achieved.

6.2 Outlook

The studies described in this thesis contribute to a deeper insight into the functionalization of graphene and self-assembly of graphene-based hybrid materials (GHMs). Moreover, this work is helpful for understanding the relationships between microstructure/macroproperties of GHMs and their device performance in energy storage and conversion applications. Nevertheless, there remains a long way to achieve practical applications of various GHMs.

For lithium storage materials, combination of graphene shells and 3D graphene frameworks is a feasible and promising strategy to buffer the volume change of active components and improve electrochemical performance of the electrode. However, there are still some obstacles of this protocol. For instance, active components with reduced particle size (e.g. <100 nm) cannot be perfectly encapsulated and interconnected by graphene via the self-assembly process. In contrast, the active particles tend to randomly attach to the graphene surface and give rise to lots of bare surface exposed to the electrolyte.[3] This might be improved by pre-coating active particles with carbon shell (or carbon precursors) before confinement within graphene networks in the future. Another obstacle is that the as-constructed monolithic hybrids have to be broken into pieces for electrode preparation as measured for traditional powder samples. Therefore, from a practical point of view, assembly GHMs with tunable bulk shape (like films, papers, and fibers) towards final device application is also necessary.

The performance of GHMs for supercapaticors (SCs) and oxygen reduction reaction (ORR) largely depends on their porosity characteristics, including specific surface area, pore structure and pore size distribution. For SCs applications, a carbonaceous electrode

containing large amounts of micropores is currently believed to be ideal due to the actual energy storage occurring predominately in the micropores where the bulk of the surface area lies.[4] Therefore, it is of great importance to fabricate GHMs via soft-template methods (small organic molecules or block polymers as soft templates) to increase the surface area through the introduction of ordered/periodic micropores. Further, an additional activation process (by activation agents, like NH_3, CO_2, KOH) [5] can also be used to increase the fraction of micropores on the total surface area of carbonaceous materials. It has been revealed that integration of macropores with micro-/mesopores is favorable for buffering ions and increasing the charge accommodation within the electrodes.[6] Therefore, to increase the capacity and power density, GHMs can be further optimized by building up hierarchical porous structure that span the micropore to macropore range while maintaining the predominant micro-/mesopore domains.

Further, mesoporosity control associated with nitrogen doping appears to boost the ORR activity of carbonaceous catalysts. However, the performance of metal-free GHMs for fuel cell applications is still poor when operated in acidic condition. Beyond the scope of this topic to tailor mesopore size and promote exposure of active sites, several issues need to be addressed for further development of graphene-based ORR catalysts such as: (1) synthesize dual-/multi-heteroatom (such as N, S, B and P) doped graphene materials to optimize the intrinsic catalytic nature of metal-free catalysts. This is due to the fact that the synergistic effect between the dopants might result in redistribution of charge densities in carbon atoms, and thereby generate a large number of active sites;[7] (2) it has been suggested that the nitrogen in either graphitic or pyridinic form participates in the active sites and contributes to the ORR performance.[8] Therefore, to enrich the catalytic activity, GHMs with optimal amount and types of nitrogen needs to be synthesized. This can be

achieved by selecting different nitrogen-containing polymeric (e.g. polyaniline and polypyrrole) or organic precursors; (3) incorporate transition metal components (e.g. Fe, Co) into nitrogen-doped carbon frameworks to improve the ORR activity by creating metal-N_x active sites;[9] (4) fundamental study of the ORR catalytic mechanism on either metal-free or nonprecious metal catalyst is essential prior to design and development of graphene catalysts with desirable activity and durability; (5) for industrial application purposes, the performance evaluation of all developed GHMs catalysts in actual fuel cells should be performed.

Electrochemically exfoliated graphene (EEG), which features high quality, environmental acceptability, and scalable production potential, has emerged as promising candidate for fabrication of GHMs. In the end of this thesis, we reported a new method to assemble series of colloidal functional nanoparticles onto EEG surfaces with the aid of polyaniline (PANI) as the linker. Nevertheless, both functionalization of EEG and assembly of EEG hybrids are still at their infant stage. More efforts beyond this approach should be devoted to the construction of EEG hybrids with desired morphology and properties. First, the high solution-processability of EEG is regarded as key to achieve dispersion phase assembly with different functional components. However, owing to the superhydrophobic nature, EEG is unable to disperse in most solvents, which limits the use of conventional assembly techniques (such as layer by layer, solvent-evaporation, sol-gel, hydrothermal etc.) for fabricating EEG hybrids. Thereby, functionalization of EEG which allows for bulk-scale processing and assembly of EEG in nontoxic and low boiling point solvents would be necessary; Moreover, despite the selection of a conducting polymer (PANI) as functional component in this study, the PANI-functionalized EEG presents a lower electric conductivity compared to that of pristine EEG. Therefore, careful selection of functional

components (like small organic molecules) which can be readily removed at the end is highly desirable; Last but not least, GHMs based on EEG remain a less explored area. There is great potential for using EEG in the development of novel electronic/energy devices, such as transparent/flexible electrodes, all-solid-state lithium-ion batteries/supercapacitors.

6.3 References

[1] C. K. Chan, H. Peng, G. Liu, K. McIlwrath, X. F. Zhang, R. A. Huggins, Y. Cui, *Nat. Nanotechnol.* **2008**, *3*, 31.

[2] K. Parvez, Z.-S. Wu, R. Li, X. Liu, R. Graf, X. Feng, K. Müllen, *J. Am. Chem. Soc.* **2014**, *136*, 6083.

[3] X. Li, X. Huang, D. Liu, X. Wang, S. Song, L. Zhou, H. Zhang, *J. Phys. Chem. C* **2011**, *115*, 21567.

[4] Y. Zhai, Y. Dou, D. Zhao, P. F. Fulvio, R. T. Mayes, S. Dai, *Adv. Mater.* **2011**, *23*, 4828.

[5] Y. Zhu, S. Murali, M. D. Stoller, K. J. Ganesh, W. Cai, P. J. Ferreira, A. Pirkle, R. M. Wallace, K. A. Cychosz, M. Thommes, D. Su, E. A. Stach, R. S. Ruoff, *Science* **2011**, *332*, 1537.

[6] Z.-S. Wu, Y. Sun, Y.-Z. Tan, S. Yang, X. Feng, K. Müllen, *J. Am. Chem. Soc.* **2012**, *134*, 19532.

[7] J. Liang, Y. Jiao, M. Jaroniec, S. Z. Qiao, *Angew. Chem. Int. Ed.* **2012**, *51*, 11496.

[8] H.-W Liang, W. Wei, Z.-S. Wu, X. Feng, K. Müllen, *J. Am. Chem. Soc.* **2013**, *135*, 16002.

[9] G. Wu, K. L. More, C. M. Johnston, P. Zelenay, *Science* **2011**, *332*, 443.

Chapter 7 Experimental Part

7.1 Fabrication of Fe_3O_4/graphene foam (Chapter 2)

7.1.1 Synthesis of graphene oxide and reduced graphene oxide

Graphene oxide (GO) was prepared according to the Hummer's method.[1] In a typical procedure, natural graphite flakes (10 g, Aldrich) and $NaNO_3$ (7.5 g) were added into concentrated H_2SO_4 (300 mL) under stirring. After 5 min, $KMnO_4$ (40 g) was slowly added to the reaction mixture over 1 hour. The mixture was stirred at room temperature for 3 days. Afterwards, 1 L of H_2O_2 solution (1 % in water) was added to the dark brown paste. The resulting suspension was then centrifuged at 4,000 rpm for 10 minutes to remove unreacted graphite flakes. After removal of large graphite flakes, the dark brown dispersion was subjected to dialysis for 2 weeks to remove residual salts and acids until the pH of the dispersion reached 7.0. Exfoliation was carried out by sonicating the as-prepared black solid in an ice bath. The concentration of the GO dispersion was determined by vacuum drying and measuring the weight of a small volume of the as-prepared GO dispersion. The resulting homogeneous brown dispersion was stable for several months and was used for fabrication of graphene-based hybrid materials.

GO was reduced by hydrazine in the presence of ammonia.[2] In a typical experiment, as-synthesized GO dispersion was first diluted with water to a concentration of 0.2 mg ml^{-1}. Ammonia solution (28 wt% in water) was added to the GO dispersion to increase the pH to ~10. Next, a hydrazine solution (N_2H_4, 35 wt% in water, Aldrich) was dropwise added into above suspensions under magnetic stirring at room temperature, where the weight ratio of

hydrazine to GO was fixed to 7:10. The mixture was put in a water bath (~95 °C) and stirred for 1 h. After filtration and washing with water, chemically reduced graphene oxide (RGO) was readily obtained.

7.1.2 Preparation of Fe_3O_4@graphene core-shell hybrids

Fe_3O_4 nanospheres (Fe_3O_4 NSs) were first prepared by alcohol reduction of ferric chloride via a solvothermal process.[3, 4] In a typical procedure, $FeCl_3 \cdot 6H_2O$ (2.7 g, 10 mmol) was dissolved in ethylene glycol (80 mL) to form a clear solution, followed by the addition of sodium acetate (7.2 g) and 1,2-ethylenediamine (20 mL). The mixture was stirred for 30 min and then sealed in a Teflon-lined stainless-steel autoclave (100 mL). The autoclave was heated at 200°C for 8 h. After cooling to room temperature, the black products were collected by filtration and washed with ethanol. The obtained Fe_3O_4 NSs (150 mg) were modified by surface grafting of aminopropyltrimethoxysilane (APS) to render the particle surface positively charged.[5] Typically, Fe_3O_4 NSs (150 mg) were dispersed into 150 mL toluene solution via sonication. After 30 min, 1.5 mL of APS was poured into the above solution and refluxed for 24 h under argon atmosphere to obtain APS-modified Fe_3O_4 NSs.

GO-encapsulated Fe_3O_4 NSs (Fe_3O_4@GO) was fabricated by electrostatic assembly of negatively charged GO and positively charged Fe_3O_4 NSs. 200 mL APS-modified Fe_3O_4 dispersion (0.38 mg mL^{-1} in H_2O) was added into a 250 mL GO suspension (0.1 mg mL^{-1} in H_2O) under mild mechanical stirring. After 2 h, Fe_3O_4@GO was obtained by centrifugation and washed with water.

To achieve a favorable electrostatic assembly between Fe_3O_4 NSs and GO, the surface charges of APS-modified Fe_3O_4 NSs and GO depending on various pH values were monitored by zeta potential measurements (Figure 7.1a). The surface charge of modified Fe_3O_4 NSs remained positive over a broad pH range (2.5-8.5) and became negative with a high pH value (>8.5, Figure 1a). In contrast, the zeta potential of GO was negative over the whole investigated pH range, similar to previously reported results.[2] Therefore, assembly between the modified Fe_3O_4 NSs and GO was easily triggered under neutral conditions via electrostatic interactions. Under an optimal condition, almost all the GO and modified oxide nanoparticles coassembled to leave a transparent aqueous solution (Figure 7.1b). The GO shells of Fe_3O_4@GO were chemically reduced by hydrothermal treatment (180 °C, 12 h), resulting into graphene-encapsulated Fe_3O_4 NSs (Fe_3O_4@GS).

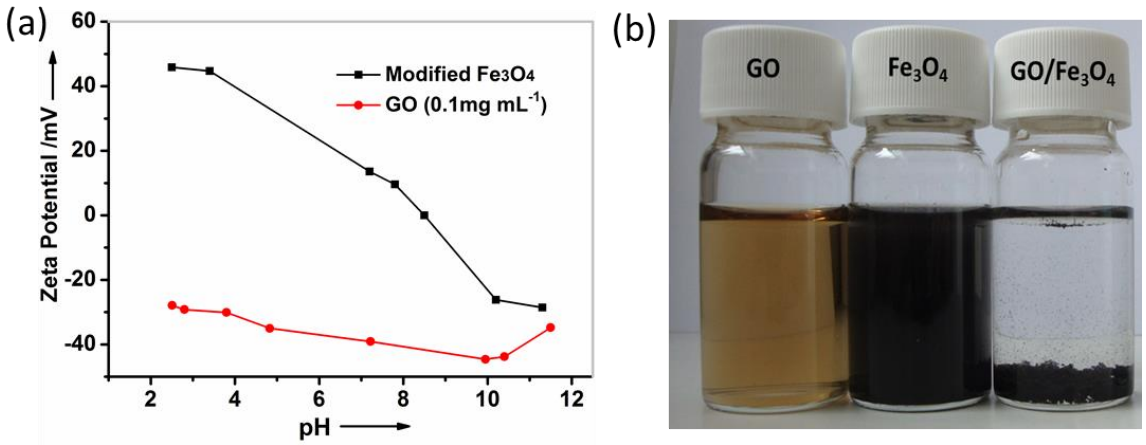

Figure 7.1 (a) Zeta potentials of APS-modified Fe_3O_4 NSs and GO in aqueous solutions under different pH conditions; (b) Photographic illustration on the synthesis of Fe_3O_4@GO.

7.1.3 Preparation of Fe_3O_4/graphene foam hybrids

Fe_3O_4/graphene foam hybrids (Fe_3O_4@GS/GF) were prepared by hydrothermal assembly of Fe_3O_4@GO and additional GO sheets, followed with freeze-drying and thermal treatment. In a typical process, Fe_3O_4@GO was homogeneously dispersed in 10 mL aqueous GO suspension (1 mg mL^{-1}) and sealed in a Teflon-lined autoclave. After hydrothermal treatment at 180 °C for 12 h, the autoclave was naturally cooled to room temperature; the obtained graphene hydrogel embedded with Fe_3O_4 NSs was taken out and freezing dried. Subsequent annealing at 500 °C for 4 h in argon gave rise to Fe_3O_4@GS/GF.

A series of controlled experiments indicate that both GO shells of Fe_3O_4@GO and additional GO sheets have significant effect on the construction of 3D graphene foam structure. The photographs of the synthetic procedures are presented in Figure 7.2. It was found that the aqueous Fe_3O_4 NSs dispersion (without GO encapsulation) tended to precipitate after standing for long time (e.g. 15 h) (Figure 7.2a-i and b-i), whereas the Fe_3O_4@GO dispersed in either water or aqueous GO was stable under the same condition. After hydrothermal treatment, Fe_3O_4@GO dispersed in aqueous GO solution converted to hydrogel successfully (Figure 7.2c-iii), while Fe_3O_4@GO aqueous dispersion without addition of GO agglomerated and precipitated (Figure 7.2c-ii). We surmise that the interaction between GO shells and additional GO layers induces the spontaneous assembly of Fe_3O_4@GO subunits into 3D network structures. During the hydrothermal processing, GO was hydrothermally reduced to graphene, and the exposed graphene layers around Fe_3O_4@GO simultaneously coalesced the additional graphene sheets due to the abundant oxygen-containing groups of GO serving as cross-linking sites.[6] Thereby, 3D hierarchical Fe_3O_4/graphene hybrids were constructed (Figure 7.2d).

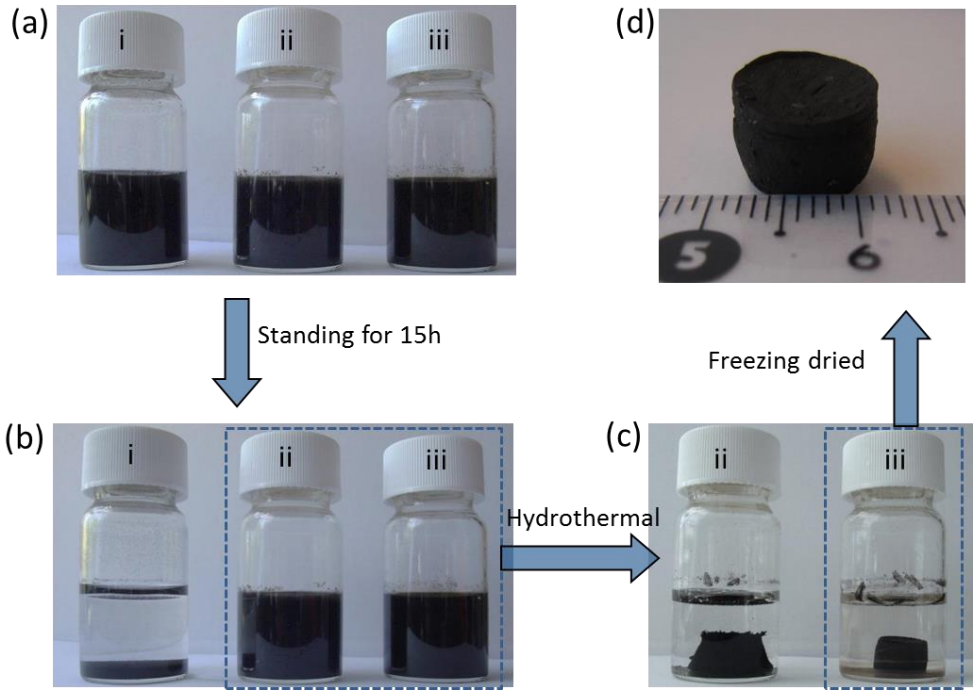

Figure 7.2 Photographic illustrations on synthesis of Fe_3O_4@GS/GF. (a-i) APS-modified Fe_3O_4 NSs in water, (a-ii) Fe_3O_4@GO in water, (a-iii) Fe_3O_4@GO in aqueous GO dispersion (1 mg mL^{-1}). Compared with Fe_3O_4 NSs, Fe_3O_4@GO dispersed in either water or aqueous GO was stable after standing for 15h (b-ii/-iii). After hydrothermal treatment, Fe_3O_4@GO dispersed in GO converted to hydrogel successfully (c-iii), whereas Fe_3O_4@GO in water agglomerated and precipitated. Monolithic Fe_3O_4@GS/GF foam hybrids could be obtained after freeze-drying (d).

7.2 Fabrication of highly porous carbon nanosheets (Chapter 3)

7.2.1 Synthesis of G-silica-I template

Graphene-based silica template (G-silica-I) was fabricated by the hydrolysis of tetraethylorthosilicate (TEOS) on the surface of GO with the aid of cetyltrimethyl

ammonium bromide (CTAB, step 1 in Figure 7.3).[7] Typically, GO (30 mg) was suspended in an aqueous solution containing CTAB (1 g) and NaOH (40 mg), and ultrasonically treated for 3 h. TEOS (1 mL) was slowly added to the above mixture and kept stirring for 12 h at 40 °C. GO-based mesoporous silica sheets were obtained by washing with warm ethanol and centrifugation. Subsequent pyrolysis of GO-based mesoporous silica sheets at 800 °C in N_2 yielded G-silica-I template.

7.2.2 Synthesis of G-silica-II template

60 mg G-silica-I was dispersed in 100 mL aqueous polydiallyldimethylammonium chloride solution (PDDA, 1 wt%) by sonication. After stirring for 12 h at 40 °C, G-silica-I was functionalized with PDDA (PDDA-functionalized G-silica-I) to render the nanosheets surface positively charged (step 2 in Figure 7.3). The resultant PDDA-functionalized G-silica-I was collected by two filtration/washing cycles. Next, PDDA-functionalized G-silica-I was electrostatically assembled with colloidal silica nanoparticles (NPs) in aqueous solution (step 3 in Figure 7.3). In a typical experiment, 0.5 g silica NPs (Ludox AM-30, with diameter of ~12 nm, Aldrich) were dispersed in 50 mL deionized water via sonication to obtain monodisperse silica NPs. The colloidal silica dispersion was mixed with PDDA-functionalized G-silica-I (300 mg L^{-1}) and kept stirring for 3 h. As a result, G-silica-I was further sandwiched with silica shells comprising close-packed silica NPs (denoted as G-silica-II).

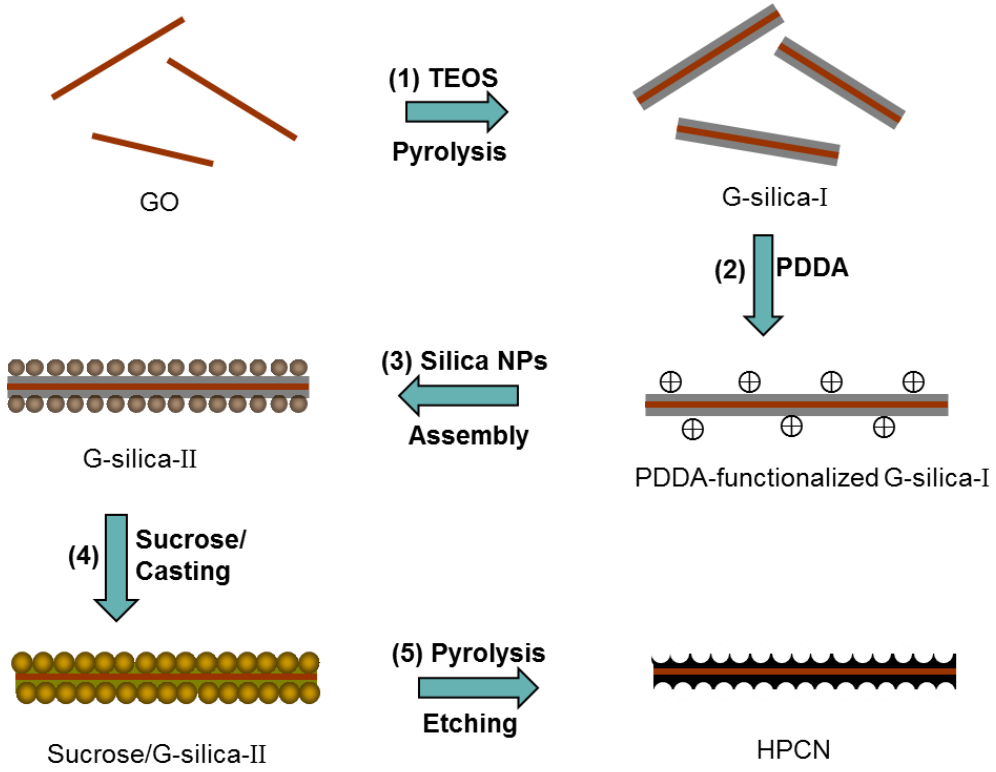

Figure 7.3 Fabrication process for HPCN: (1) hydrolysis of TEOS and removal of CTAB surfactant; (2) surface wrapping G-silica-I with PDDA; (3) electrostatic assembly of G-silica-I with colloidal silica NPs; (4) sucrose casting of G-silica-II template; (5) pyrolysis and silica removal treatment.

7.2.3 Preparation of HPCN

HPCN was produced via a nanocasting technology, with G-silica-II as template and sucrose as carbon source (step 4 and 5 in Figure 7.3). An ethanol solution of sucrose was repeatedly impregnated into G-silica-II template with a mass ratio of sucrose to template of 2:1. Later on, the sucrose-filled G-silica-II template was pyrolyzed at 800 °C in N_2. Subsequent etching of the silica template in NaOH solution (2M) gave birth to HPCN.

7.3 Fabrication of N-doped carbon nanosheets (Chapter 4)

7.3.1 Synthesis of G-silica-X template

Graphene-based silica template (G-silica-X) was synthesized according to the procedure of G-silica-I/-II as described in 7.2; X represents the particle size of colloidal silica template.

7.3.2 Preparation of NDCN catalyst

Nitrogen-doped carbon nanosheets (NDCN-X, X represents the mesopore size) were prepared by surface coating polydopamine (PDA) layer,[8,9] followed by pyrolysis and removal of silica template. Typically, the as-obtained G-silica-2/-7/-22 template were dispersed in dopamine hydrochloride (DA, 200 mg, Aldrich) in Tris-buffer (100 mL, 10 mM, pH 8.5) solution and slightly stirred for 6 h. The resultant polydopamine (PDA)-coated G-silica-2/-7/-22 were collected by centrifugation and washed three times with water. The dried samples were then placed in a tube furnace and heated under N_2 at 900℃ for 2 h with a heating rate of 5℃ min^{-1}. Subsequently, the silica template was removed using NaOH solution (2 M), followed by centrifugation and ethanol washing three times to generate NDNC-2, NDCN-7 and NDCN-22 with defined mesopore size of about 2 nm, 7 and 22 nm, respectively. For comparison, nitrogen-doped carbon nanosheets (NDCN) were prepared by employing pristine graphene nanosheets as substrates (without using silica template). The graphene nanosheets were obtained by chemically reduction of GO with hydrazine (see 7.1.1). Following the above procedures including PDA-coating for 6 h, calcination at 900 ℃, NDCN can be readily obtained.

7.4 Fabrication of EEG-nanoparticle hybrids (Chapter 5)

7.4.1 Electrochemical exfoliation of graphite

EEG was first prepared according to a modified procedure via electrochemical exfoliation of graphite.[10] Natural graphite flakes were used as anode for the electrochemical exfoliation. The graphite flakes were adhered to a conductive carbon tape, forming a pellet. A Pt wire was used as a cathode. The electrolyte for the exfoliation was prepared by dissolving sodium methanesulfonate in aqueous solution (0.1 M). The distance between the graphite and the Pt electrode was ~2 cm and was kept constant throughout the electrochemical process. Electrochemical exfoliation was carried out by applying positive voltage (10 V) to the graphite electrode. After the graphite exfoliation was completed, the product was collected through a polytetrafluoraethylene (PTFE) membrane filter with 0.2 μm pore size and washed several times with deionized water by vacuum filtration. The resultant EEG was then dispersed in *N*,*N*-dimethylformamide (DMF) by sonication for 2 h. The dispersion was maintained for at least 48 h to precipitate un-exfoliated graphite flakes and particles, and the top solution was used for characterization and materials synthesis.

7.4.2 Functionalization of EEG

EEG was functionalized with polyaniline (emeraldine base form, PANB) via π-π interactions. Typically, 2 mg EEG nanosheets was dispersed in 20 mL DMF solution of PANB (0.2 mg mL^{-1}) by sonication, and the suspensions were stirred for 12 h at room temperature. Afterwards, EEG-PANB was collected by filtration and washed two times with DMF.

7.4.3 Assembly of EEG-nanoparticle hybrids

Si, Fe_3O_4 and Pt nanoparticles (NPs) were used as the functional components for the assembly of EEG hybrids. Si NPs with an average particle size of ≤50 nm were obtained from Alfa Aesar. In a typical synthesis of Fe_3O_4 NPs,[11] 2.6g $FeCl_3$ (16 mmol) and 1.59 g $FeCl_2 \cdot 4H_2O$ (8.0 mmol) were dissolved in 12.5 mL water with 0.43 mL of 12 M HCl, and then the mixture was added dropwise into 125 mL of 1.5 M NaOH aqueous solution under vigorous stirring. The black precipitation was collected by centrifugation at 4000 rpm and washed with ultrapure water for 3 times. The cationic Fe_3O_4 NPs were then peptized by adding water with the aid of mild ultrasonication, resulting in a yellow hydrosol of Fe_3O_4.

Polyvinylpyrrolidone (PVP)-capped Pt NPs were prepared according to a modified procedure.[12] Ethylene glycol (EG) solutions of PVP (3mL, 0.375 M) and $H_2PtCl_6 \cdot 6H_2O$ (1.5 mL, 0.0625 M) were added to boiling EG (2.5 mL) alternatively every 30 s for 16 min. The resulting mixture was refluxed for another 10 min. The product was precipitated with the addition of acetone and washed with ethanol two times. The resulting residue was redispersed in water to obtain a yellow-brown dispersion with the aid of ultrasonication.

EEG-Si hybrids were fabricated by co-assembly of Si NPs and EEG-PANB. Typically, 18 mg Si NPs were added to 100 mL DMF and sonicated to obtain monodispersed Si NPs. The Si NPs/DMF dispersion was mixed with EEG-PANB under stirring for 1 h to produce EEG-PANB-Si hybrids. The photograph in Figure 7.4 illustrates the co-assembly process. Interestingly, some agglomerates spontaneously formed as soon as the Si NPs (b) was diluted into the EEG-PANB suspensions (a), indicating that the self-assembly of the two species occurred. Under an optimal mass ratio, almost all EEG-PANB and Si NPs co-assembled and left a transparent solution (c). In a control experiment, Si NPs was added to

the pristine EEG dispersion without PANB functionalization, whereas only a dark-yellow suspension was observed (d). Such comparative results highlight that the PANB functional layers act as the crucial driving force to couple the Si NPs on EEG surface.

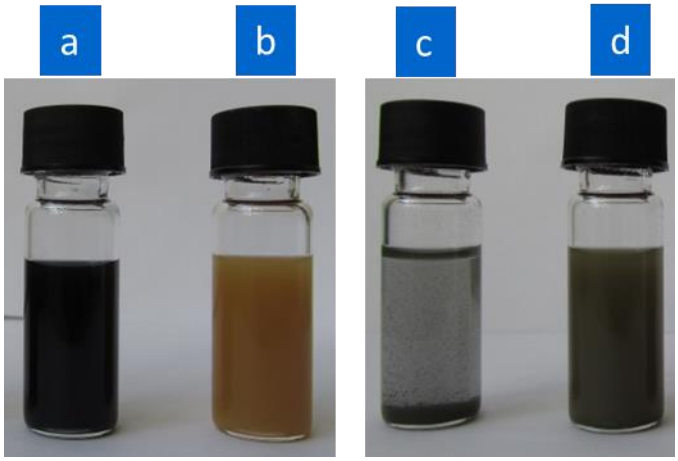

Figure 7.4 Photographic illustration on synthesis of EEG-Si hybrids (a) EEG-PANB in DMF; (b) Si NPs in DMF; (c) EEG-Si sample obtained after coassembly of (a) and (b); (d) EEG/Si suspensions obtained by blending pristine EEG sheets and Si NPs.

To promote the electrical conductivity, EEG-PANB-Si were separated by centrifugation and dispersed in 0.5 M HCl in mixed solvents of DMF/H_2O (v/v=1:1). After stirring for 1 h, EEG-Si hybrids were obtained by filtration and washed with ethanol for three times. Following the same assembly protocol, EEG-Fe_3O_4 and EEG-Pt hybrids were readily fabricated. To determine the effect of EEG on the electrochemical performance of hybrids (for lithium storage), such an assembly was extended to fabricate RGO-based Si hybrids (RGO-Si). RGO was prepared by chemical reduction of GO with hydrazine in the aqueous ammonia solution (see 7.1.1). As-obtained RGO was employed as substrates for surface functionalization and assembly of Si NPs. The experimental procedure is identical to that of EEG-Si.

7.5 Material characterizations and techniques

7.5.1 X-ray diffraction (XRD)

XRD data were collected with a Philips X-ray diffractometer (PW 1820) equipped with Cu Kα radiation (λ=1.5418Å). The crystalline phases were determined by comparing the XRD patterns with standard JCPDS (Joint Committee on Powder Diffraction Standards) cards.

7.5.2 Surface area and pore size measurements

Nitrogen isothermal adsorption/desorption measurements were performed on a porosimetry analyzer (Micromeritcs Tristar 3020, USA) at 77K. Prior to measurement, the sample was purged with flowing N_2 at 423 K for 2 h. The specific surface area was calculated from the nitrogen adsorption data in the relative pressure range (P/Po) of 0.06–0.20. The total pore volume was determined from the amount of N_2 uptake at a relative pressure of P/Po = 0.95. The pore size distribution plot was derived from the adsorption branch of the isotherm based on the Barrett–Joyner–Halenda (BJH) model.

7.5.3 Thermogravimetric analysis (TGA)

TGA is a technique that measures the change in weight of a sample as it is heated in different atmosphere (e.g., N_2, O_2, air). Its main use is to characterize materials with regard

to their compositions. The weight fraction of graphene in different hybrids was studied by a Mettler TG50 Thermogravimetric Analyzer at a heating rate of 10℃ min^{-1} in flowing air.

7.5.4 Scanning electron microscopy (SEM)

SEM is a typical electron microscope that produces images of a sample by scanning it with a focused beam of electrons. The electrons interact with atoms in the sample, producing various signals that can be detected and that contain information about the sample's surface topography and composition.[13,14] In our lab, morphology observations of all materials were conducted with a LEO 1530 Gemini (Zeiss, Field emission gun (FEG), acceleration voltage V_{acc}= 0.2 - 30 kV, resolution: 1.0 nm at 20 kV, 2.5 nm at 1 kV, 5 nm at 0.2 kV).

7.5.5 Transmission electron microscopy (TEM)

TEM is a microscopy technique in which a beam of electrons is transmitted through an ultra-thin specimen, interacting with the specimen as it passes through. An image is formed from the interaction of the electrons transmitted through the specimen; the image is magnified and detected by a sensor such as a CCD (charge-coupled device) camera.[15,16]

The TEM characterizations were carried out by a JEOL JEM-1400 Transmission Electron Microscope with the maximum acceleration voltage of 120 kV. The high-resolution TEM images were acquired with Philips Tecnai F20 in an acceleration voltage of 200 kV.

7.5.6 Atomic force microscopy (AFM)

The thickness of materials was investigated by tapping mode AFM (VEECO Dimension 3100). The Dimension 3100 is capable of imaging specimens with a horizontal and vertical resolution down to a fraction of a nanometer. The instrument works by measuring the deflection produced by a sharp tip on micron-sized cantilever as it scans across the surface of the specimen.[17] The samples were prepared by dip coating material dispersion (in ethanol) on SiO_2/Si substrates.

7.5.7 X-ray photoelectron spectroscopy (XPS)

XPS is a surface analysis technique which measures the elemental composition at the top 0~10 nm of the sample. The sample surface is irradiated with a beam of X-rays, and the kinetic energy and number of escaping electrons from the sample surface are analyzed.[18] XPS measurements in this study were carried out on an AXIS Ultra DLD system from Kratos with Al Kα radiation as X-ray source for radiation. The deconvolution of the C1s and N1s spectra was performed with XPSPEAK software with Gaussian-Lorentzian functions and a Shirley background.

7.5.8 Raman spectroscopy

Raman spectroscopy has historically been used to probe structural and electronic characteristics of graphite materials, providing useful information on the defects (D-band), in-plane vibration of sp^2 carbon atoms (G-band), as well as the stacking orders (2D-

band).[19] Raman spectra of all samples were recorded with a Bruker RFS 100/S spectrometer with excitation laser beam wavelength of 532 nm. The powders of materials were placed on clean SiO_2/Si substrates for the measurement.

7.5.9 Fourier transform infrared spectroscopy (FT-IR)

The infrared spectrum of a sample was recorded by passing a beam of infrared light through the sample. When the frequency of the IR is the same as the vibrational frequency of a bond, the absorption occurs. Examination of the transmitted light reveals how much energy was absorbed at each frequency (or wavelength), which was achieved by scanning the wavelength range using a monochromator. Analysis of the position, shape and intensity of peaks in this spectrum reveals details about the molecular structure of the sample.[20] FT-IR spectra were recorded using Nicolet 730 (Thermo Scientific, Inc., USA) spectrometer.

7.5.10 Ultraviolet–visible spectroscopy (UV-vis)

Molecules containing π-electrons or non-bonding electrons (n-electrons) can absorb the energy in the form of ultraviolet or visible light to excite these electrons to higher anti-bonding molecular orbitals. The more easily excited the electrons (i.e. lower energy gap between the highest occupied molecular orbital (HOMO) and the lowest unoccupied molecular orbital (LUMO)), the longer the wavelength of light it can absorb.[21] UV-vis spectra of graphene samples were recorded using Lambda 900 (Perkin Elmer, Inc., USA) spectrometer.

7.5.11 Zeta potential

Zeta potential (ζ) is an indicator of the stability of colloidal dispersions. From a theoretical viewpoint, ζ is the potential difference between the dispersion medium and the stationary layer of fluid (interfacial double layer) attached to the dispersed particles. The magnitude of ζ indicates the degree of electrostatic repulsion between adjacent, similarly charged particles in the dispersions. For molecules and particles that are small enough, a high zeta potential will confer stability.[22]

Zeta potential measurements in this work were conducted using a Zetasizer 3000 (Malvern Instruments). The pH values of samples were adjusted by adding ammonia solution or diluted hydrochloric acid.

7.5.12 Film resistance

The film samples were fabricated by vacuum filtration of graphene or graphene hybrids dispersion in DMF through PTFE membrane, followed by transfer of the film through mechanically pressing against a SiO_2/Si substrate. The sheet resistance of film sample was measured with a four-point probe system using Keithly 2700 Multimeter (probe spacing: 0.635 mm, Rs = 4.532 V/I).

7.6 Electrochemical characterizations and techniques

7.6.1 Lithium-ion battery

The working electrodes were prepared by mixing the active materials, carbon black (Super-P), and binder at different weight ratio and pasted on pure copper foil. The detailed experimental parameters were summarized in Table 7.1. The resulting electrode films were punched into disk with diameter of 10 mm and vacuum dried at 80°C overnight.

Table 7.1 Experimental parameters on electrode preparation and cell test.*

Active material (AM)	Conductive additive	Binder	Weight ratio (AM/Super P /Binder, wt%)	Electrolyte	Voltage range (V /vs. Li/Li^+)
Fe_3O_4/Graphene hybrids (Chapter 2)	Super P carbon black	PVDF /NMP	80/10/10	1M $LiPF_6$ EC/DMC (v/v, 1/1)	0.01-3
EEG/Silicon hybrids (Chapter 5)	Super P carbon black	Sodium alginate /H_2O	60/20/20	1M $LiPF_6$ EC/DEC (v/v, 3/7) + VC (2wt%)	0.01-1.5

***Abbreviations:** EEG-Electrochemically exfoliated graphene; PVDF-poly(vinyl difluoride); NMP-*N*-Methyl-2-pyrrolidone; EC-ethylene carbonate; DMC-dimethyl carbonate; DEC-diethyl carbonate; VC-Vinylene carbonate.

The cells were assembled in an argon-filled glovebox with the concentrations of moisture and oxygen below 1 ppm. Lithium foil (Aldrich) was used as the counter electrode. The electrolyte consisting of 1M $LiPF_6$ in a mixture of aprotic solvents (ethylene carbonate/dimethyl carbonate/diethyl carbonate) was obtained from Ube Industries Ltd.

The necessary components were collected and assembled into CR2032 coin type cells. The order of the assembly is presented in Figure 7.5.[23] The electrochemical performance was tested at various current densities in defined voltage ranges (see Table 7.1). Electrochemical impedance spectral measurements were carried out in the frequency range from 100 kHz to 0.01Hz on a PARSTRAT 2273 electrochemical workstation.

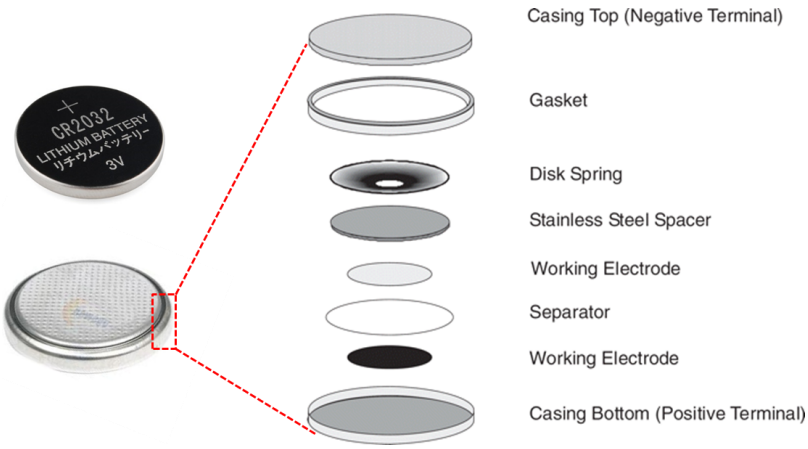

Figure 7.5 An illustration of the coin-type cell parts and assembly. In the "half cell," one working electrode is Li foil.[23]

7.6.2 Supercapacitor

All the working electrodes were fabricated by physically mixing 80 wt% graphene hybrids, 10 wt% Super-P carbon black, and 10 wt% PTFE binder dispersed in ethanol solvent, and then pressed onto a platinum mesh serving as a current collector, a platinum plate as counter electrode, an Ag/AgCl (KCl, saturated) electrode as reference electrode, and 1 M H_2SO_4 as aqueous electrolyte.

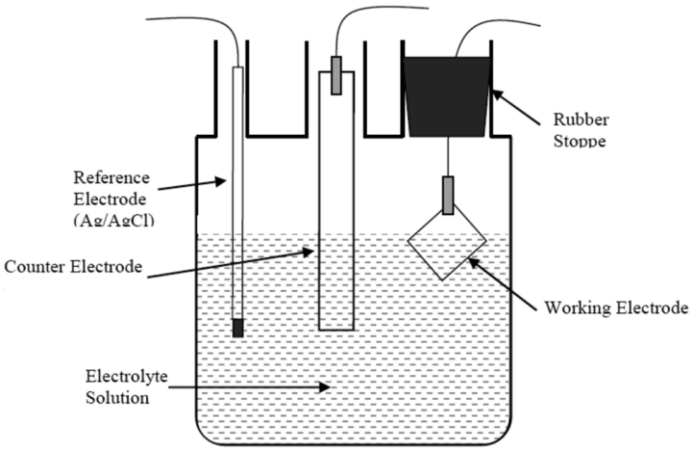

Figure 7.6 Typical profile of Three-electrode electrochemical system.[24]

Electrochemical measurements of supercapacitors (SCs) were carried out in a three-electrode system (Figure 7.6).[24] The electrochemical performance of samples was determined by the CV measurements and galvanostatic charge-discharge tests on a CH 1760E electrochemical workstation (CHI Inc., USA). The specific capacitance (F g^{-1}) was calculated from the CV curves based on the follow formula:

$$C_m = 2\int Idv/(v \cdot \Delta V \cdot m)$$

Where I is the current (A), V is the voltage (V), v is the scan rate (V s^{-1}), and m is the mass of active electrode material (g).[25]

7.6.3 Oxygen reduction reaction

Rotating disk electrode (RDE) and rotating ring-disk electrode (RRDE) were used as the substrate of working electrode for evaluating the ORR activity and durability of various catalysts. Figure 7.7a shows a photograph of RRDE electrode with a Pt ring (5.52 mm

innerdiameter and 7.16 mm outer-diameter) and a glassy carbon disk (5.0 mm diameter). Prior to use, the glass carbon electrode was polished mechanically with an alumina slurry to obtain a mirror-like surface and then washed with Mill-Q water and allowed to dry. For electrode preparation, 10 mg samples (NDCN and NDCN-X) were dispersed in 0.5 mL solvent mixture of Nafion (5 wt %) and ethanol (V: V ratio = 1:4) for 0.5~1 h under sonication. Then 6 μL portion of each suspension was slightly dropped on the disk surface of the pre-polished glassy carbon electrode. For comparison, a commercially available catalyst of 20 wt% Pt/C powder (E-TEK) was used and 5 mg mL^{-1} Pt/C suspension was prepared as the same procedure above. The electrodes were then dried overnight at room temperature before measurement.

Electrochemical measurements of cyclic voltammetry (CV), RDE and RRDE were performed by a computer-controlled potentiostat (CHI 760C, CH Instrument, USA) with a three-electrode cell system. A glass carbon RDE/RRDE (Autolab) after loading the electrocatalyst was used as the working electrode, an Ag/AgCl (KCl, 3 M) electrode as the reference electrode, and a Pt wire as the counter electrode. The electrochemical experiments were conducted in O_2 saturated 0.1 M KOH or 0.5 M H_2SO_4 electrolyte for the oxygen reduction reaction. The potential range was cyclically scanned between -1.0 and +0.2 V (between 0.03 and 1.03 V vs. RHE in 0.5 M H_2SO_4) at a scan rate of 10 mV s^{-1} at room temperature after purging O_2 or Ar gas for 20 min. RDE measurements were conducted at different rotating speeds from 400 to 2500 rpm, using an Autolab Model, and RRDE measurements were carried out at 1600 rpm with an Autolab Model.

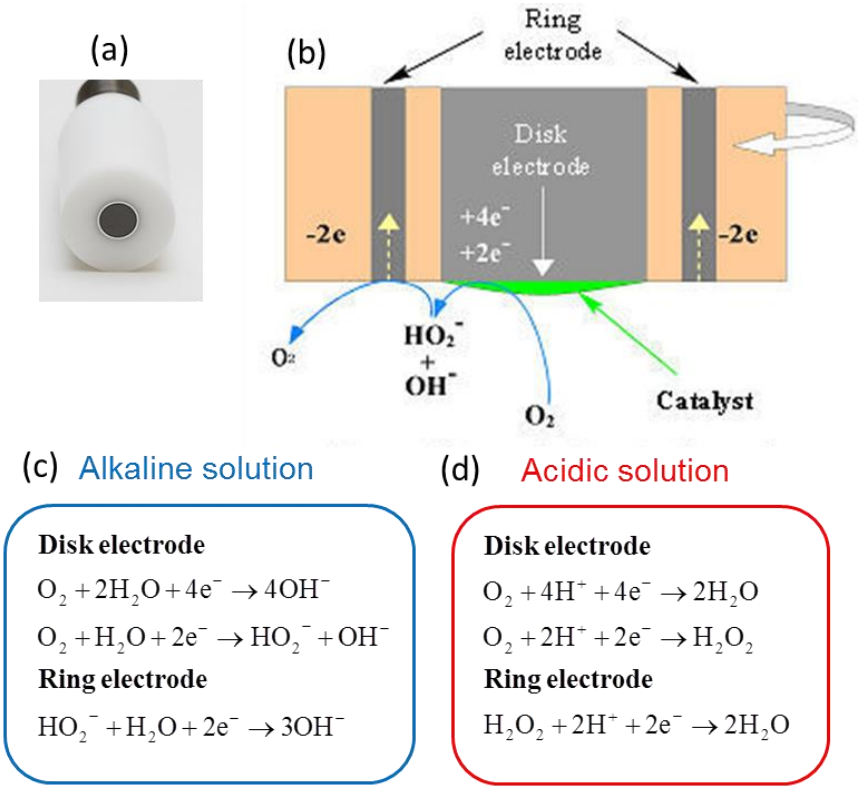

Figure 7.7 (a) An photograph of rotating ring-disk electrode; (b) Illustration of ORR catalytic reactions on RRDE;[26] ORR reactions in alkaline (c) and acidic aqueous solution (d).

In general, there are two electrochemical pathways to reduce oxygen to water in aqueous electrolytes. As illustrated in Figure 7.7b, O_2 can be electrochemically reduced either directly to water (4-electron reduction) or to HO_2^- intermediate (2-electron reduction) in the alkaline solution. The 2-electrons reduction intermediate HO_2^- can be transported to the ring electrode (Pt) by rotation and electrochemically reduced to water.[26] The mechanism of the electrochemical O_2 reduction reaction is quite different in the alkaline and acidic condition as illustrated in Figure 7.7c and d. For fuel cell applications, the 4-electron direct pathway is highly preferred. The 2-electron reduction pathway is used in industry for H_2O_2 production.[27]

The electron transfer number (n) was determined from RRDE measurement on the basis of the disk current (I_D) and ring current (I_R) via the following equation:[28]

$$n = 4 \times \frac{I_D}{(I_D + I_R / N)}$$

The peroxide percentage (H_2O_2 %) was calculated based on the following equation:

$$H_2O_2(\%) = 200 \times \frac{I_R / N}{(I_D + I_R / N)}$$

where N=0.36 is the current collection efficiency of Pt ring.

7.7 References

[1] W. S. Hummers, R. E. Offeman, *J. Am. Chem. Soc.* **1958**, *80*, 1339.

[2] D. Li, M. B. Müller, S. Gilje, R. B. Kaner, G. G. Wallace, *Nat. Nanotech.* **2008**, *3*, 101.

[3] H. Deng, X. L. Li, Q. Peng, X. Wang, J. P. Chen, Y. D. Li, *Angew. Chem. Int. Ed.* **2005**, *44*, 2782.

[4] J. F. Zhou, L. J. Meng, X. L. Feng, X. K. Zhang, Q. H. Lu, *Angew. Chem. Int. Ed.* **2010**, *49*, 8476.

[5] S. B. Yang, X. L. Feng, S. Ivanovici, K. Müllen, *Angew. Chem. Int. Ed.* **2010**, *49*, 8408.

[6] Y. X. Xu, K. X. Sheng, C. Li, G. Q. Shi, *ACS Nano* **2010**, *4*, 4324.

[7] S. B. Yang, X. L. Feng, L. Wang, K. Tang, J. Maier, K. Müllen, *Angew. Chem. Int. Ed.* **2010**, *49*, 4795.

[8] H. Lee, S. M. Dellatore, W. M. Miller, P. B. Messersmith, *Science* **2007**, *318*, 426.

[9] R. J. Li, K. Parvez, F. Hinkel, X. L. Feng, K. Müllen, *Angew. Chem. Int. Ed.* **2013**, *52*. 5535.

[10] K. Parvez, Z.-S. Wu, R. J. Li, X. J. Liu, R. Graf, X. L. Feng, K. Müllen, *J. Am. Chem. Soc.* **2014**, *136*, 6083.

[11] Y. S. Kang, S. Risbud, J. F. Rabolt, P. Stroeve, *Chem. Mater.* **1996**, *8*, 2209.

[12] O. D. Lyons, N. E. Musselwhite, L. M. Carl, K. A. Manbeck, A. L. Marsh, *Langmuir* **2010**, *26*, 16481.

[13] D. Mcmullan, *Scanning* **1995**, *17*, 175.

[14] http://en.wikipedia.org/wiki/Scanning_electron_microscope

[15] B. Fultz, J. Howe, *Transmission Electron Microscopy and Diffractometry of Materials*, Springer ISBN: 3-540-73885-1, USA **2007**.

[16] http://en.wikipedia.org/wiki/Transmission_electron_microscopy

[17] G. Binnig, C. F. Quate, C. Gerber, *Phys. Rev. Lett.* **1986**, *56*, 930.

[18] S. Hüfner, *Photoelectron spectroscopy: principles and applications*, Springer-Verlag ISBN: 3-540-41802-4, Berlin, **2003.**

[19] Y. Y. Wang, Z. H. Ni, T. Yu, Z. X. Shen, H. M. Wang, Y. H. Wu, W. Chen, A. T. S. Wee, *J. Phys. Chem. C* **2008**, *112*, 10637.

[20] http://en.wikipedia.org/wiki/Infrared_spectroscopy

[21] http://en.wikipedia.org/wiki/Ultraviolet%E2%80%93visible_spectroscopy

[22] http://en.wikipedia.org/wiki/Zeta_potential

[23] J. C. Burns, L. J. Krause, D. B. Le, L. D. Jensen, A. J. Smith, D. J. Xiong, J. R. Dahna, *J. Electrochem. Soc.* **2011**, *158*, A1417.

[24] L. M. Kindschy, E. C. Alocilja, *Sensors* **2007**, *7*, 1630.

[25] Z. H. Wen, X. C. Wang, S. Mao, Z. Bo, H. Kim, S. M. Cui, G. H. Lu , X. L. Feng, J. H. Chen, *Adv. Mater*. **2012**, *24*, 5610.

[26] http://www.als-japan.com/support-hydrodynamic-voltammetry.html

[27] J. J. Zhang, *PEM Fuel Cell Electrocatalysts and Catalyst Layers: Fundamentals and Applications*, Springer-Verlag ISBN: 978-1-84800-935-6, London **2008.**

[28] Z. S. Wu, S. B. Yang, Y. Sun, K. Parvez, X. L. Feng, K. Müllen, *J. Am. Chem. Soc.* **2012**, *134*, 9082.

List of Publications:

(1) **Wei Wei**, Haiwei Liang, Khaled Parvez, Xiaodong Zhuang, Xinliang Feng, Klaus Müllen, Nitrogen-doped Carbon Nanosheets with Size-Defined Mesopores as Highly Efficient Metal-Free Catalyst for the Oxygen Reduction Reaction, ***Angew. Chem. Int. Ed.*** **2014**, *53*, 1570-1574; ***Angew. Chem.*** **2014,** *126*, 1596-1600;

(2) **Wei Wei**, Shubin Yang, Haixin Zhou, Ingo Lieberwirth, Xinliang Feng, Klaus Müllen, 3D Graphene Foams Cross-Linked with Pre-Encapsulated Fe_3O_4 Nanospheres for Enhanced Lithium Storage, ***Adv. Mater.*** **2013**, *25*, 2909–2914;

(3) **Wei Wei**, Gang Wang, Sheng Yang, Xinliang Feng, Klaus Müllen, Efficient Coupling of Nanoparticles to Electrochemically Exfoliated Graphene, ***J. Am. Chem. Soc.*** **2015**, **DOI:** 10.1021/jacs.5b02284;

(4) **Wei Wei**, Jiulin Wang, Longjie Zhou, Jun Yang, Bernd Schumann, Yanna NuLi, CNT Enhanced Sulfur Composite Cathode Material for High Rate Lithium Battery, ***Electrochem. Commun.*** **2011**, *13*, 399-402;

(5) Haiwei Liang, **Wei Wei**, Zhongshuai Wu, Xinliang Feng, Klaus Müllen, Mesoporous Metal-Nitrogen-Doped Carbon Electrocatalysts for Highly Efficient Oxygen Reduction Reaction, ***J. Am. Chem. Soc.*** **2013**, *135*, 16002-16005;

(6) Shaohua Liu, Pavlo Gordiichuk, Zhongshuai Wu, Zhaoyang Liu, **Wei Wei**, Dongqing Wu, Yiyong Mai, Andreas Herrmann, Klaus Müllen, Xinliang Feng, Patterning Two-Dimensional Free-Standing Surfaces with Mesoporous Conducting Polymers, Submitted to ***Nat. Nanotechnol.***.